Spring 2007

# Molecular Dynamics Simulations to Probe Effects of Ultra-Short, Very-High Voltage Pulses on Cells

Viswanadham Sridhara
*Old Dominion University*

# MOLECULAR DYNAMICS SIMULATIONS TO PROBE EFFECTS OF ULTRA-SHORT, VERY-HIGH VOLTAGE PULSES ON CELLS

by

Viswanadham Sridhara
M.S. August 2003, Old Dominion University.

A Dissertation Submitted to the Faculty of
Old Dominion University in Partial Fulfillment of the
Requirement for the Degree of

DOCTOR OF PHILOSOPHY

ELECTRICAL AND COMPUTER ENGINEERING

OLD DOMINION UNIVERSITY
May 2007

Approved by:

Ravindra P. Joshi (Director)

Richard L. Nuccitelli (Member)

Linda L. Vahala (Member)

R. James Swanson (Member)

# ABSTRACT

## MOLECULAR DYNAMIC SIMULATIONS TO PROBE EFFECTS OF ULTRA-SHORT, VERY-HIGH VOLTAGE PULSES ON CELLS

Viswanadham Sridhara
Old Dominion University, 2007
Director: Dr. Ravindra P. Joshi

The use of very high electric fields (~ 100kV/cm or higher) with pulse durations in the nanosecond range (Ultra-short) has been a very recent development in bio-electrics. Traditionally, the electric field effects have mostly been confined to: (a) low field, long-duration pulses, and (b) focused mainly on electroporation studies. Thus, aspects such as possible field-induced DNA damage, calcium release, alterations in neuro-transmitters, or voltage-gating have generally been overlooked.

Ultra-short, high-field pulses open the way to targeted and deliberate apoptotic cell killing (e.g., of tumor cells). Though experimental data is very useful, it usually yields information on macroscopic variables that is inherently an average over time and/or space. Measurements often do not provide the molecular level information or details, as might be possible through numerical simulations. Also, the relevance and relative role of underlying physical mechanisms cannot be probed. With developments in computer technology, rapid advances in numerical algorithms for parallel computing, and with increasing computational resources, computer simulations of cellular dynamics and biological phenomena is gaining increasing popularity. A range of simulation methods exist that span the macroscopic continuum approaches (e.g. the Smoluchowski equation), to those based on the semi-classical retarded Langevin and Green's functions, to microscopic-kinetic analyses based on Brownian dynamics or Molecular Dynamics (MD). Here we focus on the MD technique, as it provides the most comprehensive, time-dependent, three-dimensional nanoscale analyses with inclusion of the many-body aspects. This dissertation research presents simulations and analyses of

lipid membrane poration and its dynamics, predictions of transport parameters under high-field, non-equilibrium conditions, electric fields effects on DNA, micelle disintegration, protein unfolding and intra-cellular calcium release.

The following results have been found as a result of the application of external electric fields on cells: (a) Poration due to the re-orientation of the lipid molecules within the lipid bilayer, (b) Externalization of charged molecules such as Phosphotidyl Serine (PS), (c) Dramatic lowering of permittivity and diffusion coefficient with spatially structured layering of the membrane nanopore, (d) DNA alignment in the direction of electric field and eventual fragmentation, (e) Calcium release from the endoplasmic reticulum (ER) leading to time-dependent oscillatory waves and (f) Membrane fragmentation upon the application of high external fields.

*This thesis is dedicated to my parents*
*and my family.*

# TABLE OF CONTENTS

# LIST OF FIGURES

# LIST OF TABLES

# CHAPTER I

# INTRODUCTION

## 1.1 Overview

The interaction of electric and magnetic fields with biological systems (1-3) has been of long standing scientific interest. This interaction might be accidental, coming from various electrical devices and appliances, but could also be intentional, like exposure of biological tissue to short electrical pulses (time periods ranging from microseconds to milliseconds) for electrochemotherapy and DNA electro transfer (4). The use of very high electric fields (~100KV/cm) with pulse durations in the nanosecond range has been a very recent development in the area of bio-electrics (5). This technique is new and has been termed as intracellular manipulation. The primary objective of this technique is to treat different types of cancer and assist in introducing drugs to specific sites. Recently, experiments on mice treated with melanoma have already confirmed the hypothesis of field-assisted cancer cell death (6). This could be a drug-free therapy, as the pulsed electric fields are shown to cause apoptosis directly without any gene transfer and without the injection of drugs. Some of the other observed experimental results are outlined in the next section. These experimental results of PEF's on cells often do not provide the molecular level information or the details and insights needed to understand the underlying biophysical mechanisms involved in apoptosis induction (tumor destruction). Hence, there is an immense need to carry out simulations both at microscopic and macroscopic levels that would help provide an understanding and quantitative assessment of the apoptosis phenomena. With developments in computer technology, rapid advances in numerical algorithms for parallel computing, and with increasing computational resources, computer simulations of cellular dynamics and biological phenomena is gaining increasing popularity over the last few decades (7). These simulations can help quantify the roles of various inherent processes and also

---

Dissertation References Format: Proceedings of the National Academy of Sciences.

gauge the importance of several on-going mechanisms involved in the application of nsPEF's on biological tissues.

## 1.2 Experimental Observations of Pulsed Electric Fields on Cells

Some of the salient features that have emerged from the studies of cellular responses to high-intensity, pulsed electric fields are given as follows.

(i) Apoptosis has been observed (8) for cells subjected to the short electrical pulses.

(ii) Multiple pulses have been observed to do more irreversible damage than single-shot electric shocks (6).

(iii) Externalization of phosphatidylserine (PS) was shown to occur in response to a nanosecond pulse for average electric fields above 2 MV/m (9).

(iv) A distinct polarity effect has been observed, with the *externalization predominantly occurring at the anode end.* In addition, asymmetry in transmembrane potentials at the anodic and cathodic poles has been demonstrated (10).

(v) Calcium is released from the intracellular endoplasmic reticulum in response to external voltage pulses (11). This could be a vital element in induction or possible suppression of cell signaling.

(vi) Molecular uptake has been shown to be delayed process as compared to conventional electroporation that utilize smaller electric fields and longer time durations (5).

(vii) DNA damage in cells due to the ultrashort pulses has been observed (12).

## 1.3 Scope of the Present Dissertation Research

The application of pulsed electric fields on cells induce transmembrane potentials across various membranes (plasma, nuclear, inner and outer mitochondrial etc.) in cells, leading to permeabilization of membranes, if the membrane voltage reaches a minimum

threshold of about 1V. These membranes are generally few (~1-10) nanometers thick. Furthermore, the technique of intracellular manipulation requires the externally applied electric fields to penetrate deep into the sub-cellular organelles. Based on simple considerations of circuit theory and capacitive charging, one can easily show that only electric fields of short duration and fast rise-times could be capable of penetrating sub-cellular structures. Hence, the time scales of interest here are typically a few nanoseconds. Hence a nanoscale, molecular approach to modeling bioelectric response at cellular level capable of resolving events on nansoseconds or less, is necessary to understand the underlying biophysics of the interactions of PEF's on cells. Here, we focus on Molecular Dynamics (MD) technique (7, 13, 14) as it provides the most comprehensive, time-dependent, three-dimensional nanoscale analyses with inclusion of the many-body aspects. Details of the MD technique can be found in Chapter III.

Most of the work done in MD simulations is to understand structure and dynamics of molecular clusters, chains, and lipid bilayers (15). Recently, there has been some progress made in understanding proteins and micelles (16). However, there are not many reports on the electrical interactions on cellular response and the molecular biophysics. In particular, MD analyses in the context of nanosecond bio-electrics, is severely lacking. Yet aspects such as electroporation (3) or intracellular manipulation (5) that arise from the application of short duration high-amplitude pulses to cell membranes need to be understood. *The primary objective in the dissertation work reported here is to use MD technique to probe effects quantitatively and analyze the response of ultra-short, very high amplitude pulsed electric fields on cells.*

In this dissertation report, Chapter II provides the relevant literature review on traditional electroporation principles along with introducing to the novel concept of intracellular manipulation. This chapter also provides the relevant studies done in the past in the area of computational structural biology. In addition, Chapter II introduces the lipid membrane models, water models and other protein models obtained from X-ray

diffraction studies. These models are used to carry out simulations in this dissertation research reported here. In Chapter III, the details of various computational algorithms in MD technique along with other physics-based mathematical models used for the studies of nsPEF's on cells are provided. Chapter IV of this dissertation research report presents simulations and analyses of several aspects including membrane poration and its dynamics; predictions of transport parameters under high-field, non-equilibrium conditions; electric fields effects on DNA; micelle disintegration; protein unfolding; and intra-cellular calcium release. Finally, Chapter V summarizes the work reported in this dissertation report along with the scope for future work.

# CHAPTER II

# LITERATURE REVIEW

## 2.1 Introduction

The use of very high electric fields (~ 100kV/cm or higher) with pulse durations in the nanosecond range (17) has been a very recent development in bio-electrics. Traditionally, the electric field effects have mostly been confined to: (a) low field, long-duration pulses, and (b) focused mainly on membrane electroporation studies. Thus, aspects such as possible field-induced DNA damage, calcium release, alterations in neuro-transmitters, or voltage-gating have generally been overlooked. Relatively low external electric fields (less than a kilo-Volt per centimeter), applied over time periods ranging from several tens of microseconds to milliseconds have traditionally been studied.

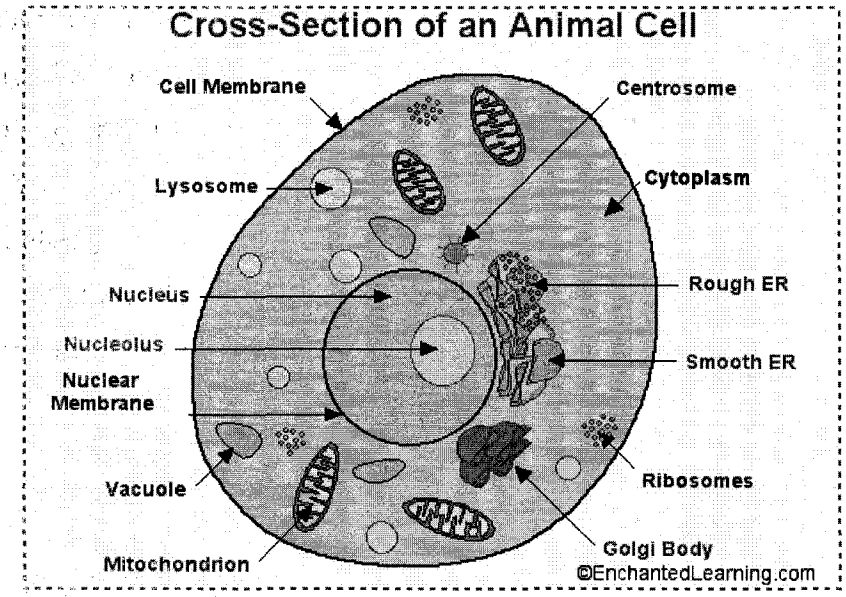


Fig. 2.1. Animal cell.

## 2.2 Pulsed Electric Field Effects on Cells

A basic structure of the cell is given in Fig. 2.1. Exposure of these cells to electric fields can lead to a variety of biochemical responses. Living biological cells contain many membranes, first at the outer boundary i.e., plasma membrane and then further in at the boundary of the nucleus, endoplasmic reticulum, mitochondria and other sub-cellular structures. The main function of the cell membranes is to isolate regions of different materials, but also to facilitate the flow of selected types of ions in and out of the cell (18). We can, therefore, think of the cell as a conductor surrounded by an insulating envelope and containing substructures with similar properties. The simplified model of such a cell with one substructure, the nucleus is shown in Fig. 2.2. The effect of pulsed electric fields can be understood qualitatively by considering cell as an electric circuit as shown in Fig. 2.2., describing the various cell membranes by their capacitances and their content i.e., cytoplasma, by resistance. In this circuit, the value of the conductance of membranes and inner media, as well as the capacitances of the membranes, is experimentally calculated by a technique called time domain dielectric spectroscopy (TDDS). The background information on this technique is given in the later sections of this chapter.

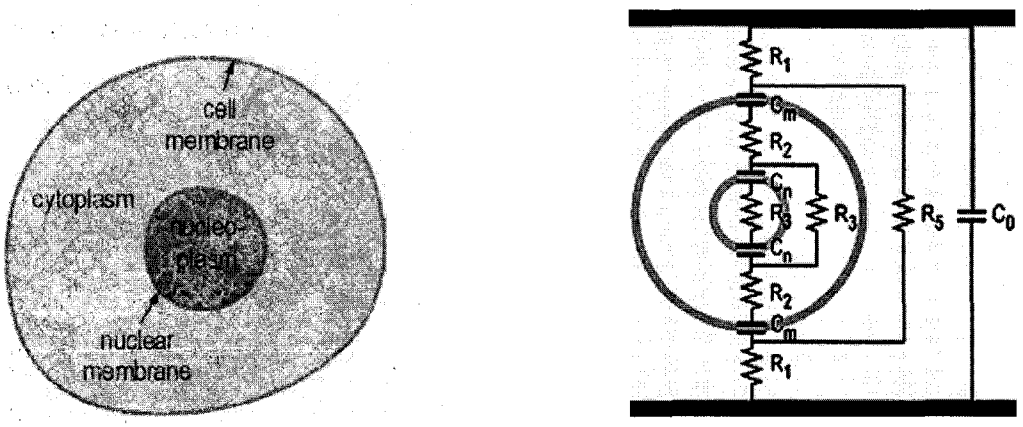


Fig. 2.2. Simplified model of cell (left) and its equivalent electrical model (right)

## 2.3 Intracellular Manipulation

Most pulsed electric field effects focus on the outer plasma membrane. When the potential difference across this membrane reaches a critical value or the threshold required for voltage gating effects, a non-linear effect called electroporation occurs. Electroporation is a term given for the pore formation on cell membranes caused by an external electrical field. This is also known as electropermeabilization. Although not fully understood, it is believed that pore formation generates large openings in cell membranes, allowing for transfer of large molecules across the cell membrane. The critical membrane voltage for electroporation is approximately 1V (19). This electroporation effect is reversible and the cell survives if the electric field is neither too high, nor too prolonged. The charging time constant for the plasma membrane is a measure of the time during which the cell interior is exposed to the applied electric field. According to Schwan's theory of oscillating electric fields, the outer membrane becomes transparent if the duration of the pulse is lower than the outer membrane's charging time constant. If the amplitude of this pulse is sufficiently high to porate the sub-structural membranes, then there can be poration of inner organneles without damage to the outer membrane. The analytical model supporting this hypothesis along with the equations and supporting literature is provided in Appendix B. The schematic of the blumlein pulse generator to along with the pulse produced with this principle is shown in Fig. 2.3. The ultra-short, very high amplitude rectangular pulses generated from this blumlein line are generally used for the application of Pulsed Electric Fields on cells. This technique is new and has been termed as intracellular manipulation or intracellular electroeffects by Dr. Schoenbach's group at ODU (17). From a practical standpoint, electrical pulsed technology could be useful for various biological applications ranging from cellular electroporation, injection of xenomolecules e.g., hormones, proteins, RNA, DNA and chromosomes, the electrofusion of dielectrophoretically aligned cells, and the non-thermal destruction of micro-organisms (20).

There appear to be inherent advantages in using *short electric pulses*. These include:

(i) Negligible thermal heating,

(ii) The ability to develop large electric fields and peak powers, with a lower energy input, and

(iii) The capacity to create large trans-membrane potentials across *sub-cellular organelles*, such as the mitochondria. This provides a method of reaching into the cell interior that is not possible with slower duration voltage pulses.

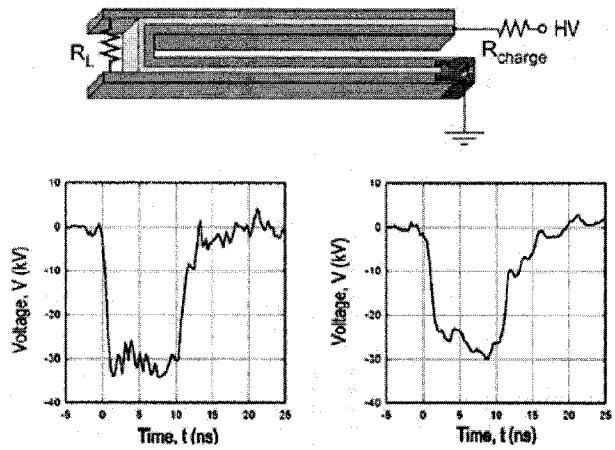


Fig. 2.3. Schematic of Blumlein Pulse Generatore (above) and temporal development of pulse with 10Ω matched load and with cell suspension ($\varepsilon_r$=80).

## 2.4 Summary of nsPEF Experimental Results and Oservations

Ultra-short, high-field pulses open the way to targeted and deliberate apoptotic cell killing (e.g., of tumor cells). Though the exact mechanism has not been identified, it appears that there could be several pathways that can help attain this desired goal of apoptotic cell death. These include Phosphatidyl-serine (PS) externalization that marks a cell for macrophage action, *cytochrome c* release that triggers caspase activation, DNA damage, irreversible field-induced changes to ion-pumps and voltage gated channels, etc. As has been recently reported, voltage-variations across the mitochondrial membrane can induce *cytochrome c* release via a two-step process (21, 22). The likely channel involves

a field-induced disruption in the electrostatic binding of *cytochrome c* with the inner mitochondrial membrane. To understand the serious effects caused by these ultra-short pulses, experiments have been done and are underway at various research centers. Some of the experimental results along with the observations have been summarized below.

### 2.4.1 Primary effects of nsPEF's

Experiments of nsPEF's on eosinophils show plasma membrane integrity. Eosinophils are one of the 5 different types of white blood cell and are characterized by large granule like structures when the cells are stained. This happens as the cells are loaded with calcein-AM, a dye that enters cell through plasma membrane and get trapped in the cytosol. When nsPEF's are applied on these cells, they began to fluoresce brightly and remain intact in the cells. The stains were also found inside the nucleus/inner organneles. This indicates some breaching of inner organneles. This is shown in Fig. 2.4. The retention of this dye inside the cell is strong evidence for plasma membrane integrity. Pulses of duration 50ns and amplitude of 60KV/cm are applied to the cells in these experiments.

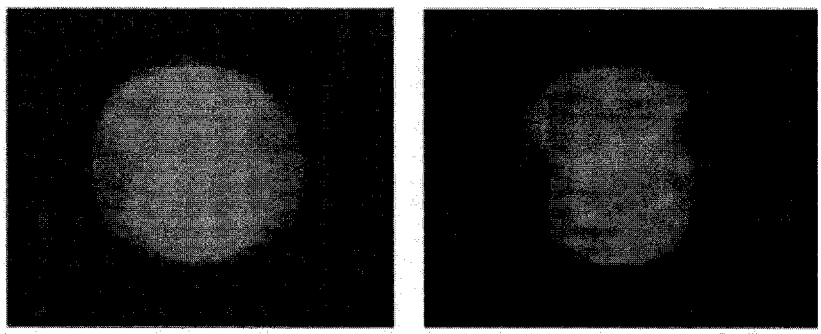

Fig. 2.4. HL-60 cells before (left) and after (right) pulsing (17).

The effect of nsPEF's on DNA has been explored using acridine orange (AO), a fluorescent dye that is able to permeate the plasma membrane, nuclear membrane and other inner organelle membranes. AO interacts with DNA and RNA by intercalation or electrostatic attraction (as DNA and RNA are highly charged). Experimental results of short-pulses on cells loaded with AO have shown that the intensity of AO fluorescence in the inner organneles and nucleus decreases after pulsing. This validates the hypothesis that inner membranes get breached after the application of these pulses. This is clearly shown in Fig. 2.5. So, nosPEF's can disrupt (or porate) the intracellular membranes without disturbing the plasma membrane integrity. This is regarded as the primary effect of these short pulses.

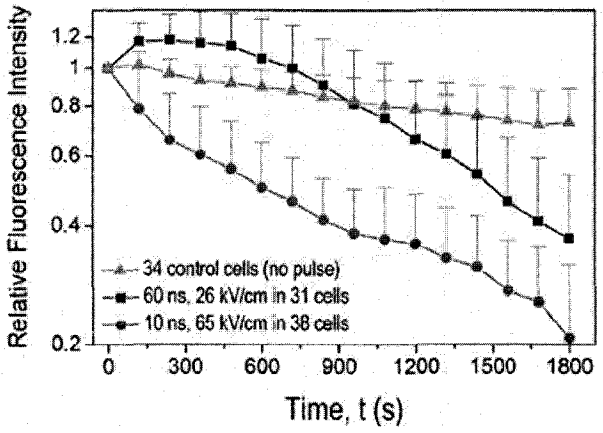


Fig. 2.5. AO fluorescence results on control and pulsed cells (17).

### 2.4.2 Secondary Effects of nsPEF's

The two basic cell death mechanisms known are necrosis and apoptosis. The difference between these two types is the biochemical mechanims that cause their death and the response of the surrounding cells on their occurrence. Both of these mechanims involve ultimate loss of plasma membrane integrity. However, for necrosis, a loss of

membrane integrity is the primary insult followed by inflammation, pain or scaring in surrounding cells. For apoptosis, there are other intracellular signaling mechanisms followed by the final disassembly of the cell. In vivo, the apoptotic cells are removed by phagocytosis, leading to the ultimate loss of membrane inside the phagocyte. Phagocytosis begins with the neutrophil or macrophage flowing around the pathogen and engulfing it so that it winds up enclosed in a phagosome. In vitro, there are other mechanisms to report apoptosis. These include PS externalization, caspase activation, intracellular calcium release and release of Cytochrome c from mitochondria seen by the apoptotic markers. These mechanisms are shown in Fig. 2.6 below.

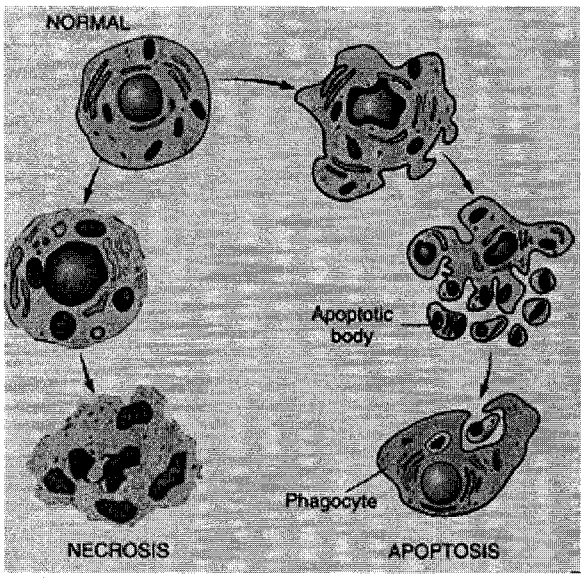


Fig. 2.6. Apoptosis and Necrosis in Cells.

Having given a brief description of the cell death mechanisms and with the background of primary effects of ultra-short pulses on cells, it looks clear that apoptosis is one of the main objectives to be achieved with these nsPEF's. A brief explanation on the experimental results showing secondary effects in cells is provided in the next section.

### 2.4.2.1 Apoptosis Induction with nsPEF's

Annexin-V-FITC flouroscence indicates externalization of PS, which is a marker for apoptosis. It was shown that ultrashort pulses induce apoptosis at higher electric fields. For 10ns pulse, an electric field of 300KV/cm caused Annexin-V to fluoresce, while 60ns pulse required 40KV/cm for PS to externalize. This is shown in Fig. 2.7. The electric fields were chosen such that the energy density is approximately the same. The energy density (W) is given by

$$W = \sigma E^2 \tau, \tag{1}$$

where $\sigma$ is conductivity of suspension, E is electric field and $\tau$ is duration of the pulse.

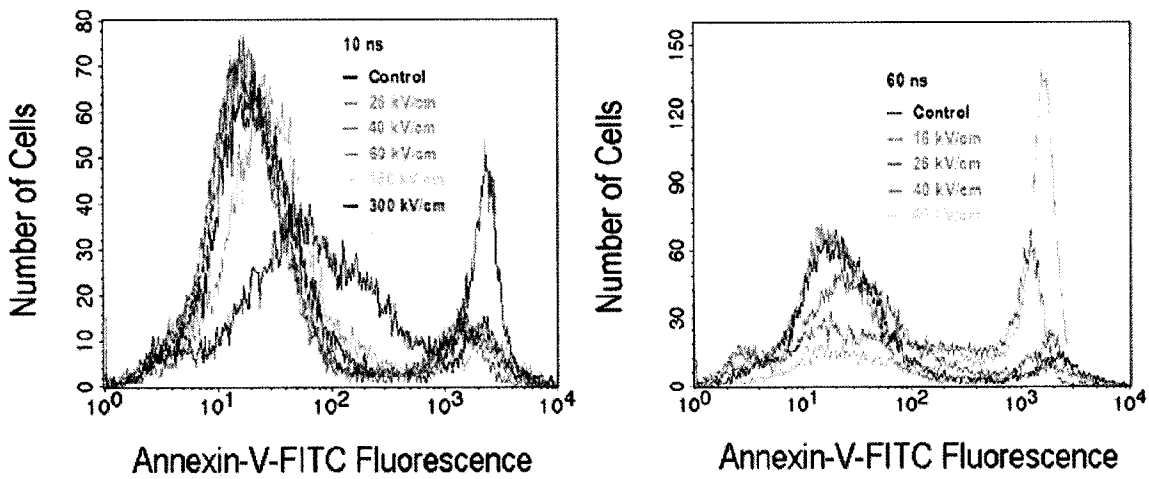


Fig. 2.7. Annexin-V-FITC bounds cells showing apoptosis (12).

The following salient features have emerged from these studies of cellular responses to high-intensity, pulsed electric fields.

(viii) Apoptosis has been observed (8) for cells subjected to the short electrical pulses.

(ix) Multiple pulses have been observed to do more irreversible damage than single-shot electric shocks.

(x) Externalization of phosphatidylserine (PS) was shown to occur in response to a nanosecond pulse for average electric fields above 2 MV/m.

(xi) A distinct polarity effect has been observed, with the *externalization predominantly occurring at the anode end.* In addition, asymmetry in transmembrane potentials at the anodic and cathodic poles have been demonstrated.

(xii) Calcium is released from the intracellular endoplasmic reticulum in response to external voltage pulses. This could be a vital element in induction or possible suppression of cell signaling.

(xiii) Molecular uptake has been shown to be delayed process as compared to conventional electroporation that utilize smaller electric fields and longer time durations.

(xiv) DNA damage in cells due to the ultrashort pulses has been observed.

In the next few sections, some details are provided about the cell membrane, X-ray crystallography of bilayers, recent experiments on bilayers and some background information of computer simulations on cells. A detailed explanation of the molecular dynamics simulation technique is provided in Chapter III, while the results achieved in this work are reported in Chapter IV.

## 2.5 Cell Membranes

Cell membranes are made up of lipids as well as proteins as shown in Fig. 2.8. The ratio varies enormously in different cell types. In the myelin membrane of nerve cells, proteins make up only 18%, while the rest of it is lipids. On the other hand, the inner mitochondrial membrane contains 76% of proteins (23). The diversity in lipid composition of typical membranes is equally large. The most commonly found molecules in membranes are glycerophospholipids, e.g. phosphatidylcholine, phosphatidylethanolamine, phosphatidylglycerol. Prefixes like "dipalmitoyl" indicate the

length and type of the extended hydrocarbon chains attached. Large fraction of the plasma membrane of mammalian cells constitutes cholesterol and many membranes also contain carbohydrates bound to either proteins or lipids. Likely reason can be that these components alter the packing properties of the membrane.

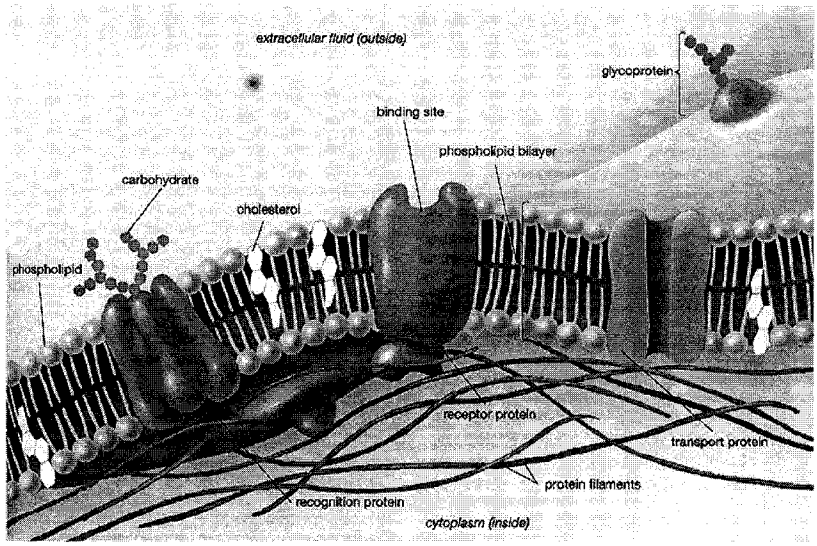


Fig. 2.8. Cell Membrane (31).

A membrane is thus a relatively complex structure. Despite this complexity, the lipid molecules determine all the fundamental physiochemical properties of membranes. So, in order to better understand membranes it has proven very useful to start by studying pure lipid bilayer systems. These lipid molecules also provide basic functionality and flexibility of the membrane. This type of "soft" material properties are much less studied than static ones like protein structure, since they are rather difficult to resolve experimentally.

## 2.6 Bilayer Experiments & Simulations

Structural biology is the study of the architecture and shape of biological macromolecules e.g., lipid bilayer, proteins and nucleic acids. These biomolecules are too small to see in detail even with the most advanced light microscopes. X-ray crystallography, NMR spectroscopy, ultra fast laser spectroscopy, electron microscopy are some of the techniques, structural biologists use to determine the structures of these biomolecules. It has been experimentally possible to obtain high resolution X-ray structures of individual lipids from crystalline bilayers at low temperatures and limited hydration (24, 25).

Having obtained the X-ray structures, the next thing computer scientists are interested in is to use this structure to carry out simulations. It is not easy to perform accurate simulations in general, and membrane systems in particular are very sensitive to the choice of force field. The only way that we can assess the results and ascertain that we are doing reasonable simulations is to compare with available experimental observations. The electron densities from X-ray diffraction and also NMR order parameters provide excellent tests for bilayer systems, and in particular DPPC bilayers. The simulations done in the past (26) reproduce these properties accurately, hence we have fair reason to use these bilayer systems to perform other simulations. The availability of powerful computers has opened new ways to study lipid bilayers in atomic detail. Computer simulations now offer a detailed picture of a time-dependent structure and dynamics of membranes, or a trajectory of lipids in bilayer, which help answer a lot of research questions and issues.

Since most of the effects of electropulsing is on the cell membranes as well as the inner organelle membranes, it will be interesting to investigate the structure and function of the lipid membrane during and after electroporation at molecular level. Since the lipid membrane thickness is of the order of few nanometers and the pulse duration being in

nanoseconds, the molecular dynamics simulation scheme is a very good tool to use. The molecular dynamics technique has developed over the last decades from a method to study the dynamics of liquids of solid spheres and Lennard-Jones particles to a versatile method to study many different types of systems at atomic resolution (27). In the field of biochemistry, a large study on MD simulations on proteins in vacuum and in solvents is available. The development of this particular use of MD was greatly stimulated in 1980's, when a number of general-purpose force fields for water, proteins and DNA along with computer programs for simulations like AMBER (28), CHARMM (29) and GROMOS (30) are available. Chapter III provides adequate and relevant information on the molecular dynamics simulation technique along with a detailed description of the force-fields.

### 2.6.1 Dynamical Bilayer Properties

The structure of the lipid bilayer can be revealed from X-ray crystallography. The commonly occurring molecules in this dissertation report are neither integral membrane proteins nor the nucleic acids, but lipid molecules. One of the lipid molecule structure is shown in Fig. 2.9. These lipid molecules have a dipolar charged head groups and so are hydrophilic, or in other words, they tend to stay near water. The tails of these molecules are comprised of saturated fatty acids and so are hydrophobic and tend to stay away from water.

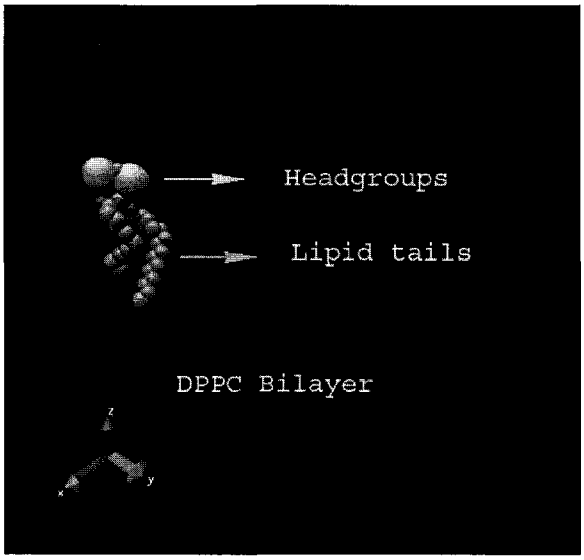


Fig. 2.9. Schematic of a DPPC lipid molecule.

The rate and extent of motions of the lipid molecules in bilayer are usually very important to their function. The Singer & Nicolson fluid mosaic model (31), and more recent computer simulations, have helped us understand that membranes are essentially "microscopic seas" of lipids with integral proteins floating around. One of the interesting properties of these membrane systems is that this dynamics is not limited to the individual lipid molecules, but is a collective mesoscopic effect. This can be clearly understood in terms of bending and stretching elasticity found from experiments and shown at atomic level with computer simulations (32).

### 2.6.2 Lipid Chain Relaxation

The "soft" nature of the hydrocarbon interior is one of the most important features of a bilayer systems as the complex interactions between these chains are responsible for the expansive pressure balancing the headgroup attraction. These motions fall in a very wide range from picosecond vibrations to slow diffusion in microsecond scale. Nuclear Magnetic Resonance (NMR) spectroscopy is one of the experimental tools to study these

diffusion processes and in turn can validate the computer simulations. These simulations in turn can provide additional atomic detail and can reveal the interactions responsible for the relaxation of lipid chains.

### 2.6.3 Computational Structural Biology

Structural biology would not have advanced much without high performance computing as stated by Michael Levitt in his nature - structural biology - article (33). In recent years, growing computational resources and power along with the improved algorithms have led to more complicated simulations and for longer times (34). Computer simulations to understand various properties including surface area per lipid, surface tension, electron density and deuterium order parameters has been ongoing in the last decade (35). These simulations are mostly confined to pure lipid bilayers. There were also computer simulations done to understand the effect of salt concentration on the structure of bilayer e.g., DPPC bilayer system (36). Simulations having mixture of different bilayer systems were also carried out e.g., mixture of DPPC and DPPS (37). One of the bilayer structures having mixture of PC and PS is shown in Fig. 2.10. Simulations to include integral membrane proteins in the bilayer systems have also been done by various groups (38, 39). Recently many simulations by several groups (40) are underway to investigate the voltage-gating mechanism of the ion channels after the crystallization of the KvaP channel structures (41). A molecular model of KcsA potassium channel is shown in Fig. 2.11. In the next few sections, the background information on the computer simulations that have performed during this dissertation work is provided.

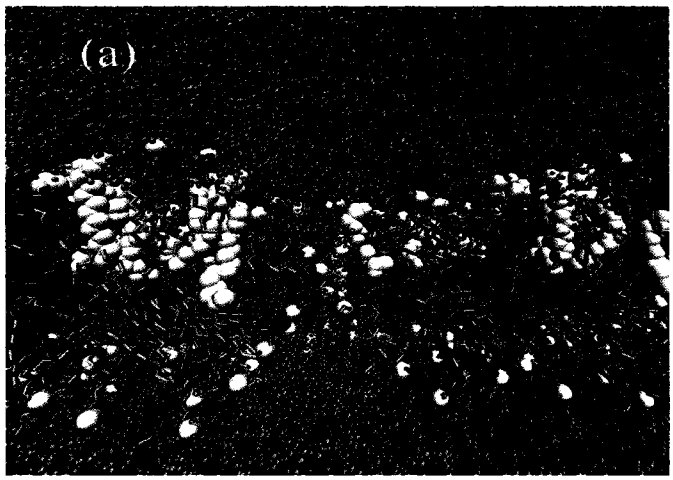


Fig. 2.10. PS molecules are embedded in DPPC bilayer. PS are shown in white, PC molecules in cyan, headgroups in yellow and green, water molecules in ice blue.


Fig. 2.11. Molecular Model of Voltage gated Potassium Channel.

## 2.7 Bilayer Pore Formation

As earlier discussed, the application of pulsed electric fields to cells or tissues permeabilizes the cell membrane and is thought to produce aqueous filled pores in the bilayer system. This process is referred to as membrane breakdown, electropermeabilization or membrane breakdown. The molecular processes involved in this process are still not properly understood. The aim of this study is to bring about a very detailed molecular level picture using molecular dynamics simulations. It was shown in a recent study (42) that electroporation takes place in two stages. First water molecules organized in single file like wires pentrate the hydrophobic core of the bilayer and slowly defects start to form eventually completing the pore formation process. These observations were at constant electric field and were reported to show electric field effects on cells. Though these simulations showed the process of electroporation at high dc fields clearly, there is no evidence of support to use high electrical fields in the range of 0.5V/nm in these simulations.

Our group has calculated the transmembrane potentials generated across the inner membranes upon the application of ultra-short pulsed electric fields. The mathematical model used in this computation consists of a distributed circuit model with current continuity equations, and a coupled Smoluchoswki equation for pore development. In this model, the entire cell volume is broken up into finite segments, and each segment is represented by a parallel RC combination to account for current flow and charging effects. These calculations of transmembrane potentials generated across inner and outer membranes are given separately as a supplementary material in Appendix B. These transmembrane potentials generated across the inner membrane were taken as an input parameter for molecular dynamics simulations on DPPC bilayer. The details of this simulation technique are given in Chapter III, while the results of bilayer pore formation along with nice images are given in Chapter IV.

## 2.8 High Electric Field Effects

The notion central to the electroporation process is the gradual but well-organized, structural re-arrangement without any molecular detachment or break-up (4). It has also been shown that the presence of localized membrane heterogeneities and defects (such as charged DPPS molecules) enhance the electroporation process (43). Preferential electroporation at the anodic side can then result, and this has been demonstrated both experimentally (44) and through molecular dynamics (MD) simulations on coarse-grained model of DPPC (43). The traditional electroporation model seems to work well for relatively low-to-moderate electric fields (200 V/cm–5 kV/cm). However, it appears to be inadequate in explaining several of the observed phenomena at high electric field strengths. The various inadequacies with regards to experimental reports are listed below. (i) The high-field experimental data indicates strong conductivity increases of the cell solution at the very beginning of a high-voltage pulse (45). Our current experimental data sets (discussed in results section in Chapter IV) show conductance increases far exceeding values that might be predicted on the basis of simple membrane electroporation or dissolution. Also, such increases cannot be attributed to field-induced Wien effects. (ii) The fast decrease in conductance, observed after the pulse cessation, is not compatible with pore shrinking or sealing. The re-sealing process for electro-pores is known to be slow and can take up to several seconds to minutes (46). An additional point of interest is the vesicle formation at the plasma membrane (i.e., blebbing) that has been observed (47). This aspect is not addressed by the electroporation models. (iii) Recent reports by Tekle et al. (44) show loss of the phospholipid membrane during high-voltage pulsing. This phenomenon was shown to occur in addition to a pore formation process. Their results demonstrated that up to 14 percent of the membrane surface could be lost upon electric field application. (iv) Finally, it has been well documented that the application of electric pulses facilitates the penetration of large molecules through the membrane. This probably implies the creation of large pores. For example, in multi-lamellar systems such as the stratum corneum, contributions to structural changes arise from electro-thermally induced vesicle formation. However, electroporation theory, as applied to the short-duration, high-intensity pulses, predicts

relatively small nano-pores. Also, simple nano-pore formation alone cannot explain the transport of polyelectrolytes and DNA. Here, we hypothesize that not only are aqueous pores formed within the lipid membranes, but that nanoscale membrane fragmentation occurs, possibly with micelle formation. This effect would produce conductivity increases beyond simple electroporation and display a relatively fast turn-off with external voltage. Molecular dynamics simulations on high electric field effects, the results of which are presented in Chapter IV, qualitatively support our hypothesis. The scheme of setting up the simulations is explained in detail in Chapter III.

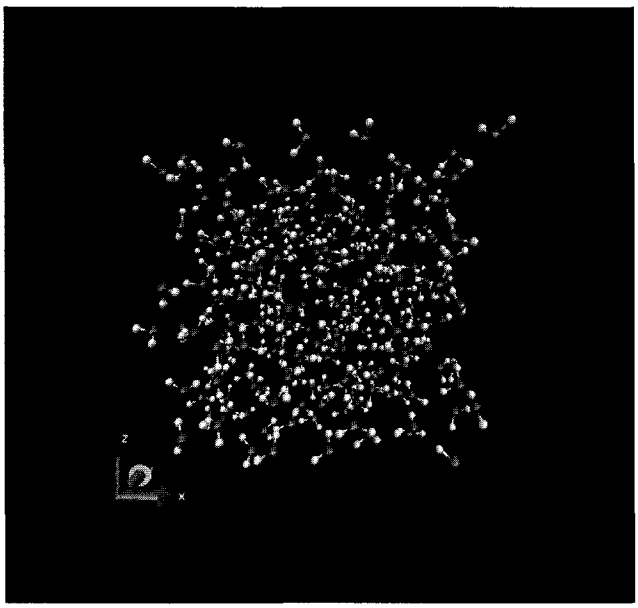

Fig. 2.12. Simple Point Charge water model.

## 2.9 Transport Parameters

Water is regarded as the most important biological solvent. Almost all the bilayer simulations include water as the solvent. It is so important that most biomolecules would not maintain their structure without the surround solvent. One of the water models is

shown in Fig. 2.12, which is known as Simple Point Charge (SPC) model. The Fig. 2.12 shows a system of size 1.8 nanometer cube enclosing 216 water molecules. Ionic transport through membranes involving ion and nutrient exchanges is critical to cell survival. The pertinent microscopic transport analysis can rigorously be treated at several levels that include density functional theory (48), molecular dynamics (49), or Brownian motion (50). However, such microscopic calculations are too time consuming and computationally almost intractable for most practical applications. Simplified schemes, such as those based on drift-diffusion analysis or the Smoluchowski equation (51), remain the preferred approaches in bio-systems. Such methods are characterized by local parameters that include diffusion coefficients, ionic mobilities and permittivity. It, therefore, becomes important and relevant to accurately evaluate these local parameters for lipid environments. The focus and interest in this area has increasingly been shifting to high field conditions—a domain usually characterized by membrane poration. In evaluating transport through porated membranes, several aspects such as the dynamical many-body effects of the lipids, the surrounding water and their associated dipoles, and confined space effects need to be carefully considered and evaluated. The present study attempts to provide such an analysis for the transport parameters of the aqueous medium with inclusion of microscopic details. The primary application of this work would be for subsequent coarse-grained, macroscopic transport across porated membranes. The details of the simulation technique are given in Chapter III, while Chapter IV gives the simulation results.

## 2.10 Electric Field Induced DNA Damage

Most of the experimental results come from electrodelivery of plasmid DNA's with traditional electroporation pulses (52). Molecular dynamics simulations were also done to show this electrodelivery of plasmid DNA's and support the above hypothesis (53). There were no simulations done to show DNA damage upon the application of traditional electroporation pulses, but there are results which show possible DNA damage upon the application of nsPEF's (54).

Recently it has also been shown that DNA strands conduct electricity upon the application of a potential across DNA molecules (55). This motivates us to see the effect of nsPEF's on DNA in atomic detail.

Here through MD simulation, we show that these nsPEF's induce DNA damage, which are central part for the functioning of the cell. The molecular dynamics parameters used in this work is described in detail in Chapter III, while the results are presented in Chapter IV.

## 2.11 Electric Field Induced Intracellular Calcium Release

It has been shown that nsPEF (nanosecond Pulsed Electric Field) pulses can trigger apoptosis in Jurkat and HL-60 cells. Application of these pulses results in a rapid rise of intracellular calcium (56). The rise in calcium levels depend on the pulse duration, amplitude of the pulsed electric field, and the number of pulses applied. Pulse-induced intracellular calcium release can explain or give an insight into cell signaling mechanisms.

Monitoring calcium concentration directly inside the endoplasmic reticulum or other sub-structures has been difficult to achieve in cells. If this calcium inside these intracellular stores can be driven into cytoplasma by agonists, then they can be evaluated using calcium flouroscent indicators. On the other hand, application of nsPEFs on cells increase calcium concentrations inside the cytoplasma. This can be due to release from intracellular organs (after getting nano-porated) followed by calcium entry via the plasma membrane through a mechanism known as capacitative calcium entry. So, experimentalists conduct these tests in a media with and without calcium and compare the results to obtain intracellular calcium concentration.

The experimental ways of depleting intracellular calcium is by the addition of reagents that deplete calcium as mentioned above. Thapsigargin is a reagent which empties ER calcium stores and at the same time, not affecting calcium in mitochondria. nsPEF's are applied to cells after they are treated with thapsigargin (or UTP). The intracellular calcium increase found is very little compared to direct application of nsPEF's on cells untreated with thapsigargin. These experiments suggests that pulse induced intracellular calcium release is dependent on the operation of the calcium stores of ER. This validates the increase in intracellular calcium caused by nsPEF's is mostly from ER, although there might be a small pumping of calcium from mitochondria which can be neglected. The release of calcium from ER is also shown to contribute to calcium signaling (57). This phenomenon therefore originates within the cell and is not a disturbance in the plasma membrane.

A very interesting secondary effect has also been reported in the context of such electrically pulsed calcium release. It has been reported that a second pulse of lesser intensity than the initial pulse is almost totally ineffective in inducing any calcium release within cells (58). However, with second pulse intensities either equal to or greater than the first, a small to moderate calcium response could be evoked. This phenomena is not well understood at present, though it is suggestive of a number of plausible explanations. For example, the electrically induced calcium release might conceivably deplete the endoplasmic reticulum to a large extent after the first pulse. This would then leave very little calcium within the intracellular stores for possible release during the second pulse. Alternately, conformational changes and electrically induced charge movements (59) within the ER membrane might create electrostatic barriers (or other "damage") that affects subsequent calcium release. The modeling part of this work is neatly described in Chapter III, while Chapter IV is dedicated to the corresponding results.

## 2.12 Time Domain Dielectric Spectroscopy

Information on dielectric parameters of cell is very essential as they dictate the fashion of electric field through it. The two electrical properties that determine the electrical characteristics of any material are the dielectric constant relative to free space ($\varepsilon$) and the conductivity ($\sigma$). The complex relative permittivity is defined as:

$$\varepsilon^* = \varepsilon' - j\varepsilon'', \tag{2}$$

$$\varepsilon^*(\omega) = \varepsilon(\omega) - j\sigma(\omega)/\omega\varepsilon_0, \tag{3}$$

where $\varepsilon'$ and $\varepsilon''$ are the real and imaginary parts, respectively, $\varepsilon$ is the relative permittivity, $\varepsilon_0$ is the permittivity of vacuum, $\sigma$ is the conductivity, $\omega$ is the angular frequency, and $j = \text{sqrt}(-1)$. The relative permittivity and conductivity of materials decrease and increase, respectively, with increasing frequency. Sometimes, instead of conductivity $\sigma$, the loss factor $\varepsilon''$ is plotted against the frequency, giving rise to a peak at characteristic frequency. If the dc conductivity ($\sigma_{dc}$) is not negligible, the loss factor is calculated from $\varepsilon'' = (\sigma - \sigma_{dc})/\{\omega\varepsilon_0\}$.

When dielectric spectra are measured for biological tissues and cell suspensions over a wide frequency range of 1Hz to 10GHz, three distinct dispersions termed $\alpha$-, $\beta$-, and $\gamma$- along with a smaller dispersion $\delta$- are generally found (60). Dielectric dispersion refers to regions of operating frequencies within which strong absorption or dissipative energy losses are typically encountered due to collective interactions with the medium. These major dispersion characterizations and their frequency ranges, along with the type of biopolymers that fall in these categories, are shown in Fig. 2.13. The "alpha" dispersion appears at frequencies less than few KHz and cannot be easily measured

because of the interference from electrode polarization effects. There is not much evidence of a relaxation process. This dispersion could originate from the displacement of counter ions surrounding charged membranes. The "beta" dispersion (100KHz – few MHz) is due to interfacial polarization, being mainly attributed to the existence of plasma membrane of cells. The "gamma" dispersion is due to the Debye-type relaxation of water molecules above few GHz. The "delta" dispersion found between "beta" and "gamma" is due to bound water and other biomolecules solvated in extracellular and intracellular media of the tissue.

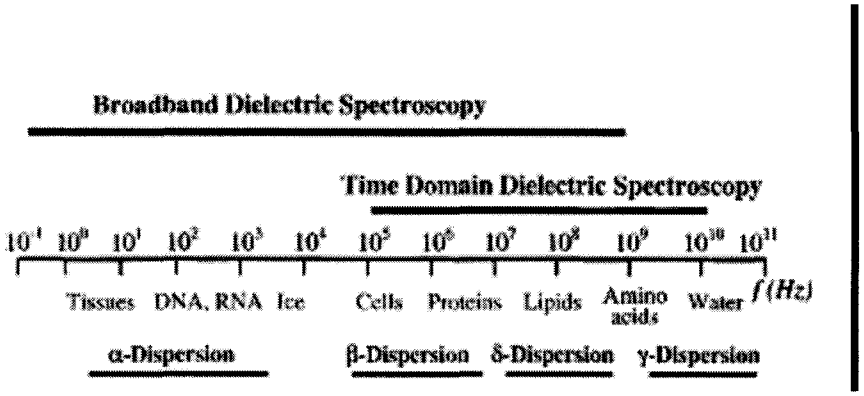


Fig. 2.13. Frequency Dependent Dispersion Characterizations (62).

The traditional methods of determining permittivity rely on measurements in the frequency domain. The common feature of all such methods is that the solution is contained in a sample holder and its complex permittivity measured at various discrete frequency points. It is not, however, possible to devise one piece of apparatus or a single technique to cover the entire frequency range. This is so because of problems in measuring both the very low frequency spectra and very high frequency spectra.

At the low-frequency end of the spectrum, generally bridge techniques are used. Although, these can, in theory, be extended down to d.c. levels, practical measurements on conductive biological solutions are difficult below a few KHz because of electrode

effects. The electrode polarization effect and the possibility for overcoming this problem in described later. At higher frequencies, transmission lines are employed. They are sub-divided into coaxial lines and waveguides. The frequency of a coaxial line in practice is from few tens of MHz to around 12 GHz. Above 12GHz and below 100GHz, waveguides are employed. Above 100GHz free space methods are used, but these are relatively unimportant for biological solutions.

Alternative methods can be classified as time domain techniques, generally known as time domain reflectometry (TDR) or time domain spectroscopy (TDS). These are advantageous over frequency domain dielectric spectroscopy (61) because it requires only one pulse to determine all frequencies of interest rather than conducting measurements at individual frequencies (62). This is particularly important during biological measurements, when the cells have a limited lifespan and the events being considered may occur quickly.

Recently, single-particle analysis has been developed and becomes increasingly important especially in medical and biotechnological researches. For the single-particle analysis electromechanical techniques, such as electrorotation and dielectrophoresis, are used instead of conventional dielectric spectroscopy. Alternatively, imaging techniques with a scanning fine probe are also available in the single-particle analysis. This is out of context in the present work, as the pulsing is generally done on cell suspension, instead of a single cell. So, it is more relevant to use multi-particle analysis like TDDS than electrophoresis.

Dielectric spectroscopy had its origin in the late 1800's and early 1900s and played a major role in the emergence of electrophysiology (63). Hoeber's observations that red blood cells conducted electricity differently at low and high frequencies led to his

speculation that a membrane must be present to separate the intracellular components from the extracellular ones. The initial application of dielectric spectroscopy is often traced back to the pioneering work of Fricke (64). Improvements in presentation and analysis can be traced back to the work of the Cole brothers, who developed a relationship between the real and imaginary components of permittivity for polar liquids that is now referred to as a "Cole-Cole plot". However, the early methods of dielectric spectroscopy generally involved placing the substance between the two plates of a capacitor and measuring the change in complex impedance as the frequency changed. Fellner-Feldegg developed a procedure previously used for cable testing that involved using a pulse simultaneously containing all frequencies of interest. It was this work in time domain reflectometry (TDR) that has been developed into TDDS. Over the years, TDDS has been a versatile tool, providing measurement and insight in the dielectric behavior of erythrocytes, lymphocytes, proteins, erythrocytes under different glucose conditions, micro-emulsions, and tobacco mosaic virus (65). Recently, it has also been shown that dielectric properties do vary upon membrane disruption (66). The main objective of this work is to find the dielectric properties of the cell before and after electroporation and use this information in mathematical models based on electroporation. The principle of TDDS on biological suspensions along with the results (not published) is provided in Appendix A.

This completes the literature review on electropulsing effects on cells along with the computer simulation on bilayers. This chapter was also dedicated towards going through the background information and motivation towards this dissertation work.

# CHAPTER III

# COMPUTER SIMULATIONS

## 3.1 Introduction

Computer simulations allow us to study system properties at a microscopic level and to investigate phenomena on ultra-short time scales that may not be accessible to experimental detection. In addition, the influence of several individual interactions (e.g., the Coulomb or the hydro-phobic interaction) can be gauged, and collective many-particle influences can be assessed. In the context of cellular effects, such computer simulations are all the more important since it is not possible to probe the electrical responses at the cellular level. Use of simulations is very helpful in providing a fundamental understanding of the underlying phenomena and in a quantitative assessment of the relative magnitudes of various processes. Finally, simulations allow a convenient and quick mechanism to span, probe and evaluate a large parameter space. A range of simulation methods exist that span the macroscopic continuum approaches (e.g. the Smoluchowski equation (67)), to those based on the semi-classical retarded Langevin and Green's functions, to microscopic-kinetic analyses based on Brownian dynamics (68), Monte Carlo (69) or Molecular Dynamics (MD) (13,39).

Here we focus on the MD technique, as it provides the most comprehensive, time-dependent, three-dimensional nanoscale analyses with inclusion of the many-body aspects. The MD simulations are based on the assumption that classical Newtonian mechanics can be used to describe the motions of atoms, pseudo atoms, interaction sites or molecules, regardless of all-atom implementations or use of coarse grained models. However, no quantum calculations as may be needed to predict electron energies, wavefunctions, probabilistic occupancies etc. are performed. Hence, molecular dis-integration or chemical reactions are not addressed. In an MD scheme, the use of an all

atom model has the advantage of calculating properties of the system precisely, while the coarse-grained model has the advantage of speed-up that can be useful in the context of big systems responding on sub-microsecond scales.

## 3.2 Molecular Dynamics

MD simulation is a technique to calculate the equilibrium, non-equilibrium, and time-dependent properties of a classical many-body system. Molecular/ionic transport and dynamical changes in position or configuration, is usually the aspect of primary interest. Every observable quantity to be evaluated by this technique is based on a determination of the exact position and momenta of the particles in the many-body system at every time instant.

The concept of molecular dynamics was originally developed by Alder and Wainwright in the early 1950's as a technique to simulate a system of colliding hard core particles (70). It was later extended to continuous potentials and uniform time steps by Rahman (7). The underlying idea is actually rather simple, but it requires *a lot* of computing power even by today's standards. A short tabular listing of the various advances and milestones in MD work is given in Table 3.1.

Table 3.1. Few examples showing the rapid devolopment of MD simulations.

| System | Year | Authors | Atoms | Time |
|---|---|---|---|---|
| Hard Spheres | 1953 | Alder et. al. (70) | 108 | - |
| Water | 1971 | Rahman et. al. (7) | 648 | 2.2 ps |
| Protein in Vacuo | 1977 | McCammon et. al. (71) | 580 | 8 ps |
| Lipid Bilayers | 1988 | Egberts et. al. (72) | 5408 | 200 ps |
| Bacteriorhodopsin | 1995 | Edholm et. al. (73) | 18384 | 300 ps |
| Porine | 1998 | Tieleman et. al. | 65898 | 1 ns |
| Peptide folding | 1998 | Duan et. al. (74) | 9500 | 1 us |

## THE GLOBAL MD ALGORITHM

**1. Input initial conditions**

Potential interaction $V$ as a function of atom positions
Positions $r$ of all atoms in the system
Velocities $v$ of all atoms in the system

⇓

**repeat 2,3,4** for the required number of steps:

**2. Compute forces**

The force on any atom

$$F_i = -\frac{\partial V}{\partial r_i}$$

is computed by calculating the force between non-bonded atom pairs:

$$F_i = \sum_j F_{ij}$$

plus the forces due to bonded interactions (which may depend on 1, 2, 3, or 4 atoms), plus restraining and/or external forces.
The potential and kinetic energies and the pressure tensor are computed.

⇓

**3. Update configuration**

The movement of the atoms is simulated by numerically solving Newton's equations of motion

$$\frac{d^2 r_i}{dt^2} = \frac{F_i}{m_i}$$

or

$$\frac{dr_i}{dt} = v_i; \quad \frac{dv_i}{dt} = \frac{F_i}{m_i}$$

⇓

**4.** if required: **Output step**

write positions, velocities, energies, temperature, pressure, etc.

Fig. 3.1. Global Molecular Dynamics Algorithm (75).

## 3.3 The MD Algorithm

The aim of MD is to reproduce the time development of a system of $N$ interacting particles (e.g. atoms) with masses $m_i$ by directly solving Newton's equations of motion,

$$m_i \, d^2r_i/dt^2 = F_i \; i=1,2....N \quad , \tag{4}$$

where $\mathbf{r}_i(t)$ is the position of particle $i$. The momentary force $\mathbf{F}_i$ on each atom should be calculated from the interactions in the system. It is defined as the derivative (i.e., slope) of a potential energy function V that is determined by the positions of all the atoms,

$$F_i=-\nabla_{ri} V \, (r_1,r_2,..r_N) \quad . \tag{5}$$

The calculation of this potential function is a central part of the algorithm. There are many possible choices for the implementation of this function, and it is always an approximate compromise between a description as detailed as possible and one that can be evaluated fast on a computer. Its final appearance, together with the actual interaction parameters used in the simulation, is called the *force field.* Though various research groups have developed different force fields, most of them are closely related. A rough outline of the MD algorithm is shown in Fig. 3.1 above.

Basically, a force-field is built up from two distinct components:

- The set of equations (called the potential functions) used to generate the potential energies and their derivatives, the forces.
- The parameters used in this set of equations.

## 3.4 Potential Function & Parameters

The potential function described above can be divided into 3 parts.

1. Non-bonded: Lennard-Jones or Buckingham, and Coloumb or modified Coloumb. These interactions are computed on the basis of a neighbour list i.e., a list of non-bonded atoms within a certain radius.

2. Bonded: Covalent bond-stretching, angle-bending, proper and improper dihedrals. These interactions are computed on the basis of fixed lists.

3. Special functions: Position restraints and distance restraints. These interactions are also calculated based on the fixed lists.

### 3.4.1 Non-bonded Interactions

The non-bonded interactions contain a repulsion term, a dispersion term and a coulomb term. The repulsion and dispersion terms are combined in either the Lennard-Jones or the Buckingham potential. There can also be a Coulombic term because of the partially charged atoms. For all the simulations reported in this work, Lennard-Jones interactions and Coulomb interactions are considered.

#### 3.4.1.1 Lennard-Jones Interactions

The Lennard-Jones potential $V_{LJ}$ between two atoms equals

$$V_{LJ} = C^{(12)}_{ij} / r^{12}_{ij} - C^{(6)}_{ij} / r^{6}_{ij}, \tag{6}$$

where the parameters $C^{(12)}_{ij}$ and $C^{(6)}_{ij}$ depend on pairs of atom types, $r_{ij}$ is the distance vector.

Hence the force $F_i(r_{ij})$ derived from this potential is:

$$F_i(r_{ij}) = ( 12\, C^{(12)}_{ij} / r^{12}_{ij} - 6\, C^{(6)}_{ij} / r^{6}_{ij} )\, \mathbf{r}_{ij}/r_{ij}, \tag{7}$$

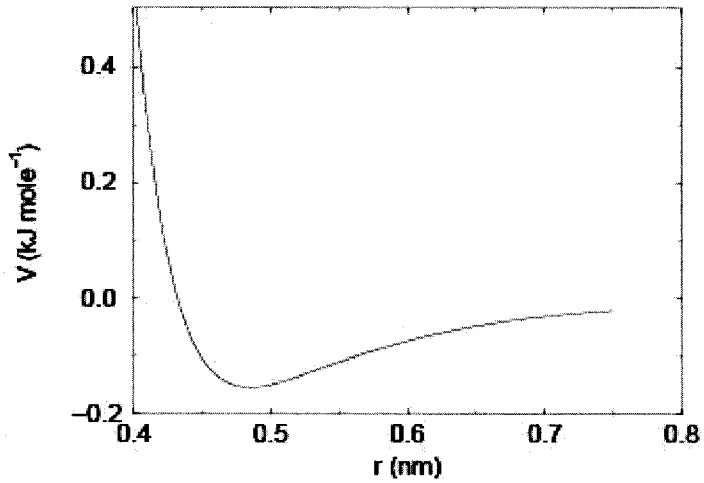


Fig. 3.2. Lennard-Jones potential (75).

Fig. 3.2 shows the Lennard-Jones potential of two particles. Initially when the distance between the two particles is very close, the repulsion is very high and vice versa if the distance between two particles increases, there is attraction between them till a cut-off point.

### 3.4.1.2 Coulomb interactions

The Coulomb interaction $V_C(r_{ij})$ between two charged particles is given by:

$$V_C(r_{ij}) = q_i q_j/(4\Pi\varepsilon_o\varepsilon_r r_{ij}), \quad (8)$$

Where qi, qj are the charges of particles i,j, $\varepsilon_o$ is the permittivity of vacuum, $\varepsilon_r$ is relative the permittivity of the medium and $r_{ij}$ is the distance vector.

The force $F_i(r_{ij})$ obtained from this potential is then given by:

$$F_i(r_{ij}) = q_i q_j/(4\Pi\varepsilon_o\varepsilon_r r^2_{ij})\ \mathbf{r}_{ij}/r_{ij}, \quad (9)$$

Fig. 3.3 below shows the Coloumb interaction between two particles of like charge. Initially when the distance between the two particles is less, there is high repulsion, which decreases as the distance between them increases. The plot shows a legend of pure coloumb potential, couloumb potential with and without reaction field. In calculations pertaining to some physical quantities like permittivity, it becomes necessary to consider all the charges in the simulation box without cut-off. This will be computationally expensive and hence a term known as reaction field is later on developed with these kind of simulations. The details of these various terms and physical significance are discussed in the results section of this dissertation report.

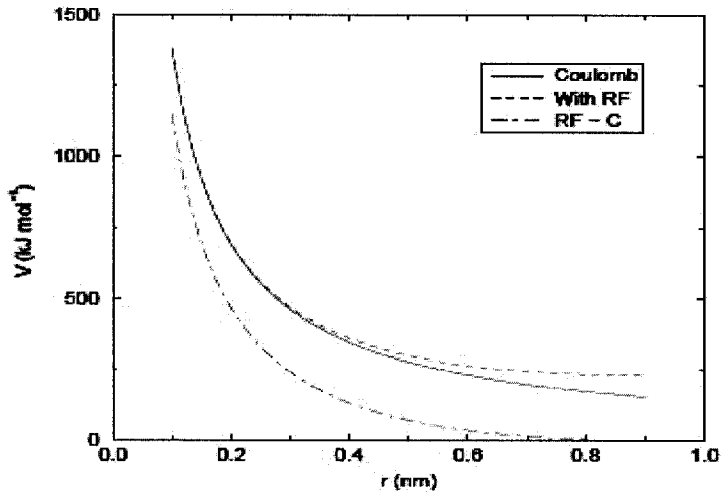


Fig. 3.3. Coulomb potential (75).

### 3.4.2 Bonded Potentials

The bonded interactions are based on a fixed list of atoms. These involve 3-body and 4-body interactions along with 2-body interactions as well. So, there are bond-stretching (2-body), bond-angle (3-body) and dihedral angle (4-body) interactions. There

is also a special type of dihedral interaction called improper dihedrals, which force atoms to remain in a plane or to prevent transition to a configuration of opposite chirality.

### 3.4.2.1 Bond-Stretching Potential

The bond stretching between two covalently bonded atoms is represented by a harmonic potential $V_b(r_{ij})$

$$V_b(r_{ij}) = 0.5k^b_{ij}(r_{ij} - b_{ij})^2, \quad (10)$$

where $k^b_{ij}$ is the harmonic force constant, $r_{ij}$ is the distance vector and $b_{ij}$ is the equilibirium bond length.

Hence the force $F_i(r_{ij})$ derived from this potential is

$$F_i(r_{ij}) = k^b_{ij}(r_{ij} - b_{ij})\,\mathbf{r}_{ij}/r_{ij}, \quad (11)$$

Fig. 3.4 below shows the bonded interactions between two particles. If the bond length is the natural bond-length, then the energy of the system will be zero. But if the bond length deviates from the initial equilibirium bond-length, then energy starts to build in the system. The equations for these interactions are similar to the energy related equations in two particles connected by a spring.

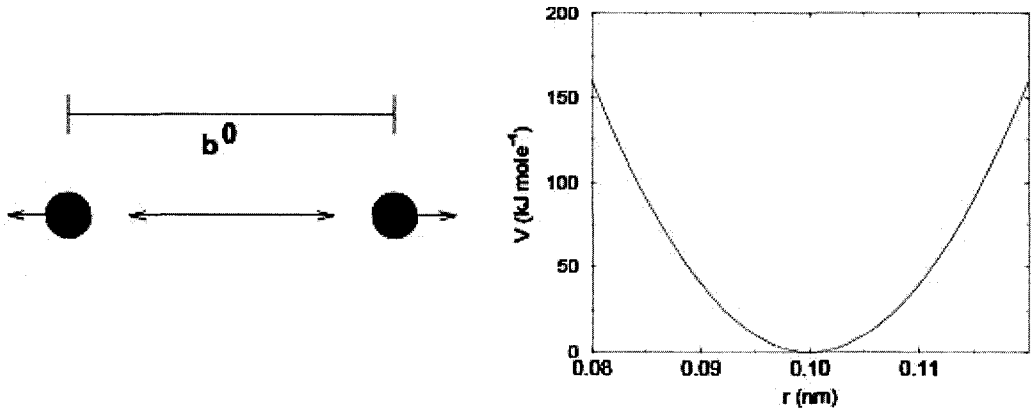


Fig. 3.4. Bond-stretching principle (left) and bond-stretching potential (right) (75).

### 3.4.2.2 Bond Angle Potential

The bond angle vibration between a triplet of atoms i-j-k is also represented by a harmonic potential $V_a(\theta_{ijk})$ on the angle $\theta_{ijk}$

$$V_a(\theta_{ijk}) = 0.5k^{\theta}_{ijk} (\theta_{ijk} - \theta^0_{ijk})^2, \quad (12)$$

where $k^{\theta}_{ijk}$ is the bond-angle force constant, $\theta_{ijk}$ is the bond angle between i-j-k and $\theta^0_{ijk}$ is the equilibirium bond angle.

Fig. 3.5 below shows the bond-angle potential generated in the system if there is any change in the angle between two adjancently connected bonds in the molecule.

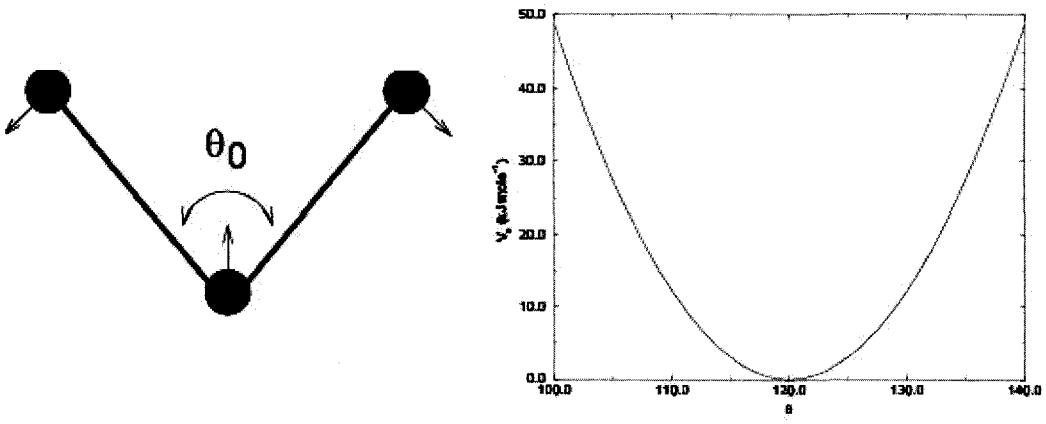


Fig. 3.5. Angle-vibration principle and bond-angle potential (75).

### 3.4.2.3 Improper Dihedrals

Improper dihedrals are meant to keep planar groups planar (e.g., aromatic rings) or to prevent molecules from flipping over to their mirror images. This is also one kind of harmonic potential.

$$V_{id}(\xi_{ijkl}) = k_{\xi}(\xi_{ijkl}-\xi_o)^2, \tag{13}$$

where $V_{id}(\xi_{ijkl})$ is the improper dihedral potential, $k_{\xi}$ is the dihedral force constant, $\xi_{ijkl}$ is the bond angle between i-j-k-l and $\xi_o$ is the equilibirium bond angle between i-j-k-l.

Fig. 3.6 below shows the potential generated if there is a torsion built up in the system at equilibirium. All the interactions which are 4 bonds away are generally neglected in molecular dynamics simulations. This completes the basic introduction to the potentials generated by the non-bonded interactions and the bonded interactions.

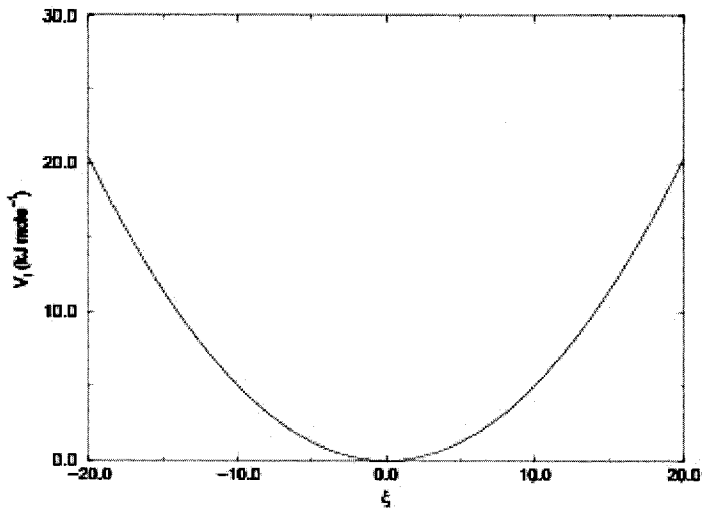


Fig. 3.6. Improper dihedral potential (75).

### 3.4.3 Special Interactions

Special potentials are used to impose restraints on the motion of the system to avoid disastrous deviations or to include knowledge from experimental data. In either case they are not really part of the force field and the reliability of the parameters is not important. Position restraints is one such kind which is very important in this class of potentials.

#### 3.4.3.1 Position Restraints

These are used to restrain particles to fixed reference positions. They can be used during equilibration in order to avoid too drastic rearrangements of critical parts (i.e., to restrain motion in a protein that is subjected to large solvent forces when the solvent is not yet equilibrated).

The following potential function is used for this kind of interactions:

$$V_{pr}(r_i) = 0.5k_{pr}|r_i - R_i|^2, \quad (14)$$

Where $V_{pr}(r_i)$ is the potential generated by position restraints, $k_{pr}$ is the position restraint force constant, $r_i$ is the position of atom i, distance and $R_i$ is the reference or equilibirium position of atom i.

This potential can be re-written as

$$V_{pr}(r_i) = 0.5\ [\ k^x_{pr}|x_i - X_i|^2\ \mathbf{x} + k^y_{pr}|y_i - Y_i|^2\ \mathbf{y} + k^z_{pr}|z_i - Z_i|^2\ \mathbf{z}\ ], \quad (15)$$

Where $x_i, y_i, z_i, X_i, Y_i,$ and $Z_i$ are the x-, y- and z- coordinates of $r_i$ and Ri respectively.

Hence the forces ($F_i^x\ F_i^y\ F_i^z$) derived are :

$$F_i^x = -k^x_{pr}\ (\ x_i - X_i\ ), \quad (16)$$

$$F_i^y = -k^y_{pr}\ (\ y_i - Y_i\ ) \quad (17)$$

$$F_i^z = -k^z_{pr}\ (\ z_i - Z_i\ ) \quad (18)$$

Three different force constants can be used to restrain the spatial positions of the atoms in a plane or in a line. The restraints are applied using a special fixed list of atoms.

Most of the important concepts dealt in molecular dynamics simulations have been explained in the above sections. Before doing simulations, a list of all atoms or combinations of atoms on which various contributions of potential functions will act should also be known. These are generally described in topology file.

### 3.4.4 Periodic Boundary Conditions

The classical way to minimize edge effects in any finite system is the application of periodic boundary conditions. In other words, the system to be simulated is surrounded with translated copies of itself. Hence there are no boundaries of the system, the artifact caused by unwanted boundaries is now replaced by artifact of periodic conditions.

### 3.4.5 Group Concept

One can use groups of atoms to perform certain actions. There can be different groups i.e., Temperature-coupling group, freeze group, accelerate group, energy monitor group, center of mass group. For example, in a solvated macromolecule the solvent can be coupled with a shorter time constant to a bath than is a macromolecule, or a surface can be kept cooler than an adsorbing molecule. This can be done using temperature coupling group.

## 3.5 Simulation details

Before a simulation is started, the co-ordinates of all the atoms in the system should be assigned. This in general can be obtained from protein data bank or from experimental data. The velocities can either be set to zero at the start of the simulation or assigned random numbers generated from the maxwellian distribution at a particular temperature as shown below

$$p(v_i) = \text{sqrt}\left( m_i / 2\pi kT \right) \exp\left( -m_i v_i^2 / 2kT \right), \qquad (19)$$

where k is Boltzmann's constant, $m_i$ mass of $i^{th}$ atom, $v_i$ velocity of $i^{th}$ atom, T temperature of the simulation and $v_i$ velocity of atom i.

## 3.6 Canonical Ensembles

There are different ways in a simulation to treat macroscopic boundary conditions. The temperature T and number of particles N are most of the times a constant. But there are several options for the volume or pressure, the pressure again have options to describe in lateral and perpendicular directions. In the simulations considered in this dissertation report, the ensemble type used is NPT (Constant N, Constant P and Constant T), which is generally regarded as the best approach.

## 3.7 Electrostatic interactions and cutoffs

According to eqn. (2), it is assumed that the interactions of all the atoms is considered, but this is not true, as it is computationally very expensive. Since the interactions become weaker at longer distances, it is reasonable to apply cut-off at some point i.e., no longer calculate the interactions between atoms which are more than a certain value. If cut-off's are applied, it means some of the interactions are neglected and how serious this can be depends on the type of interactions and the magnitude of the cutoff radius used. By performing test simulations and using the data from literature, reasonable values of cut-off can be considered. Van der waals interactions rapidly decrease with increasing distance. On the other hand, coulomb interactions between dipoles are quiet long-ranged. A popular method is to use a spherical double-cutoff, which means that all the interactions within a cut-off is calculated every step while all the interactions of the system is calculated once every N steps. Generally N is taken to be between 10 and 20.

## 3.8 Temperature and Pressure coupling

There can be drift during equilibration, drift as a result of force truncation (to speed up computations) or heating due to external or frictional forces. So, it is a necessity to control the temperature of the system in the simulations. There are two types of

temperature coupling schemes. One is weak coupling scheme of Berendsen and the other is Nose-Hoover scheme. In all the simulations reported in this work, a weak coupling scheme of Berendsen is used which is discussed next.

### 3.8.1 Berendsen Temperature Coupling

The Berendsen algorithm (76) is weak coupling with first-order kinetics to an external heat bath with given temperature $T_o$. If there is any deviation of the system temperature from the reference temperature, the algorithm brings back the system temperature T to the reference temperature $T_o$ according to eqn. (20)

$$dT / dt = ( T_o - T ) / \tau , \tag{20}$$

where $\tau$ is the berendsen temperature coupling time constant.

In other words the temperature of the system decays exponentially with a time constant $\tau$. This method seems to have an advantage to vary the strength of the coupling to suit the requirements. For equilibration purposes, the coupling time is generally short (10fs), while for equilibrium runs it is a bit longer (500fs).

Just like temperature coupling, there is pressure coupling scheme to mimic experiments. This is explained in detail in the next section.

### 3.8.2 Berendsen Pressure Coupling

The Berendsen algorithm rescales the coordinates and box vectors every step with a matrix $\mu$. This has the effect of first-order kinetic relaxation of the pressure P towards a given reference pressure $P_o$.

$$dP / dt = ( P_o - P ) / \tau_p , \tag{21}$$

where $\tau_p$ is the berendsen pressure coupling time constant.

The scaling matrix $\mu$ is given by

$$\mu_{ij} = \delta_{ij} - (\text{delta t} / 3\ \tau_p)\ \beta_{ij}\ \{ P_o ij - P_{ij}(t) \}, \quad (22)$$

where $\beta$ is the isothermal compressibility of the system. $\beta$ is 4.6 e-5 bar $^{-1}$ for water at 1 atm and 300K. Generally most solvents have similar values. Next, we look at the two most commonly used constraint algorithms SHAKE and LINear Constraint Solver (LINCS) .

## 3.9 Bond Constraints Algorithms

In classical molecular simulation techniques like molecular dynamics, the time step in the simulation is limited by bond oscillations, which have very high frequency and low amplitude. By replacing these bond oscillations with constraints, the time step can be increased by a factor of 4 and hence can speed up the simulations. LINCS and SHAKE are two algorithms which that solves this non-linear problem of resetting coupled constraints after an unconstrained update.

### 3.9.1 SHAKE and LINCS

The **SHAKE** algorithm (77) changes a set of unconstrained coordinates r' to a set of coordinates r" that fulfill a list of distance constraints, using a set r as reference:

$$\text{SHAKE}(r' \rightarrow r";r) , \quad (23)$$

This is consistent in solving a set of Lagrange multipliers in the constrained equations of motion. Detailed explanation of this scheme can be found elsewhere (77). This is an iterative procedure and continues until all constraints are satisfied within a relative

tolerance. It is also the first algorithm developed to satisfy bond geometry constraints during molecular dynamics simulations. Later on, a noniterative form of SHAKE was developed by (78).

**LINCS** (79), on the other hand is non-iterative and always uses two steps. This method is more stable and faster than SHAKE, but it can only be used with bond constraints and isolated angle constraints, such as the proton angle in hydroxyl bond. In the work reported here, Lincs algorithm was used to contrain bond lengths. The detailed explanation of this scheme can be found elsewhere (79). From eqn. (2), it is clear that F is 3N force vector and m is a 3N X 3N diagonal matrix, containing the masses of N particles. This system is constrained by K time-dependent constraing equations as shown:

$$g_i(r) = |r_{i1}-r_{i2}| - d_i = 0;\ i = 1,2,\ldots..,K, \qquad (24)$$

where $r_{i1}-r_{i2}$ is the bond-length and $d_i$ is the constraining distance.

This algorithm works in two steps as shown in Fig. 3.7. In the first step the projections of the new bonds on the old bonds are set to zero. In the second step a correction is applied for the lengthening of the bonds due to rotation.

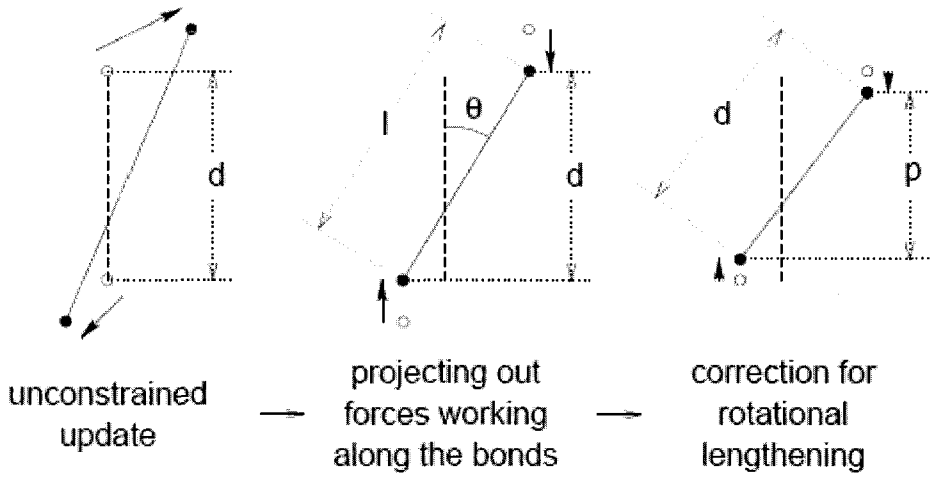


Fig. 3.7. Principle behind LINCS algorithm.

## 3.10 Set-up of Simulations

The above sections outline some of the important techniques/parameters used in molecular dynamics simulations. For a detailed explanation on these parameters in molecular dynamics simulations, the reader is directed to read van der Spoel et. al. (75, 80).

The general procedure before starting any simulation is to check whether the system is having minimum energy (local minima). Otherwise large norms of forces will be built eventually halting the simulation. Once the system attains the local minima, then molecular dynamics simulation can be started. The next few section covers the topics of energy minimization, setting up the system for molecular dynamics simulation and finally the data analysis done on the trajectories obtained from molecular dynamics simulation. Details on the molecular dynamics simulation package used in this dissertation work is also provided.

### 3.10.1 Energy Minimization

Function optimization is regarded as one of the important concepts in much of the numerical analysis. In the context of macromolecules, the function to be optimized or minimized is the energy. The energy landscape of a biomolecule possesses an enormous number of minima or conformations. The goal of the energy minimization is to find the local minima (not necessarily the global minima).

Energy minimization is generally done using steepest descent, conjugate gradients or L-BFGS algorithms. In most of the simulations reported here in this work, steepest descent and conjugate gradient algorithms are used. Each one has its own advantages and disadvantages. While steepest descent is not the most efficient algorithm for

searching, it is robust and easy to implement. On the other hand, Conjugate gradient is slower than steepest descent in the early stages of minimization, but becomes much more efficient closer to the energy minimum. Most of the parameters used for the steepest descent and the conjugate gradient algorithm are similar.

### 3.10.2 Molecular Dynamics

As earlier described, the main of MD is to update the position and velocity at each and every time step, given the initial coordinates of all the atoms in the system along with the velocity (or temperature). To update the coordinates and velocities, the leap-frog (81) algorithm is used. This algorithm uses positions **r** at time t and velocities $v$ at time (t-$\delta$t/2); it updates positions and velocities using the forces F(t) determined by the positions at time t:

$$v(t+\delta t/2) = v(t-\delta t/2) + F(t)\,\delta t\,/m, \tag{25}$$

$$r(t+\delta t) = v(t+\delta t/2)\,\delta t + r(t), \tag{26}$$

This method is superior to continuum approaches, and the advantages include:

1. Inclusion of the collective, many-body interaction potentials at the nanoscale level,
2. Dynamical screening,
3. Avoidance of the "mean-field" approximations,
4. A natural inclusion of noise and statistical fluctuations,
5. Self-consistent and dynamical transport calculations without arbitrary fitting parameters, and
6. Easy incorporation of arbitrary defects and non-uniformities.

## 3.11 Limitations of the MD Scheme

The Molecular Dynamics simulation approach has a number of important limitations. The potential function described earlier requires a large number of parameters for partial charges, van der Waals interactions, equilibrium values for bonds, angles and dihedrals, and force constants. Most of these can be obtained from experiments or quantum mechanics, but there is no guarantee that these parameters give good results. One of the other limitations is the maximum time step that can be used in MD simulations. A typical value used is 2 femto seconds, even with the bond constraints algorithms like LINCS or SHAKE. This limits the length of the current simulations to few nanoseconds and utmost a microsecond with good computational resources. Of course, this also depends on the size of the system. Thus, computational complexity and the requirement of large memory and an array of fast computers can become a impeding requirement. One of the other limitations of standard molecular dynamics is the classical treatment of the system, which is of no consequence in this dissertation report as the simulations are primarily based on lipid systems.

## 3.12 GROMACS – Groningen Machine for Chemical Simulations

The molecular dynamics simulation package used for the work reported in this dissertation report is GROMACS. GROMACS stands for Groningen Machine for Chemical Simulations. It was originally developed in the university of Groningen, but now it is maintained at several places. This package is used to simulate the Newtonian equations of motion for systems with hundreds to millions of particles. Recently, they implemented Quantum Mechanics version along with the more general classical mechanics.

One of the important applications when building this package is to look into biochemical reactions of macromolecules like proteins and lipids. The central goal for

any molecular dynamics simulation package is the calculation of non-bonded interactions, as it is computationally expensive. But GROMACS is regarded as extremely fast in calculating non-bonded interactions and hence many groups across the world use it for bio-molecules as well as non-biological molecules like polymers etc.

### 3.12.1 Advantages of GROMACS

1. GROMACS has a nice option to keep posted on when the simulation is expected to finish and how far has it come.
2. It can write coordinates using lossy compression, which provides a very compact way of storing trajectory data. For the longer simulation runs, sometimes more than 10GB is required just to store the coordinates. If it were not for this lossy compression technique, much of the space will be used unnecessarily to store the data.
3. One of the important features of GROMACS is that it can be run in parallel, using standard MPI communication. This will definitely boost up the time required for the simulations, since the computational power is increasing day-by-day.
4. Last but not least, GROMACS is Free Software available under GNU General Public License.

### 3.12.2 GROMACS Preprocessor

To give an idea about the GROMACS preprocessor, a brief explanation on the input files needed for the simulation and the output files extracted from this molecular dynamics simulation is given below as shown in Fig. 3.8.

xxx.gro → Input file with atomic co-ordinates (and/or velocities) of all particles in the system

xxx.mdp → molecular dynamics parameter file, which essentially contains all the simulation conditions and external forces, if any.

xxx.ndx → basically an index file, which in most of the cases is used after the simulation is finished to do data analysis.

xxx.top → most essential file of all the files. It has all the parameters regarding the structure of the system i.e., bond lengths, bond angles, charges, lennard-jones parameters etc.

grompp shown in Fig. 3.8 basically reads a molecular topology file, checks the validity of the file and expands the topology from a molecular description to an atomic description.

mdrun is the subroutine used in Gromacs package to start the simulation. xxx.mdp file has the option to identify whether the simulation is for energy minimization or the normal molecular dynamics simulation.

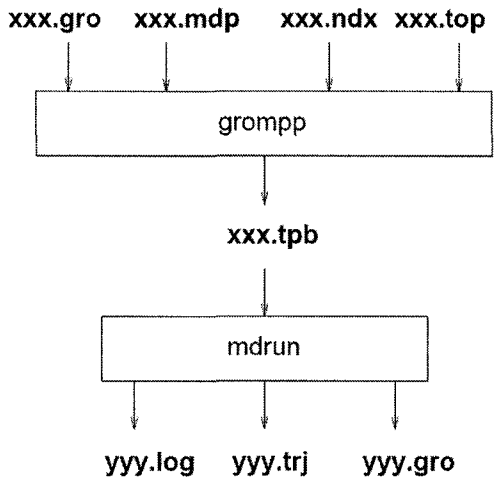


Fig. 3.8. GROMACS preprocessor: Flow Chart (75).

All the coordinates, velocities and energies are stored in the files yyy.log, yyy.trj and yyy.gro, which can be used with other Gromacs sub-routines to determine variables of interest.

## 3.13 Data Analysis

This section is devoted to explain some of the data analysis techniques used in the present dissertation work. Most of the data analysis is done on the trajectory of the simulation obtained. Gromacs has many subroutines of interest for biochemists. Since most of the dissertation work reported here needs other variables of interest as well, few subroutines were written using VMD's Tcl scripting language and MATLAB.

Some of the important variables of interest for structural biologists are the radial distribution function, root mean square deviation and radius of gyration. These are generally used to confirm the structure's stability and is explained in detail in next section. Apart from these, a brief review of autocorrelation functions and Green-kubo relations are provided. There in general are used to calculate transport coefficients like diffusion and mobility.

### 3.13.1 Radial Distribution Function

The radial distribution function describes how the atoms in a system are radially packed around each other. This is very effective in describing the average structure of disordered molecular systems like liquids. Since the motion in liquids is always disordered, the idea about the average structure is very important and radial distribution function gives an idea about this.

One of the ways, people involved in computer simulation of biomolecular systems confirm their atomic structure is by comparing the experimental results with their simulations. The radial distribution function $g_{AB}(r)$ can be calculated experimentally by X-ray or neutron diffraction studies and can also be calculated with simulations using the formula:

$$g_{AB}(r)=<\rho_B(r)>/<\rho_B>_{local}=1/<\rho_B>_{local} 1/N_A \sum\sum\delta(r_{ij}-r)/4\pi r^2, \quad (27)$$

where $<\rho_B(r)>$ is the particle density of type B at a distance r around particles A, and $<\rho_B>_{local}$ is the particle density of type B averaged over all spheres around particles A. Fig. 3.9. shows the radial distribution function between two oxygen atoms of different water molecules.

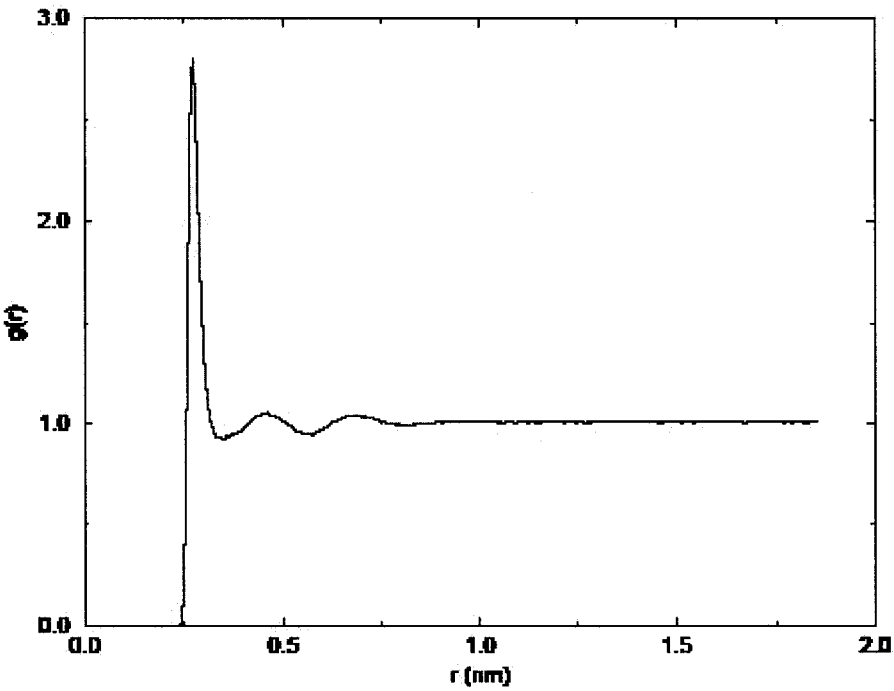


Fig. 3.9. Radial distribution function of *ow – ow*.

### 3.13.2 Radius of Gyration

The radius of gyration describes the distribution of particles (or infinitesimal elements) in a D-dimensional space by relating it to an equivalent distribution in a D-dimensional sphere, usually a circular (D=2) or spherical (D=3) distribution. The radius of gyration is a useful estimate of the size of a molecule or is used in biomolecular

simulations to have an idea about the compactness of the structure of the macromolecule considered.

The radius of gyration $R_g$ is generally calculated by the formula:

$$R_g = (\sum_i ||r_i||^2 m_i / \sum_i m_i)^{1/2}, \quad (28)$$

Where $m_i$ is the mass of atom i and $r_i$ the position of atom i with respect to the center of mass of the molecule. It is especially useful to characterize polymer solutions and proteins.

### 3.13.3 Root Mean Square Deviation

As the name suggests, root mean square deviation (RMSD) is the deviation calculated from the reference structure. RMSD is given by the formula:

$$RMSD(t_1,t_2) = [1/M \sum m_i ||r_i(t_1) - r_i(t_2)||^2]^{1/2}, \quad (29)$$

where mi is the mass of the particle I, M is the total mass of the system, $r_i(t)$ is the position of the atom i at time t.

### 3.13.4 Green-Kubo Relations

One of the interesting things in this dissertation report is the calculation of diffusion coefficient as a function of space and electric field. This can be done either by using autocorrelation functions or by using mean square displacement.

Transport coefficients like the diffusion coefficient D, the viscosity coefficient $\eta$ can be expressed as time integrals of appropriate time correlation functions. This

formulation is known as Green-Kubo formulae, which is the direct result of linear response theory in statistical mechanics. The theory of correlations is well established (82).

To give a brief idea about this, we describe the implementation of the correlation functions. The autocorrelation function is basically the cross-correlation of the function. Hence it is given by the formula:

$$C_f(t) = \langle f(t+dt)f(t)\rangle_{dt}\,, \tag{30}$$

where $C_f(t)$ is the auto-correlation function of the parameter f(t).

If the parameter considered is the velocity of the particle, the diffusion coefficient (D) is calculated by the formula:

$$D = K \int C_v(t)dt, \tag{31}$$

where K is the appropriate scaling factor, $C_v$ is the autocorrelation function of velocity.

### 3.13.5 Mean Square Displacement

As the name implies, mean square displacement is the deviation of the particle from time t=0. Diffusion coefficient (D) of the solvent / macromolecule in biomolecular simulations can be calculated using the Einstein relation

$$D = 1/(2Nt)\ \text{lt}\ t\rightarrow\infty \langle ||r_i(t) - r_i(0)||_2\rangle, \tag{32}$$

where N is the number of degrees of freedom, t is the time considered for calculating the diffusion coefficient, and $r_i(t)$ is the coordinates of the particle i at time t. If the particle of interest is inside a nanopore, then N can be considered as 1 and only the diffusion along the axis of the pore is considered. Similarly if the particle is near the interface of 2

different macromolecules e.g., water-bilayer interface, then N is considered as 2 and the diffusion along that plane can be calculated. If the diffusion is in bulk, then N has to be considered as being equal to 3.

### 3.14 VMD – Visual Molecular Dynamics

Visual MolecularDynamics (VMD) is a molecular graphics program (83) designed for the interactive visualization and analysis of biopolymers such as membranes, lipids, nucleic acids and proteins. This can also be used along with Tcl scripting to get the required data analysis done with the trajectories obtained from the molecular dynamics simulations. All the figures provided on the structures of the biopolymers is from VMD render image. GROMACS together with VMD provides a very good tool for data analysis with the trajectory.

### 3.15 Mathematical Model for Electric Field Induced Calcium Release

Even though the major portion of the work covered in this dissertation report includes molecular dynamics simulations, other continuum approaches like reaction-diffusion mechanisms are also used to simulate the effects of nsPEF's on cell. An important goal of this contribution is to obtain a quantitative dynamical analysis of the electrically stimulated calcium release from the endoplasmic reticulum (ER) stores by an externally applied nanosecond voltage pulse. Such calcium release plays an important role in several cellular events (84) and initiate factors in the apoptotic pathway (85). The primary mechanism and its quantification for electrically driven calcium release has not been probed, though electroporation of the ER membrane is conjectured to be a likely pathway.

### 3.15.1 Modeling Details

Before discussing our Calcium model for dynamical concentration changes in both the cytosol and the ER, it is perhaps useful to briefly review the calcium signaling and release mechanisms. Intracellular $Ca^{2+}$ dynamics has the unique feature of facilitating the generation of global events (often of a periodic nature) from local, thermally-activated stochastic opening/closing of channels on the ER membrane (84-85). Such channels are typically closely packed into clusters, called focal sites (86, 87) with a random spatial distribution and an average spacing in the 2–6 μm range. A typical channel present in the ER of many cells that facilitates calcium movement, is the inositol 1,4,5-triphosphate receptor (IP3R) channel. Ryanodine receptors (RyR) though present, are more important in muscle cells (88). The IP3R channel has an activating binding site for the messenger molecule IP3 (m-gate), an activating site for $Ca^{2+}$ (n-gate), and an inhibiting $Ca^{2+}$ binding site (h-gate). Experimental findings suggest that the channel is open if both $Ca^{2+}$ and IP3 are bound to the activating sites, and at the same time $Ca^{2+}$ is not bound to the inhibiting site. Binding of $Ca^{2+}$ to the inhibiting site of one of these subunits, closes the channel.

This "open channel" probability increases nonlinearly with the IP3 and calcium concentrations. Hence, any $Ca^{2+}$ released by one channel increases the open probability of neighboring channels. This provides a self-amplifying, positive-feedback non-linear mechanism (89) referred to as "calcium-induced calcium release (CICR)". Very high $Ca^{2+}$ concentrations inhibit the channels. The $Ca^{2+}$ SERCA pumps remove $Ca^{2+}$ from the intracellular space. This is necessary since elevated concentrations of $Ca^{2+}$ are toxic for the cell.

Initial simulation efforts to quantify the intracellular $Ca^{2+}$ dynamics primarily focused on deterministic continuum models (90). These reaction-diffusion models were able to explain the observed wave patterns, oscillatory, or bistable phenomena.

Extensions to these models that allowed the channels to act as discrete $Ca^{2+}$ sources facilitated the transition from localized to traveling structures (91). The stochastic behavior seen in spark and puff formation and the rather small number of channels creating a localized event, motivated the introduction of stochastic models (92). Mesoscopic aspects of the calcium-release phenomena were probed by Shaui and Jung (93). They found that site clustering could effectively allow for collectively enhanced, coherent calcium responses to signals. Homogeneously distributed channels, on the other hand, would not be capable of producing the same large response.

Discrete models have successfully predicted oscillatory dynamical regimes and random, collective calcium enhancements. *However, such localized, discrete stochastic models are perhaps not necessary in the present context of field-assisted calcium release for a variety of reasons.* First, it has become apparent based on improved spatial imaging (94) that the overall calcium release varies in a continuous fashion despite the stochastic variations in the numbers of individual channels recruited for release and the durations of their openings. Thus, macroscopically, a continuum model remains relevant. Furthermore, the present focus is on very high (> 15 kV/cm) electric fields. This external stimulus produces very strong electrostatic driving forces and gives rise to highly non-equilibrium conditions. Hence, it can safely be assumed that all of the channels are effectively driven into the calcium release (or "open") state by the strong external electric signal. Statistical variability can be expected to be minimal, and that all of the discrete sites would be collectively forced past the calcium-release threshold.

### 3.15.2 Analysis of Calcium Model

Calcium release from the ER predominantly occurs through IP3R sites (95). The model used here utilizes the Li-Rinzel two-variable simplification (96) of the De Young–Keizer model (97) with appropriate modifications to account for electric field effects. The basic model has been used in the past (but without any external electric stimulation)

for various analyses (98). According to this model, calcium flux between the ER and the intracellular space is driven by the three following processes: (i) $Ca^{2+}$ outflow mediated by the IP3 channel, (ii) a small diffusion-driven $Ca^{2+}$ leakage from the ER into the cytosol, and (iii) the SERCA ATPase pumps that drive $Ca^{2+}$ back into the ER to maintain the resting (basal) calcium levels.

Here we include the additional mechanism of electric field driven $Ca^{2+}$ outflow from the ER to the cytosol. Electroporation of the ER membrane, coupled with the electrical driving force on the calcium cations contributes to this outflow. In a sense, the ER becomes more "leaky." This effect has been included in our one-dimensional, time-dependent reaction–diffusion model through a time-dependent leak-flux term. The equations for $Ca^{2+}(z,t)$ density changes in the cytosol and ER are expressed, in general, by the continuity equation as:

$$\partial[Ca^{2+}]/\partial t = - \partial F(z,t)/\partial z + G(z,t) - R(z,t) , \qquad (33)$$

where F(z,t) is the passive calcium flux at any location "z" and time "t," while G(z,t) and R(z,t) are possible $[Ca^{2+}]$ generation and recombination/attachment rates that could include pumps, channels and pores. In our treatment, generation, recombination/attachment of $Ca^{+2}$ ions, action of pumps, channels, pores etc.. has been ignored except at the ER-cytosol boundary. The passive flow of $[Ca^{2+}]$ ions can be expressed in terms of drift and diffusive processes. Assuming that the drift velocity of the $[Ca^{2+}]$ ions in response to the highest local electric fields is much smaller than their thermal velocities, and that the role of scattering can be approximated by a relaxation time "$\tau$", the flux F(z,t) can be cast into the following "drift-diffusion" form:

$$F(z,t) = [Ca^{2+}] \mu E(z,t) - D(z,t) (\partial[Ca^{2+}]/\partial z) , \qquad (34)$$

where $\mu$ is the ion mobility, and D the diffusion coefficient. These parameters are simply related to the relaxation time "$\tau$" as : $\mu = q \langle v^2 \tau \rangle / (3 k_B T)$ , and $D = (k_B T/q) \mu$ ,

where q is the elementary charge, T the temperature, $k_B$ the Boltzmann constant, v is the individual ionic velocity, while <> denotes an ensemble average over $Ca^{2+}$ ions.

For completeness, it may be pointed out that there are some approximations inherent in our use of the above drift-diffusion scheme. For example, the diffusion coefficient and mobility are taken as fixed, invariant parameters. Strictly, this can only be done if the system is stationary, not far from equilibrium, and strong local inhomogeneities do not exist. For non-stationary, non-Markovian processes, the diffusion coefficient needs to be evaluated as an integral over a two-time velocity autocorrelation function (82). Due to the ultra-short electric pulse, we assumed near stationarity. Treatments of time-variations of transport parameters in an aqueous medium over time scales of nanoseconds or shorter, and in the presence of external electric fields, have been reported by our group elsewhere . Also, since the $[Ca^{2+}]$ release and other bio-chemical changes are relatively perturbative in nature with almost no impact or deviations in internal scattering rates, the $\mu$ and D transport parameters can essentially be assumed homogeneous. Thus, using eqn. (34) in eqn. (33) yields:

$$\partial[Ca^{2+}]/\partial t = D(z,t)\,(\partial^2[Ca^{2+}]/\partial z^2) - \mu\,\partial\{[Ca^{2+}]\,E(z,t)\}/\partial z + G(z,t) - R(z,t)\,. \qquad (35)$$

Since an analytical solution cannot be obtained for the above equation, a numerical approach was used based on a uniform discretization in space (spacing "dz") and time (interval "dt"). The details of the simulation along with the results obtained are given in detail in Chapter IV.

# CHAPTER IV

# SIMULATION RESULTS AND DISCUSSION

## 4.1 Introduction

This chapter is devoted to the results of simulations on lipid membranes, micelles, proteins, DNA, water and intracellular calcium release. A general molecular dynamics parameter list, which is common to all the molecular dynamics simulations, is given in Section 4.2. Section 4.3 is devoted to MD simulations to show the electroporation of an "all-atom" pure DPPC bilayer. In Section 4.4, simulations showing phosphatidyl-serine (PS) externalization through the MD technique are presented. Evaluations of transport parameters such as the non-equilibrium diffusion coefficients, field dependent permittivity etc.. for cells subjected to intense electroporative voltages using MD simulations are carried out in Section 4.5. Next, simulations showing membrane fragmentation during the application of pulsed electric fields are given in Section 4.6. The next section 4.7 shows the possible cytochrome C release upon the application of nsPEF's, while simulations showing electric field induced DNA damage are given in Section 4.8. All the above simulations are based on MD technique. Finally, Section 4.9 is devoted to some numerical modeling results of calcium dynamics through the endoplasmic reticulum (ER). This simulation of intracellular calcium release is based on continuum approaches, primarily, the reaction-diffusion mechanism.

## 4.2 Molecular Dynamics Simulation Parameters

Except simulations on the intracellular calcium release, all the other simulations in this dissertation report utilize MD scheme. So, a brief overview of the molecular dynamics parameters used in the MD simulations is briefly presented at the very beginning. In early work on lipid bilayers, Venable *et al.* (15) and Egberts *et al. (14)*

applied MD technique to dipalmitoyl-phosphatidylcholine (DPPC) bilayers. Various other studies of lipid bilayer systems have since been reported (99, 100). As earlier mentioned, MD simulations rely on the application of classical Newtonian mechanics for the dynamical movement of ions and neutral atoms, taking account of the many-body interactions within a realistic molecular representation of the bio-system. Thus, for example, a segment of the lipid bilayer membrane or a channel protein is first constructed taking account of the initial geometric arrangement of all the atoms and their bonding angles. Regions of water containing user-specified ion densities are then defined on either side of the membrane to form the total simulation space. In water-lipid system, simple point charge (SPC) is preferred as the water model because it has a better chemical potential in mixed systems.

For any simulation set-up, initial velocities, temperature and pressure are set for all particles. In order to prevent the system energies from increasing with time due to the dynamic acceleration, velocities are typically rescaled periodically by coupling the system to a constant temperature bath (76). In our study, the GROMACS (Groningen Machine for Chemical Simulations) package in NpT ensemble was used for the MD simulations of field-induced membrane effects. Visualization of the results was achieved through the Visual Molecular Dynamics (VMD) tool (83). For uniform bilayer systems, dipalmitoyl-phosphatidyl-choline (DPPC) membrane was chosen. Similarly to study heterogeneous membranes, PS molecules are embedded in the dipalmitoyl-phosphatidyl-choline (DPPC) membrane. The force fields for membrane molecular motion are taken from the literature (76, 77, 79). The system was coupled using a semi-isotropic Berendsen pressure coupling of 1 atmosphere with compressibility of $4x10^{-5}$ along the $z$ direction, and zero along the $x$ and $y$ directions. A 323 K heat bath is chosen to retain the liquid phase of the membrane (101). The algorithms for pressure and temperature control were those discussed by Allen and Tildesly (102). The requisite time constants for pressure and temperature coupling were set to 1 ps and 0.1 ps, respectively. A 4 fs time step has typically been used with the Linear Constraint Solver (LINCS) algorithm outlined by Berendsen *et al.* (79) to constrain all the bond lengths within the lipids and

on the water geometry. A group based twin cutoff scheme was employed for the non-bonded interactions, with cutoff radii of 1.0/1.4 nm for Lennard-Jones interactions. The particle-mesh Ewald (PME) scheme was applied in our MD simulations taking account of the long-range electrostatic interactions. Periodic boundaries were applied, and the simulations carried out under constant pressure conditions. This method allows the simulation box size to change so that the internal virial value matches the external pressure. These are the general reference parameters for all the molecular dynamics simulations in the dissertation work presented here. If the molecular dynamics parameters change from the reference values, they are explicitly mentioned, otherwise the parameters used are same as above.

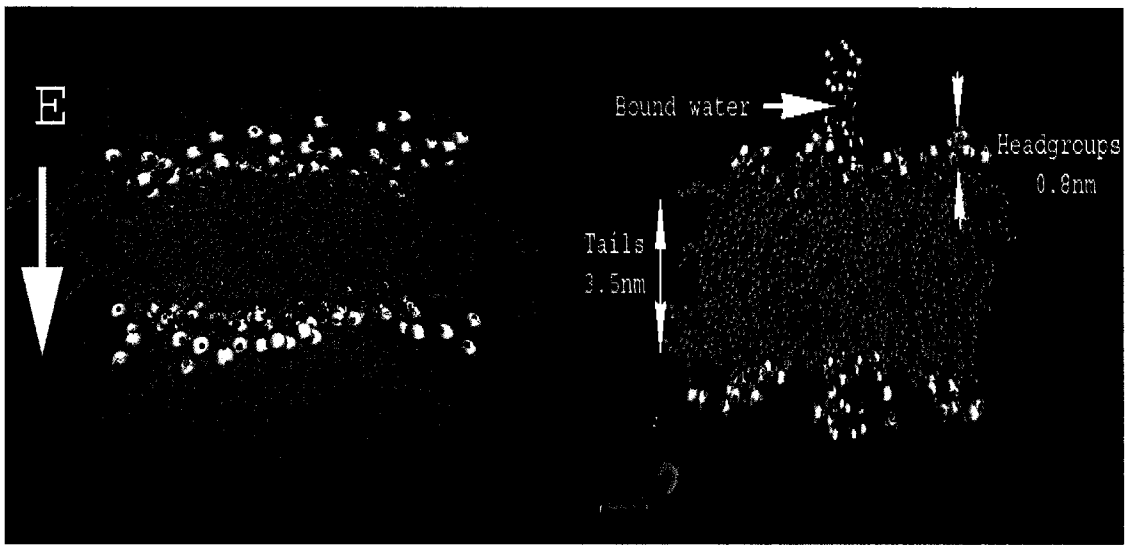


Fig. 4.1. DPPC bilayer structure (left) with SPC water above and below, 2-D cross-section (right) showing the thickness of head-groups and fatty acids.

All MD simulations (pure DPPC, DPPC–DPPS combination, DNA, proteins etc.) were carried out in two stages. In the first phase, the MD calculations were carried out for an initial membrane (or DNA/protein) patch surrounded by the water molecules in the absence of any external electric field or surface tension. In this process, the system was

allowed to stabilize and reach a dynamic equilibrium. This process implicitly allows for internal energy minimization and the attainment of a stable initial configuration.

## 4.3 Lipid Membrane Poration

A stable system containing 128-DPPC (dipalmitoyl phosphatidylcholine) lipids and 5476 water molecules is directly taken from previous work of Tieleman et.al. (101). This membrane along with the solvent SPC water model is shown in Fig. 4.2.

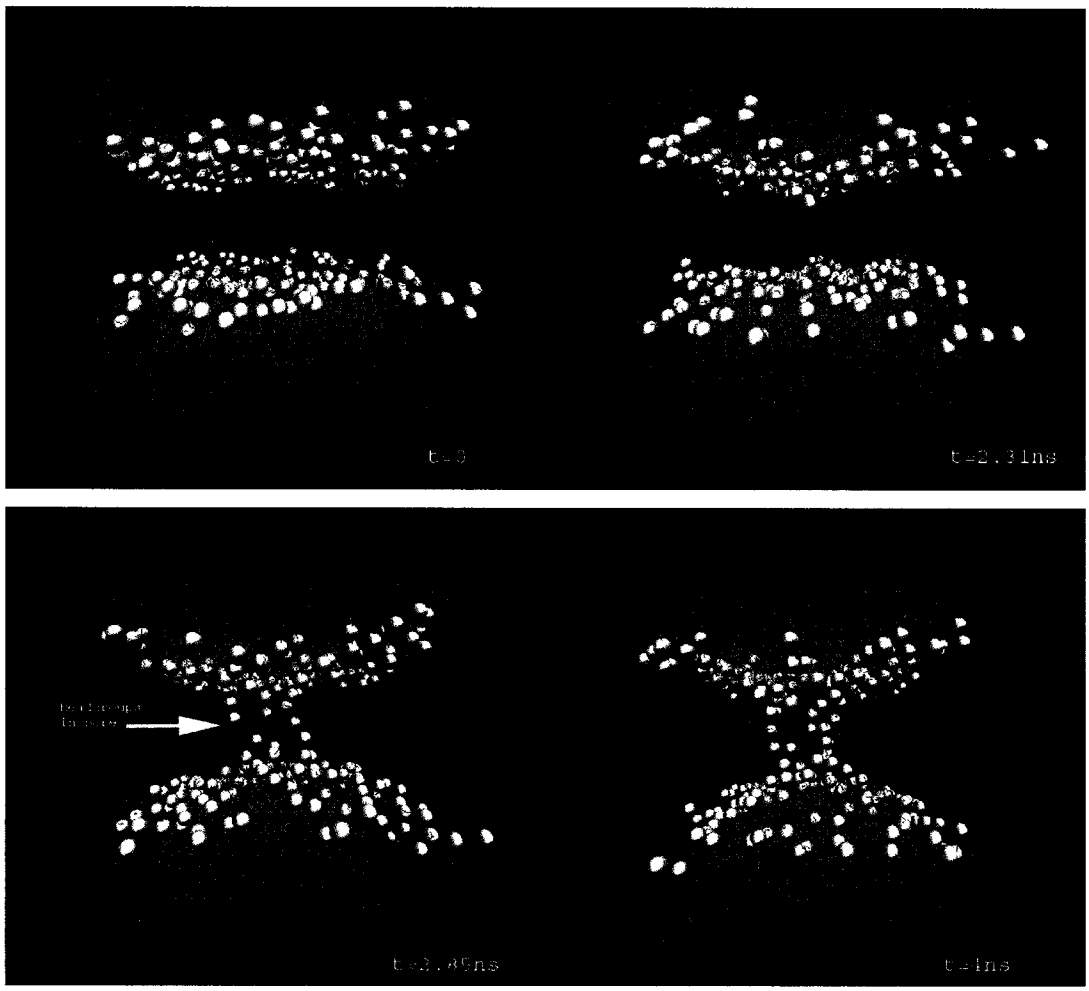


Fig. 4.2. Pore formation in DPPC bilayer.

For clarity purposes, tails are not shown in Fig. 4.2(a). A constant electric field of 0.5 V/nm was assumed. Initially, the surface tension in the membrane was $2 \times 10^{-2}$ J . The application of the electric field causes some structural rearrangements (i.e., defect formation) that begin to form at the anode side (i.e., the membrane bottom) as shown in Fig. 4.2 (b).

A pore is then seen to form fairly quickly after the creation of the initial defect. Complete nanopore formation is predicted within about a nanosecond after the initial structural change. Thus, as seen from the present simulations, most of the time for the electroporation process is taken up by the initial defect formation. A pore with headgroups slowly entering in the pore region is shown in Fig. 4.2(c), and the complete pore formation at 4ns is shown in Fig. 4.2(d). This result demonstrates a good match between the MD result of Fig. 4.2, the predictions of a continuum model (43), and the actual experimental data (10). A nanopore is predicted to form within about 5–6 ns at these high field intensities. Since the pulse duration is typically longer than this time, the ion transport (especially for ions with smaller radii) would be very likely. Second, the initial structural rearrangement and dipole reorientation are a critical step in the electroporation process. Once an initial breakthrough is achieved, the poration process proceeds relatively quickly. The surface tension used in the simulation is far less than reported to cause stress-induced rupture of membranes (103). Hence, the pore formed is a direct result of an external electrical pulse.

Finally, the poration process has a polarity dependence, and begins on the anodic side of a membrane. The related physics can easily be understood by considering the dipolar configuration within the DPPC membrane. Fig. 4.3 shows a simple schematic of the membrane lipids with their dipoles located at the head groups. For each DPPC chain, the head group contains a dipole with a positive charge on choline, and the negative charge centered on the phosphate group. Initially, with no electric field present, the

dipoles are in random thermal motion with the positive charges residing on the outermost portions of the lipid. Electrical-fieldinduced defects are initiated by the movement of the dipoles on the surface of the membrane. The defects start to form on the anode side of the

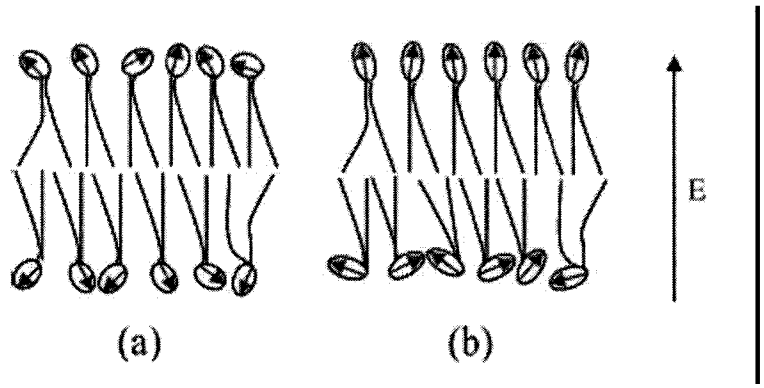


Fig. 4.3. Schematic diagram of the pore initiation process at the DPPC membrane.

membrane, because the positively charged molecules (e.g., choline) on this side are forced to swing around (i.e., reorient in the presence of a strong external electric field) and enter the membrane. However, the same applied electrical field, when acting on the dipoles located at the cathodic membrane surface, merely works to stretch the dipoles without any molecular movement into the membrane volume. Thus, Fig. 4.3(a) shows the randomly distributed dipoles at the head groups on either side of the membrane as the initial configuration. Fig. 4.3(b) shows the alignment of the dipolar head groups on the anodic side gradually deviating from the normal (equilibrium) orientation, and a defect starting to form. Thus, in accordance with the experimental observations, the pore formation is predicted to initiate at the membrane pole facing the anode.

## 4.4 PS Externalization

PS molecules are replaced with DPPC molecules on one side of the pure DPPC system to create a DPPC-DPPS mixture. If the PS externalization in the membranes is pore-driven event, then this process too, should start at the anode side. Currently, there are two competing theories regarding the PS externalization. Diffusion of the PS molecules through the membrane pores upon their formation is a one possible pathway. A second mechanism proposed in the literature, involves a PS translocation from the inner to the outer leaflet across an internal potential barrier. Here, through MD simulations, it has been shown that the energy barrier is too strong for the direct PS movement. Instead, the externalization is facilitated by the formation of the internal pores within the membranes. The

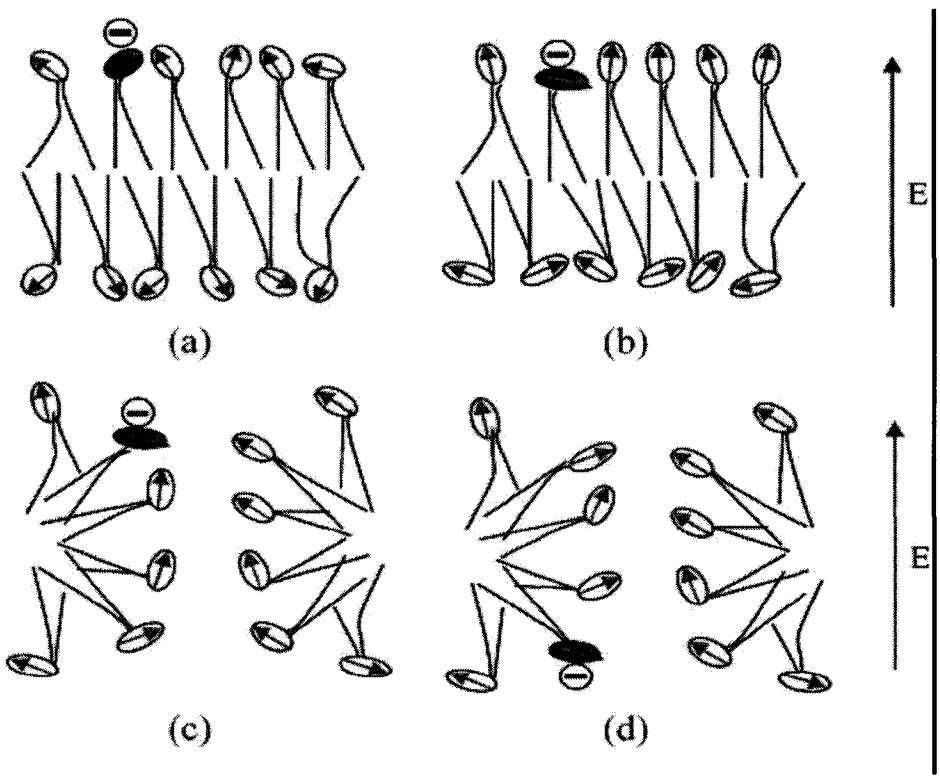


Fig. 4.4. Schematic diagram of the pore initiation process within a DPPC–DPPS membrane.

PS molecules, which are always in constant thermal motion, are then able to diffuse out through the membrane pores. Since the pore formation initiates at the anode end, the electric-field driven PS externalization also has a polarity dependence. It is dominant at the anode. Experimental observations do indicate just an anode-side preference. The electrostatics provides an additional rationale for an anode-side event. Since the PS molecules residing on the inner leaflet are negatively charged, the externally applied electric field will tend to push out the PS at the anode side, while pulling them inwards on the cathodic side. Coupling this with an anode-side pore formation event, leads to the collective effect of the preferential PS externalization at the anode end.

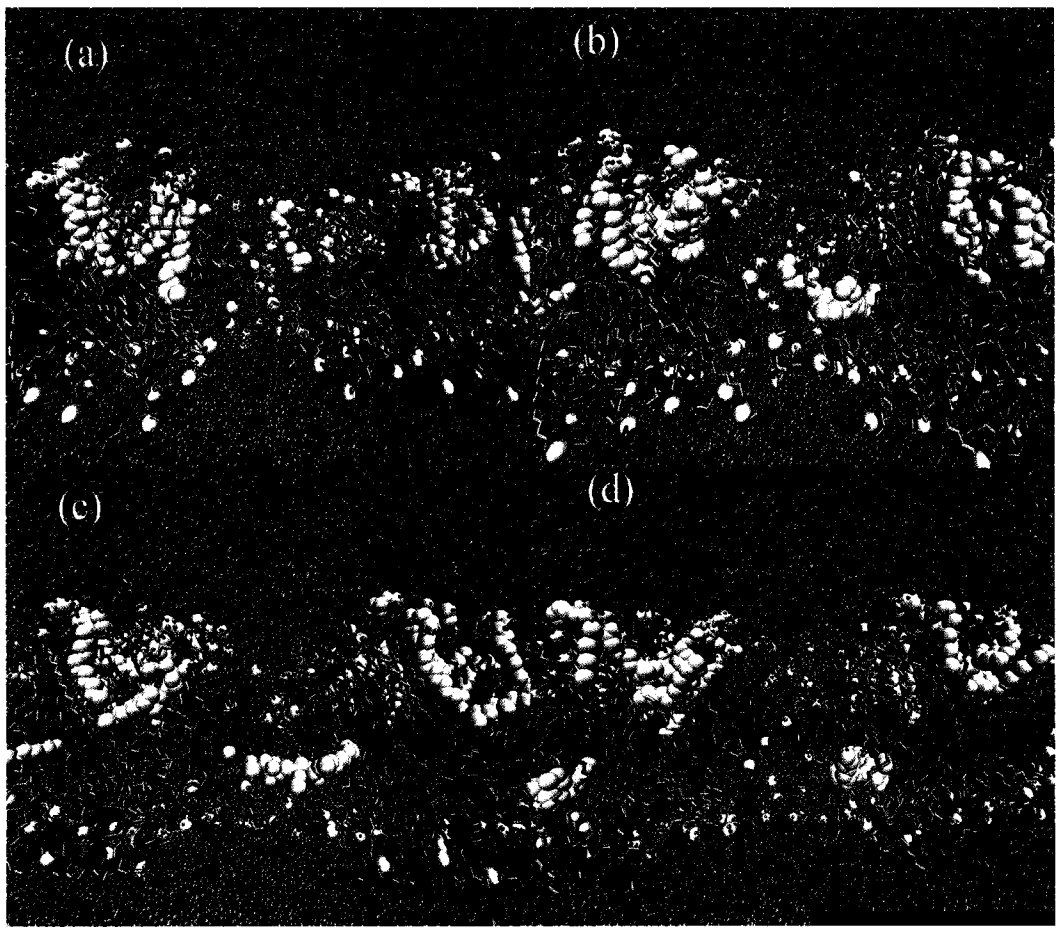


Fig. 4.5. PS externalization, a pore driven event.

Fig. 4.4 is a simple schematic diagram demonstrating the dynamics. Initially in Fig. 4.4(a), the dipoles at the DPPC lipids (shown as arrows) are randomly located, with a negative PS on the inner leaflet. With application of the electric field, the dipoles on the outer layer (anode side) reorient, leading to a defect initiation at the outer membrane surface. Eventually, a pore forms [Fig. 4.4(c)], and the negatively charged PS begins to drift and diffuses towards the exterior surface. Results of the MD simulations, shown in Fig. 4.5, demonstrate the above more clearly.

An initial snapshot of the membrane system is shown in Fig. 4.5(a), with the PS molecule located on one side of the membrane, opposite from the anode. Fig. 4.5(b) shows a pore starting to form with some translocation of the PS chain at 3.2 ns. Due to a large electrostatic force on the PS head group (in the range of $10^{-10}$ N), the chain is dragged half way to the anode side of the membrane along the wall of the nanopore at about □ 3.34 ns, as shown in Fig. 4.5(c). Finally, in Fig. 4.5(d), the DPPS chain is on the other leaflet of the membrane at 3.61 ns. The MD simulation thus validates the pore-facilitated, field-assisted mechanism of the PS externalization. An important difference between the DPPC–DPPS simulations of Fig. 4.5 and results for a pure DPPC membrane (Fig. 4.2) is the shorter time duration for the pore formation. Inclusion of a membrane defect in the form of a substitutional DPPS molecule, and the additional membrane force associated with the negative DPPS charge, collectively contribute to the quicker poration. Based on this result, one could logically extrapolate to predict that a membrane inhomogeneity (particular embedded proteins and charged ions) would further aid the electroporation and ion transport.

## 4.5 Transport Parameters

One of the important results achieved in this dissertation report is to find the frequency, space and field dependence of dielectric permittivity and diffusion coefficient in the presence of high electric fields. These would be the values under strong non-equilibrium conditions. For this, the all-atom DPPC structure that was used to show pore formation was used. The overall simulated system for MD analyses had a total of 26,893

atoms. The total simulation volume was taken to be a 6.5 nm · 6.5 nm · 8.5 nm cubic box. Fig. 4.6 shows the initial configuration of a lipid bilayer structure with a nanopore at the start of MD simulations. Details on this configuration, the pore formation process, and all preceding calculations have been reported elsewhere (43). The z-direction (perpendicular to the DPPC membrane) was divided into seven layers for spatial resolution. In the notation of Fig. 4.6, the top and the bottom-most layers (comprising mostly of water molecules) correspond to the ''above-interface'' and ''below-interface,'' respectively. The layers immediately adjacent to these are labeled as the interfacial region. Since the boundary conditions employed were periodic in nature, the top and bottom shells of water of thickness equal to the cut-off employed were ignored. In other words, the interactions between water above "above-interface" and below "below-interface" were ignored.

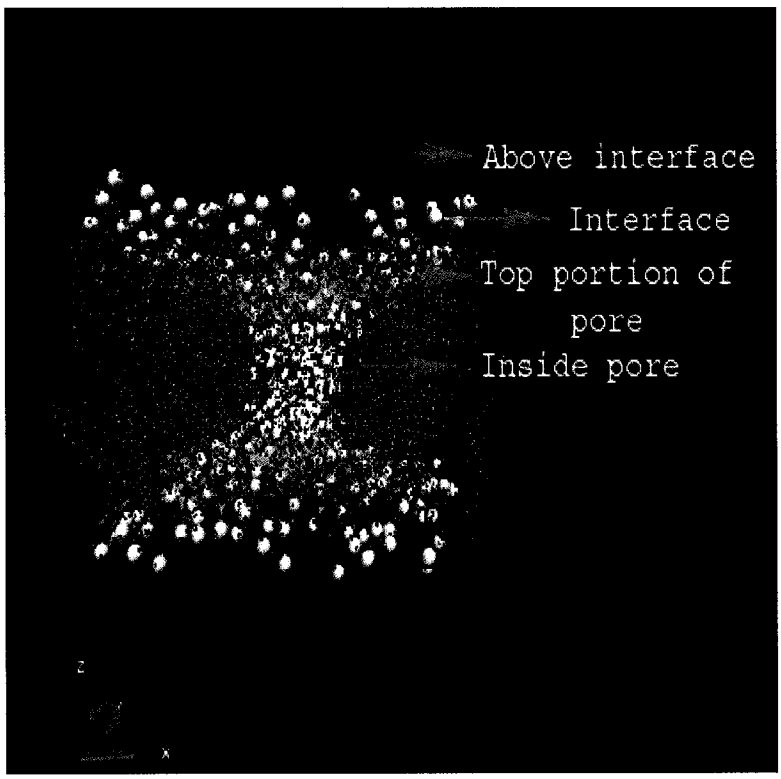


Fig. 4.6. The initial molecular configuration of a DPPC membrane segment with a central nano-pore at the start of MD simulations.

The nanopore itself is divided into three layers—a top and bottom layers that are symmetrical, and a middle layer corresponding to the central pore region. Results for the diffusion coefficient calculated from velocity auto-correlation are first presented. The velocity autocorrelation function necessary for these computations is shown in Fig. 4.7, for bulk water as an example. The relaxation times for water (and other lipid bilayer) molecules are relatively fast, and occur on timescales of 10 ps or less, as discussed in the literature (104). These timescales are consistent with our numerical observations, though our simulations were run for much longer times. Different electric field values ranging from 0 to 1 V/m were used. The field-dependence was seen to be negligible, and so only the zero-field plot is shown in Fig. 4.7. The heavy molecular mass, coupled with the isothermal relaxation used in our MD simulations, precluded any field-driven, energy-dependent effects. In Fig. 4.7, the velocity auto-correlation function C(t) starts from unity, and rapidly begins to decrease as the water molecules undergo collisions and change the direction of their velocities. For a purely Brownian motion with weak scattering, one might expect C(t) to display an exponentially decaying behavior. However, memory effect and the strong inter-atomic interactions change the temporal response. The strong molecular interactions keep individual atoms rattling around in localized regions. The high density environment surrounding each molecule effectively establishes fluctuating potential ''cages'' with localized trapping on short timescales. Eventually the molecules randomly break away. Hence, as seen in Fig. 4.7, C(t) exhibits a slight plateau and even a minor ''bump'' following the rapid decrease. Eventually C(t) goes to slight negative values as the direct result of velocity reversals within some water molecules due to strong mutual scattering. Repulsive potentials that become dominant at very small inter-molecular separations also contribute. Physically this corresponds to a ''rebound'' of the water molecules from the shell of its neighbors. The overall simulation result for bulk water obtained here is in good agreement with other reports published in the literature (104).

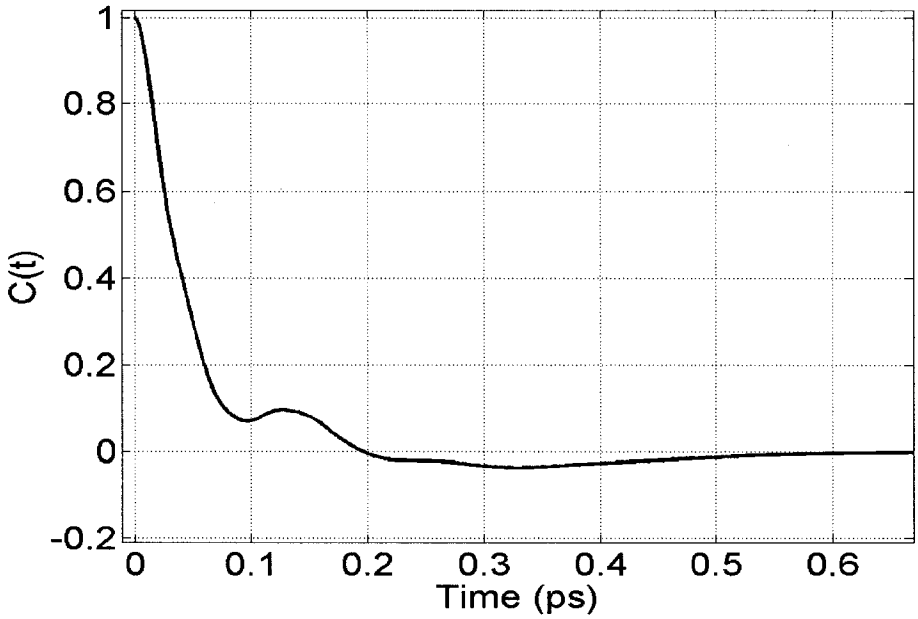


Fig. 4.7. Calculated velocity auto-correlation function for bulk water.

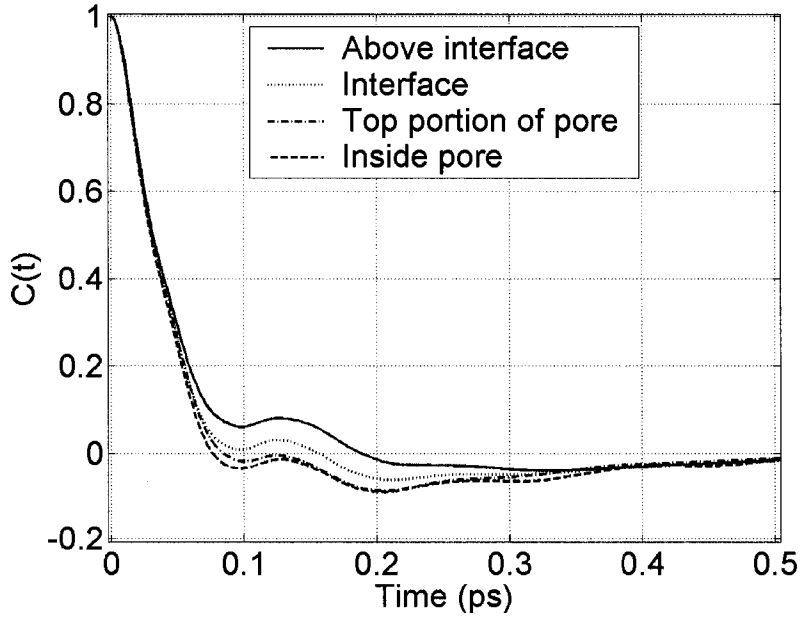


Fig. 4.8. MD results for the velocity auto-correlation function for water within different membrane regions.

Having obtained reasonable results for bulk water, MD simulations were carried out for the velocity auto-correlation within the different membrane regions. The results appear in Fig. 4.8, and the general trend is similar to the previous case for bulk water. The velocity auto-correlation within the central pore is the smallest. This is to be expected since diffusion in lower-dimensional confining geometries is always smaller than in three-dimensional bulk. Scattering primarily occurs perpendicular to the membrane, i.e., along the z-axis. Velocity randomization is faster because of a higher possibility for large-angle back-scattering in a quasi-one-dimensional geometry. The corresponding frequency-dependent diffusion coefficients D(x), in the various membrane regions as well as for bulk water, are shown in Fig. 4.9 and Fig. 4.10. These D(x) plots show the static diffusion coefficient to be the highest for bulk water and the smallest inside the pore. Values range from about 0.5 x $10^{-9}$ to 6 x $10^{-9}$ $m^2$ $s^{-1}$. The peak is predicted to occur roughly around 1.4 x $10^{12}$ $s^{-1}$.

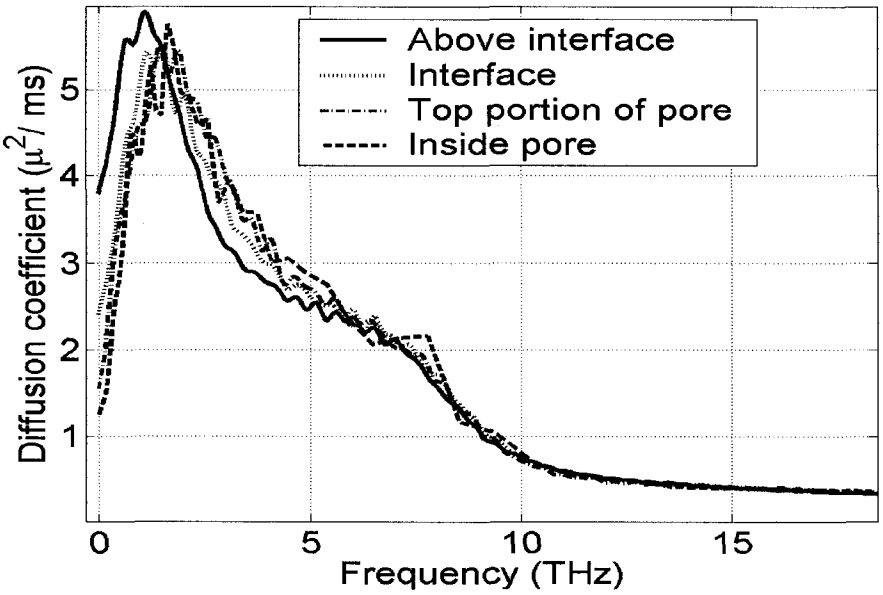


Fig. 4.9. Calculated frequency-dependent diffusion coefficient for various regions around the membrane.

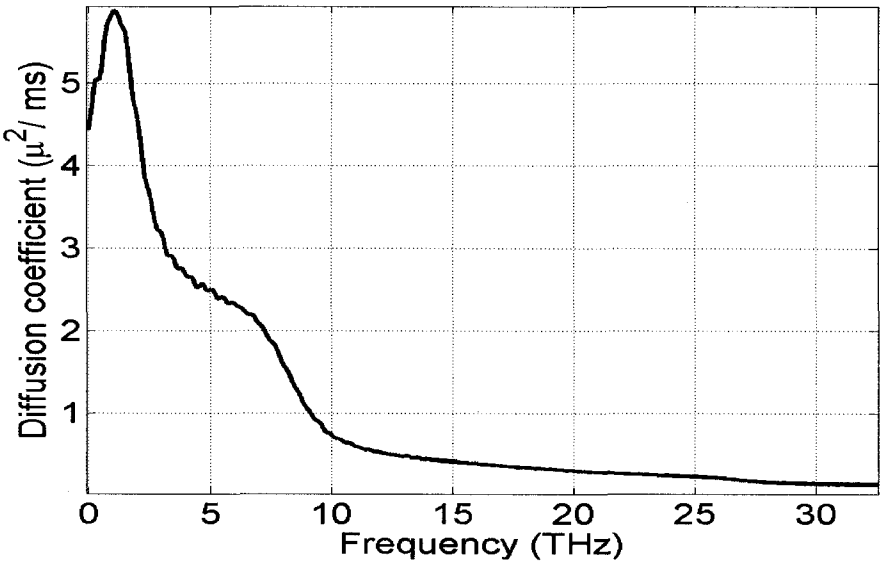


Fig. 4.10. Calculated frequency-dependent diffusion coefficient for bulk water.

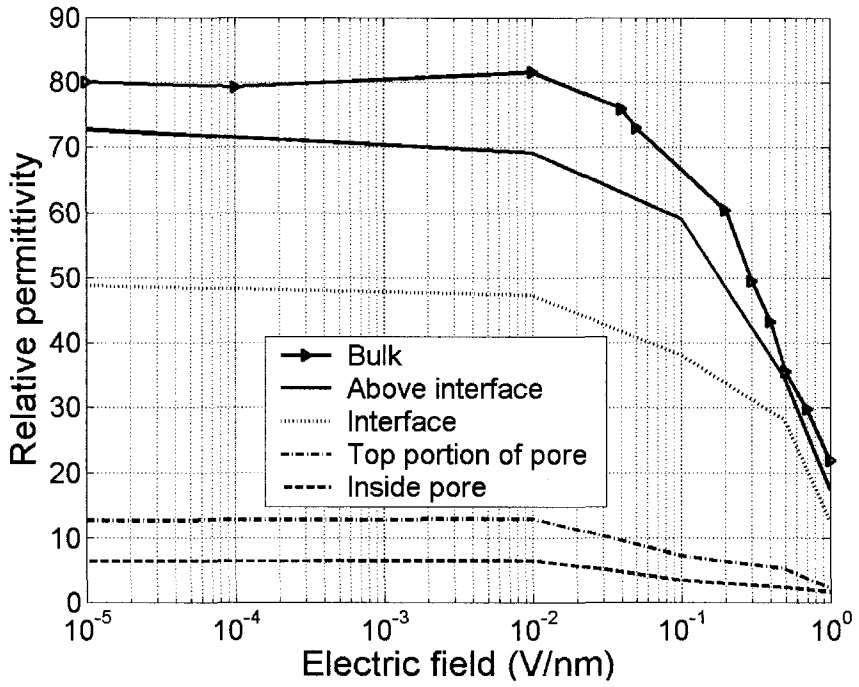


Fig. 4.11. Results of the field-dependent relative permittivity across different membrane regions. Bulk values match previous reports (105).

The $4.5 \cdot 10^{-9}$ $m^2$ $s^{-1}$ value for the static diffusion coefficient for bulk water is close to other reports (106), but slightly larger than the experimental value of $3.5 \cdot 10^{-9}$ $m^2$ $s^{-1}$ at 323 K. Though the precise quantitative value will depend on the specific model chosen for water, the general overall trends are all reasonably in line with known data.

Simulation results for the relative permittivity across various regions in the membrane vicinity are given in Fig. 4.11. As may be expected, the highest value was obtained for bulk water. The current results for bulk water match an earlier report by Yeh and Berkowitz (105) very well. As is well known, dielectric constants evaluated from molecular simulations do not yield the experimental value of 80. The magnitudes are generally lower and depend on the model interactions used in the computations. Here, our primary interest is to quantify the relative changes and their spatial inhomogeneities over atomic distances near cell membranes. Towards this end then, the simulation values were scaled up slightly to coincide with the experimentally accepted, zero-field value of 80. These are the resulting plots of Fig. 4.11. The low field value inside the pore region is predicted to be slightly below 8. This low value arises from a finite size effect due to the inability of water molecules to move along the transverse dimensions. Qualitatively, this reduces the ability of this fluid to adjust dynamically and screen charges. The plots also predict virtually no field dependence below 100 kV/cm. A plot of the MD results for the dipole moment variations at 0.1 V/nm within different regions is shown in Fig. 4.12.

Cellular electroporation is generally accepted to begin at a transmembrane potential threshold of about 1 V. Roughly, for a 5 nm thickness, this corresponds to an electric field of 2000 kV/cm. This is clearly a regime in which the permittivities can be expected to be much lower than the static, low-field values generally assumed. At these fields, the region adjacent to a cell membrane is predicted to have a relative permittivity of only 35. It is, therefore, important to include such field-dependent effects into macro-models and other transport calculations. Besides, such field-dependent decreases in

dielectric constant can be expected to give rise to a localized positive feedback mechanism in the

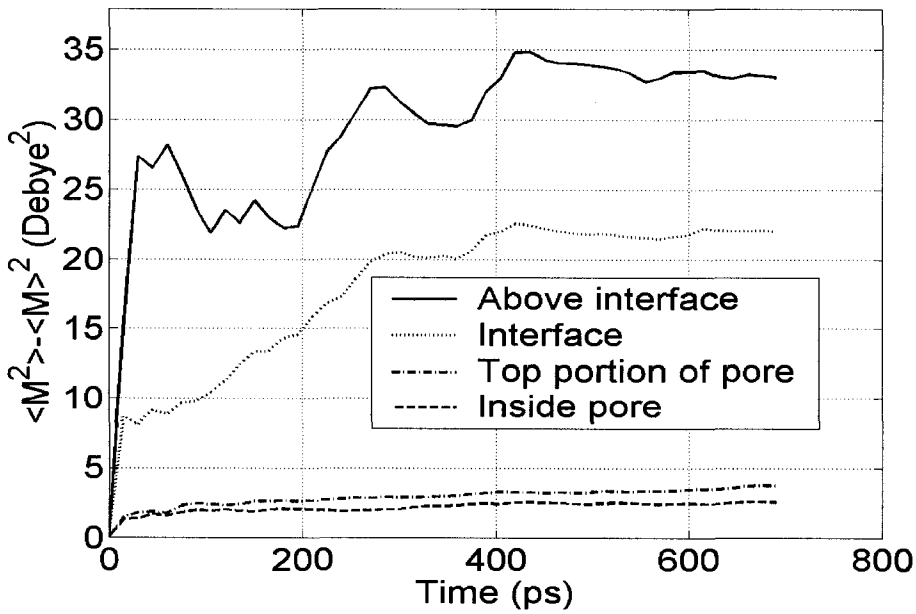


Fig. 4.12. Dipole moment variations across different membrane regions.

following manner. Increases in local electric fields (due to externally applied voltages, for example) would reduce the permittivity. Effectively then, the capacitance of a local elemental volume would decrease. In the absence of conduction current flows across the membranes at the early times (pre-electroporation regime), displacement currents dominate. Requirement of total current continuity, would naturally lead to an enhancement in the rate of voltage increase, to offset the permittivity decreases. Hence, the transmembrane voltage would rise faster, further reducing the permittivity and setting up a positive feedback mechanism.

## 4.6 Membrane Fragmentation

The traditional electroporation model seems to work well for relatively low-to moderate electric fields (200 V/cm - 5 kV/cm). However, it appears to be inadequate in explaining several of the observed phenomena at high electric field strengths.

The various inadequacies with regards to experimental reports are listed below.

(i) The high-field experimental data indicates strong conductivity increases of the cell solution at the very beginning of a high voltage pulse (45). Our current experimental data sets (discussed in the next section) show conductance increases far exceeding values that might be predicted on the basis of simple membrane electroporation or dissolution. Also, such increases cannot be attributed to field-induced Wien effects.

(ii) The *fast decrease* in conductance (45) after the pulse cessation is observed that is not compatible with pore shrinking or sealing. The re-sealing process for electro-pores is known to be slow and can take up to several seconds to minutes (46). An additional point of interest is the vesicle formation at the plasma membrane (i.e., blebbing) that has been observed (47). This aspect is not addressed by the electroporation models.

(iii) Recent reports by Tekle et al. (44) show *loss of the phospholipid membrane* during high voltage pulsing. This phenomenon was shown to occur in addition to a pore formation process. Their results demonstrated that up to 14 percent of the membrane surface could be lost upon electric field application.

The following hypothesis can then be evoked, (i) The high externally applied electric fields causes electroporation and forces water inside the bilayer structure; (ii) Spatial confinement of water molecules within the nano-pores effectively reduces the liquid permittivity. Such reductions in dielectric constant due to finite-size effects are well known (107), and arise from the inability of dipoles to effectively screen potential, as their free movement is curtailed; (iii) The high electric field near lipid membrane surfaces

also facilitates the movement of charged molecules [e.g., phosphatidyl-serine (PS)] causing further structural re-arrangement; (iv) Since the permittivity (ε) decreases with electric field, a positive feedback mechanism would arise. Any field-induced reduction in permittivity (ε) would lead to further increases the local electric field since the displacement vector D = εE is roughly constant. This local increase, in turn, would produce further reductions in permittivity; (v) The presence of a high electric field could also alter the electronic states and cause energy-level mixing through the Stark effect. It could become possible for the hybrid bonding states of one site to align with the anti-bonding energies at adjacent sites. Field induced electronic transfer (e.g., hopping), leading to the weakening of molecular bonds could then follow as a naturally consequence. Hence, field-assisted fragmentation and micelle formation might be facilitated in the presence of high fields.

### 4.6.1 Atomistic Simulations

To prove the above hypothesis, MD simulations were performed to show possible membrane loss upon the application of high electric fields. The dipalmitoyl-phosphatidyl-choline (DPPC) membrane was chosen with some embedded PS molecules, and the force fields for membrane molecular motion taken from the literature. This structure is similar to the one used for PS externalization simulations. In all a total of 169,891 atoms were used comprising of 54,485 water molecules, 119 DPPC chains, 9 phosphatidylserine and 9 Na+ ions for overall charge neutrality. Fig. 4.13 shows the initial configuration of a lipid bilayer structure at the start of MD simulations. The membrane was comprised of a 8 x 8 square grid at the top and bottom surfaces. A constant, large electric field of 0.6 V/nm was imposed perpendicular to the membrane. The electric field value used here is large and this choice perhaps needs some explanation. The corresponding transmembrane voltage at this field is roughly 3 Volts. For traditional electroporation, the accepted potential values are on the order of 1 Volt. However, for short-duration pulses highly non-equilibrium conditions exist, giving rise to transient overshoots in transmembrane

voltage (10). Hence, the use of membrane voltages larger than 1 Volt under transient conditions is not unphysical.

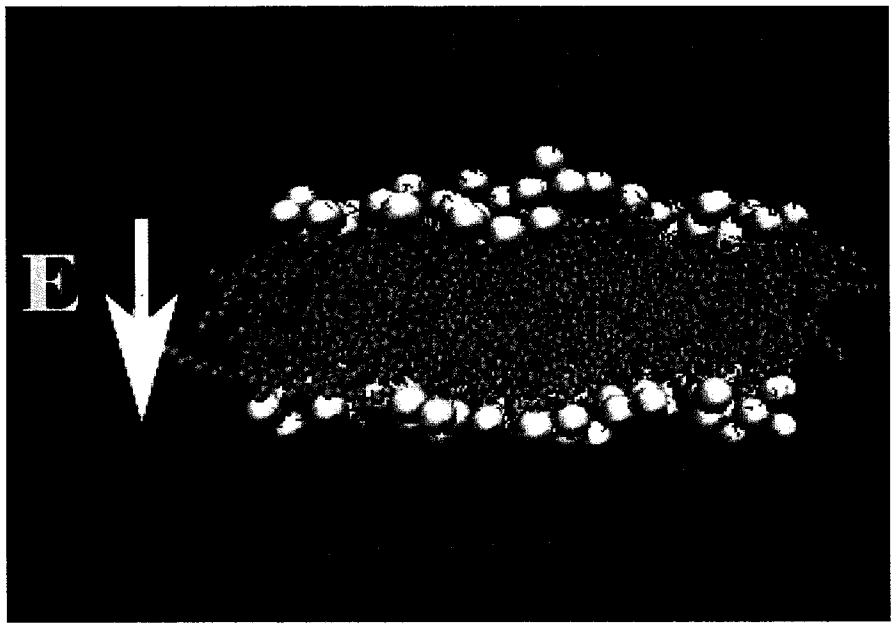


Fig. 4.13. The initial configuration of a DPPC lipid bilayer used for the MD simulations. Water is shown in brown, lipid headgroups in yellow and lipid chains in cyan.

Also, MD simulations are very computationally intensive and require small time steps in the femto-second range. Calculations of the dynamic response can only be carried out to tens of nano-seconds. In actual practice, membrane effects under a high external field could take as long as milliseconds to manifest. So here, a very high electric field was deliberately chosen to increase the driving force, and hence, produce a tangible outcome within tractable time scales. Since the underlying physics produced by the external field would be the same, the high value used here simply allows for the attainment of the final state at much shorter times – thus a "steered" result. Since the present focus is on the "proof-of-concept," and it is adequate to quantitatively demonstrate the final outcome via such "numerically accelerated testing."

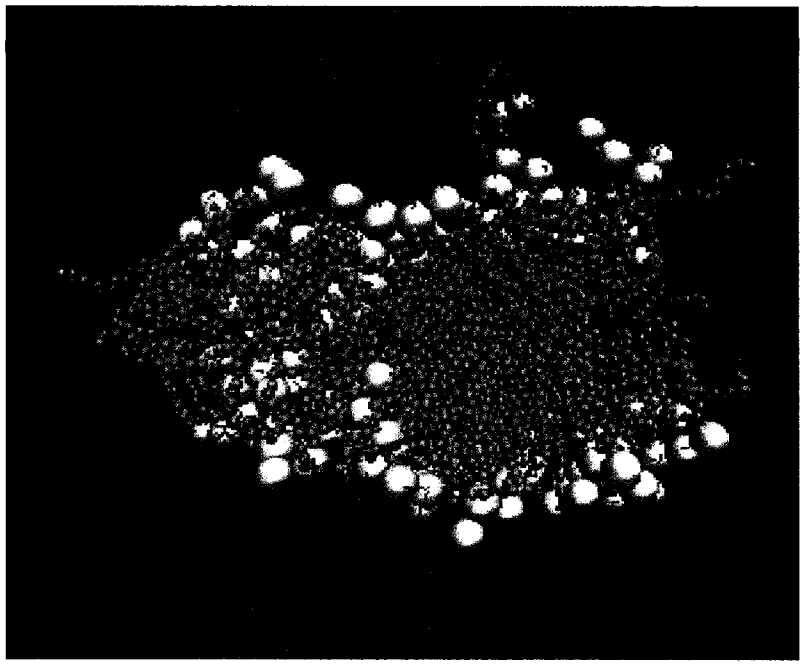

Fig. 4.14. Snapshot of the DPPC lipid bilayer patch at 1.85 ns. Slow membrane fragmentation is predicted during the electric pulse.

A snapshot of the membrane patch shown in Fig. 4.14 at 1.85 ns reveals the membrane disruption and the on-set of fragmentation. The head-groups are beginning to separate and move into the aqueous medium. Our results strongly suggest an intermediate state of a closed hydrophilic pore (HI), representing a non-conductive pre-pore on the pathway to a final HI pore. The fragmentation is more obvious in Fig. 4.15, which is a 2.05 ns snapshot from the MD simulations. The 0.6 V/nm field acting on a charged PS lipid molecule roughly corresponds to a 96 pN force that facilitates lipid extraction from the DPPC membrane. This force is slightly lower than previous estimates for bio-membrane rupture (108) based on pure mechanical stress. A slight lowering on the force requirement in this electric field context is perhaps to be expected based on the following qualitative aspects. Lipid bilayer membranes derive their resilience to structural dissolution, in part, by the hydrophobic interactions between lipid tails and the surrounding water. This interaction helps keep the lipid tails sequestered away from the water, maintains the structure and prevents membrane break-up. However, unlike pure mechanical stresses, the application of external electric fields creates nano-pores and lowers the local permittivity. Forced entry of water into the lipid bilayer system weakens

the drive towards an organized structure. Collectively, electrostatic forces tugging on charged ions, the short-range dipole interactions, reductions in localized aqueous permittivity, and the possibility for increased entropy, all serve to facilitate lipid membrane fragmentation under strong external electric fields.

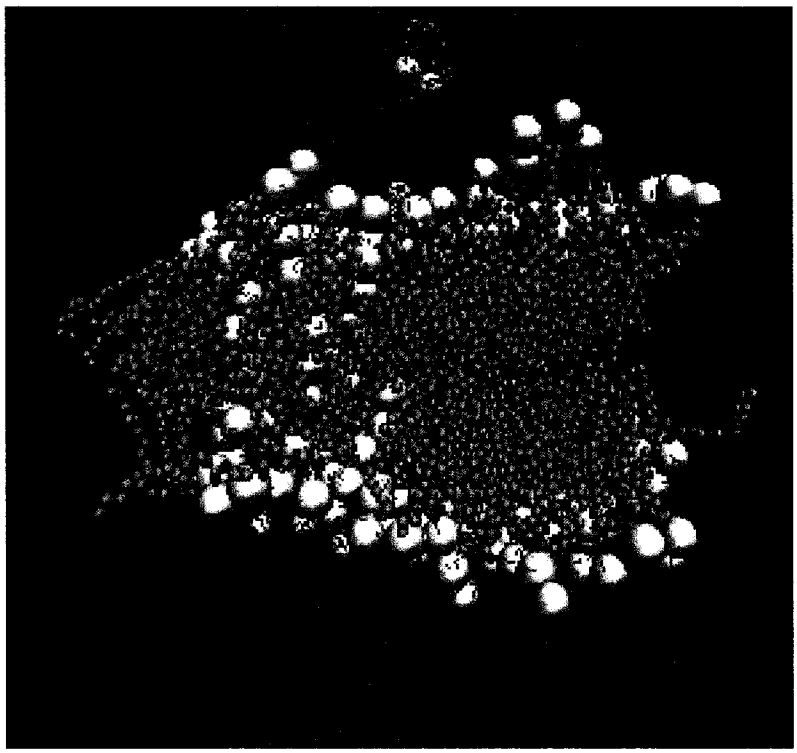

Fig. 4.15. A 2.05 ns simulation snapshot of the DPPC lipid bilayer patch with the voltage pulse applied. One lipid at the anode side (top) is seen to break loose.

The above MD simulations clearly demonstrate the following aspects: (i) It is possible to get membrane rupture and fragmentation in response to a large externally applied electric field. In practice, such effects are expected to occur at the poles due to the highest electric fields in those regions; (ii) The effects are predicted to be stronger at the anodic side due to the existence of negatively charged molecular species within membranes; (iii) The ejection of lipid molecules from parts of the membrane has been shown to occur. Furthermore, such fragments are likely to cluster together and form

micelles in the immediate vicinity of the parent membrane; (iv) Finally, though not shown here explicitly, it is conceivable that the uncharged micelles would tend to diffuse back and self-organize into the parent membrane. However, micelles containing charged entities would drift away due to the applied electric field, and also due to the mutual electrostatic repulsion between different micelles. Upon termination of the electric field, not all of such charged micelles would coalesce back due to the mutual electrostatic repulsion. Hence, a certain fraction of the membrane segment might be lost, in keeping with the reports of Tekle et al. (44).

## 4.7 Possible Field Induced Cytochrome C Release

Mitochondria, often termed as the energy power house of cells, plays a major role during the initiation of apoptosis. The release of different membrane and globular proteins inside the mitochondria is regarded as one of the causes and triggers of programmed cell death. One of this membrane proteins which plays a very important role is Cytochrome C. The exact mechanism by which Cytochrome C release is not well understood, but there are studies (109) which showed that cytochrome C release generally occurs in two steps. In the first step, Cytochrome C, which is bound to inner membrane of mitochondria through cardiolipin (110), gets detached. In the second step, this Cytochrome C diffuses into the cytoplasma. The experimental results on isolated rat liver mitochondria also showed this 2-step release of Cytochrome C release (109). This mechanism appears to be reasonable based on electrostatic considerations. A brief supporting, qualitative explanation is provided here. Cytochrome C has positively-charged lysine residues which bind to negatively-charged phosphate groups of cardiolipin. During the application of electric field, a membrane rupture in the inner mitochondrial membrane (the inherent electroporation process) could aid in creating the "exit doorway" for Cytochrome C release from the inner mitochondria. The external electric field could also help separate Cytochrome C from cardiolipin based on the electrical driving force. Once this happens, the positive charge of Cytochrome C would conceivably help it drift further away from the cardiolipin (or inner mitochondrial

membrane). This membrane rupture/poration coupled with Cytochrome C separation from cardiolipin leasing to an overall cytochrome C release thus looks plausible. Here, simulations showing poration of twin-bilayer system, as present in the mitochondrial machinery, is given next. The reason for performing simulations on twin-bilayers is explained in detail in next section.

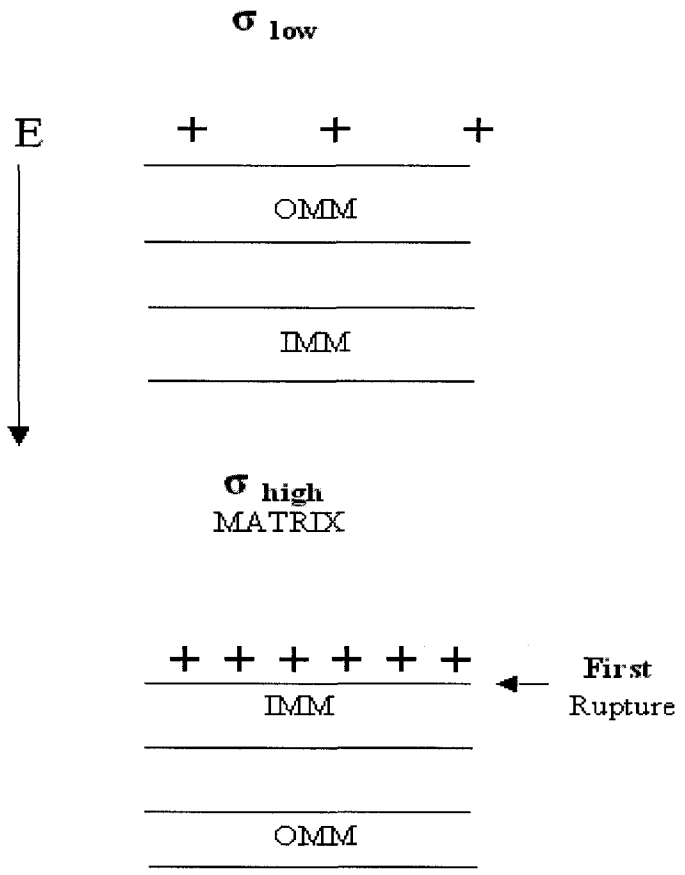


Fig. 4.16. Schematic of the double layer mitochondrial system. Outer Mitochondrial Membrane (OMM) / Inner Mitochondrial Membrane (IMM) model.

Unlike the cell or nucleus, mitochondria have inner and outer membranes separated by few nanometers. There are some contact sites between these inner and outer mitochondrial membranes, where the distance between them is supposedly very small, on

the order of ~1-10nm. These contact sites (also known as complexes), and the inner membrane generally have the phospholipid cardiolipin. It is also known that the inner mitochondrial content is more conductive than the outer cytosol. Thus, it is reasonable to suppose that the inner mitochondrial region has a higher ionic concentration, and this could lead to stronger build-up of localized charge densities upon external electric field application. In the schematic of Fig. 4.16, the potential build-up across the cathodic side of the outer membrane/inner membrane system could thus be higher as compared to that on the anodic side. The greater charge build-up at the cathodic side of the IMM (due to the high conductivity of the mitochondrial matrix) would fashion this asymmetry as shown in Fig. 4.16.

As a preliminary first step towards testing the above hypothesis of cytochrome C release from the mitochondria, MD simulations on twin-bilayer system were performed. The twin-layer mimics the mitochondrial structure. Clearly this is an initial first step, since a variety of factors are expected to be at play. These involve miochondrial membrane poration, the possible role of cardiolipin, their possible separation and finally the exit of cytochrome C through the porated membrane. The gap between the twin bilayers was taken to be around 1nm as shown in Fig. 4.17(a). For simplicity, Fig. 4.17(b) shows the bilayer structure with solvent around, but without the lipid tails for purposes of clarity. Fig. 4.17(c) shows the initiation of water defects at time instant t = 6.6ns on the top side of the twin-bilayer system. The time taken for the pore formation in one of this twin bilayer structure is somewhat larger than that for poration for a single bilayer membrane. This can be explained as follows. The solvent sandwiched between the bilayers has very little space to move and as a result the water dipoles are practically immobilized. Hence, the permittivity is almost an order lower than that of the bulk water . Treating this bilayer-water-bilayer system as capacitors in series, the permittivity of the whole system in the electric field direction can be found to approximately be that of the bilayer (~8). Thus, the system can be considered to effectively be a dielectric with permittivity of approximately 8 and length 10nm (=4.5 nm + 1 nm + 4.5 nm). As a result,

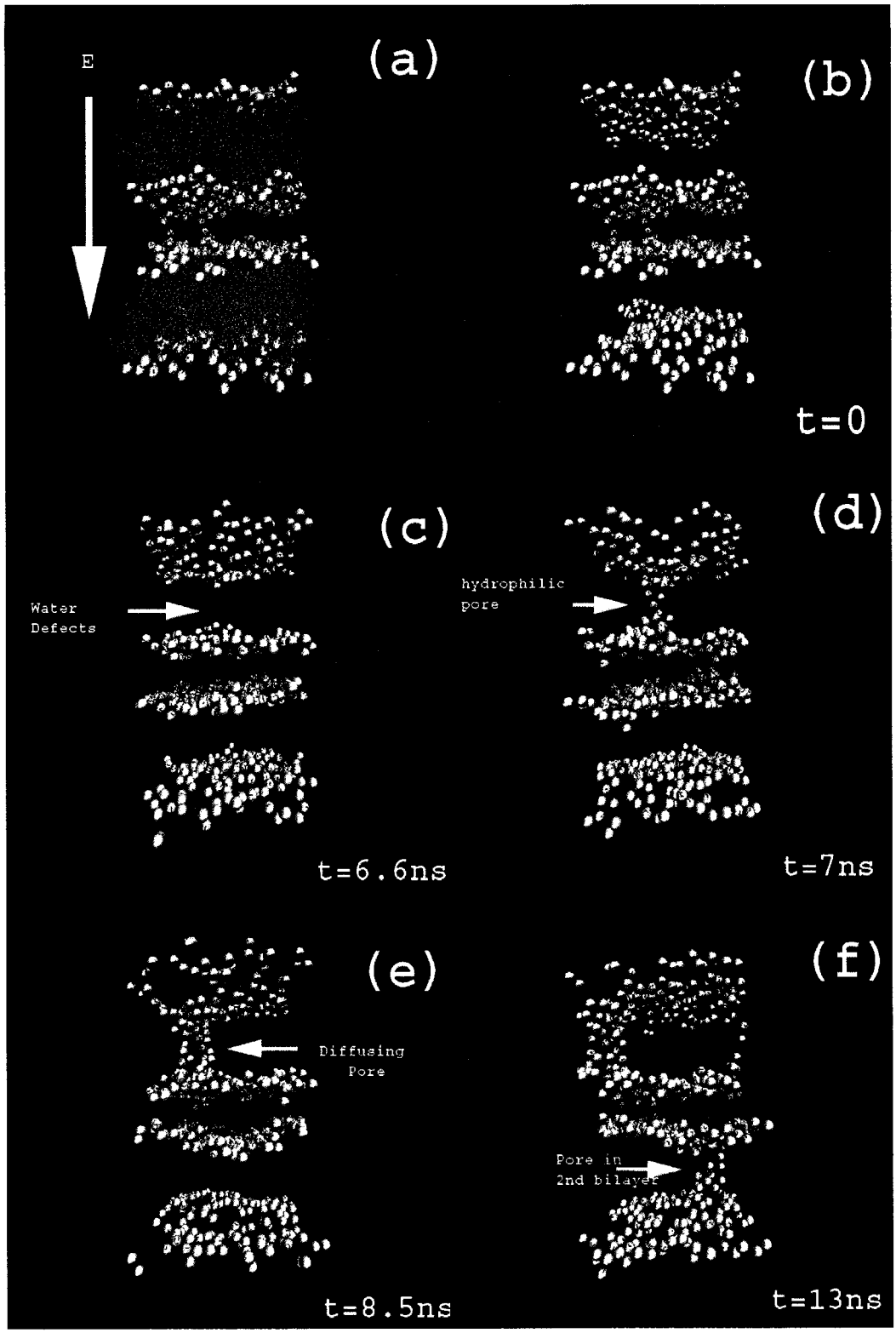


Fig. 4.17. Pore formation in 2 bilayer system. This system resembles Outer mitochondrial membrane (OMM) /Inner mitochondrial membrane (IMM) model.

the time taken to charge this twin-bilayer system will be more compared than that required for a single bilayer membrane. With more time needed to set up the critical poration field, pore formation in the composite membrane can naturally be expected to take longer. Fig. 4.17(d) shows the hydrophilic pore formation. Fig. 4.17(e) shows the diffusive/drift movement of the lipid molecules within the bilayer system. Following an initial poration event, a second hydrophilic pore formation is predicted to take place in the second bilayer a time of about t=13ns.

## 4.8 Electric-field Induced DNA damage

Most of the molecular dynamics simulations done on DNA were the studies of hydration shell around it (111, 112). These studies were possible after several x-ray crystallography experiments on DNA molecule (113). There were also a number of proposals for including nucleic acid force-fields for more accurate simulations (114). Here, results on MD simulations of oligonucleotide dodecamer d(CGCGAATTCGCG) are presented and discussed. One of the main goals was to see the possibility of deformation and/or fragmentation of DNA bonds upon the application of high electric field.

The initial structure of the DNA oligomer considered is shown in Fig. 4.18(a). This DNA molecule has a charge of -22e. So, 22 Na+ molecules were added to neutralize the charge of the system and maintain overall neutrality. The electric field applied in this simulation was taken to have a constant value of 4V/nm. This high electric-field of 4V/nm perhaps needs an explanation. The dimensions of the DNA structure taken for these simulations are less than a cubic nanometer and have only 12 base-pairs. Generally, DNA's are very long and have thousands of base-pairs. If that were the case, the charge of the DNA molecule considered will be very large, owing to the strong electrical effects upon the application of lower electric-fields. For this reason, instead of taking long realistic DNA, a short DNA was simulated at higher electric field. This was done in part

to speed up the computational time. Similar simulations have been recently carried out to demonstrate the diffusion of plasmid DNA through the lipid bilayer at 1V/nm (53).

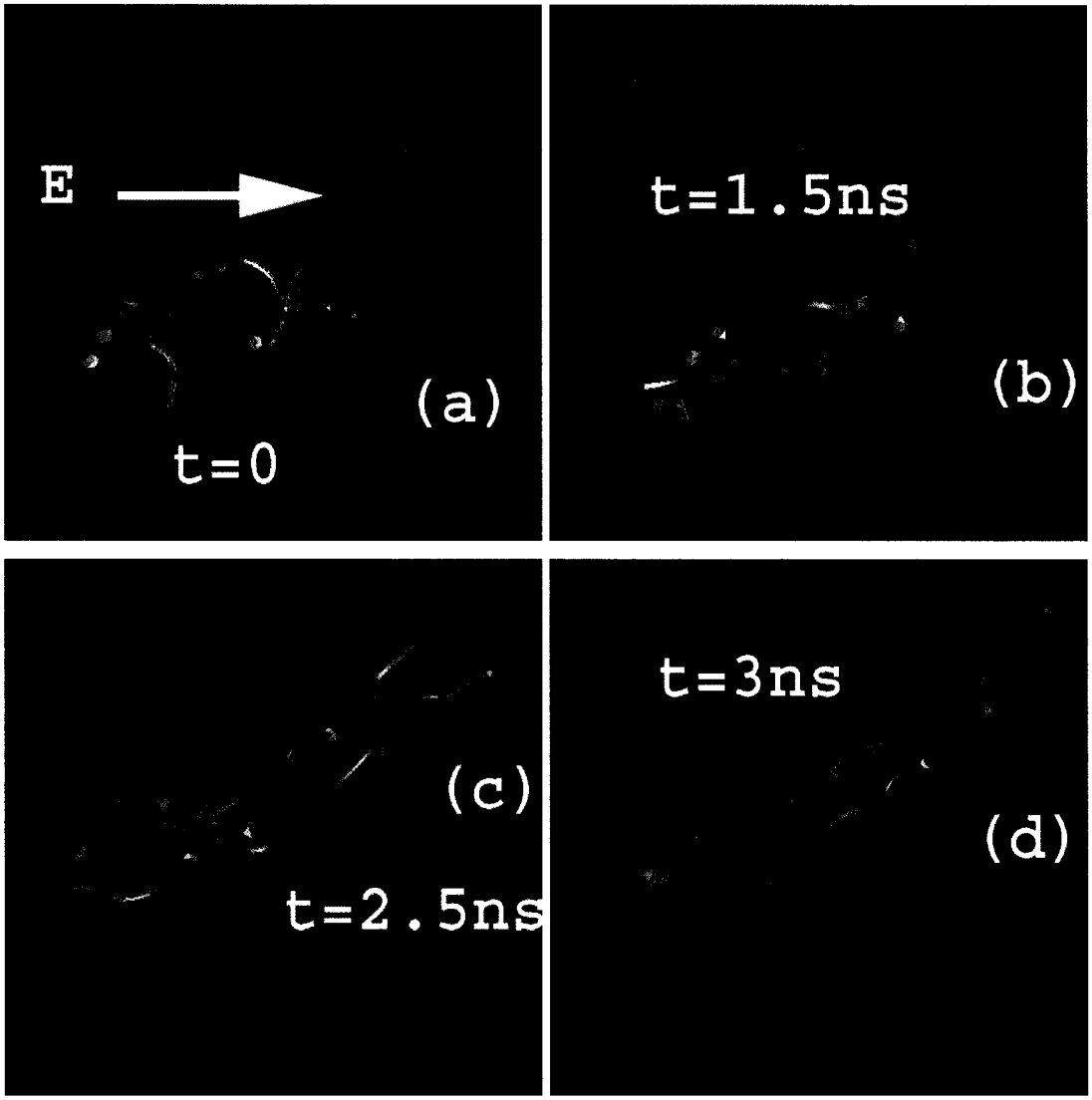


Fig. 4.18. Electric Field Induced DNA damage.

The results of the simulation are described here. Fig. 4.18 (b) shows the DNA structure at t=1.8 ns during the application of electric field. It can be seen that the double-helix is starting to break-up. This break-up is more clear and evident in Fig. 4.18 (c),

which is at t = 2.2 ns. Eventually, all the bonds between the double-helix are broken as shown in Fig. 4.18 (d). This looks like double-helix getting separated into 2 single strands. Thus, these preliminary simulations are indicative of the possibility of electric field induced DNA damage.

## 4.9 Electric Field Induced Intracellular Calcium Release

Simulations for the time-dependent calcium concentrations within both the cytoplasm and endoplasmic reticulum, in response to a 60 ns, 15 kV/cm electric pulse were carried out. These electrical pulse parameters were chosen to match previous experimental reports (115) on electric-field-induced calcium release. The mathematical model is described in detail in Chapter III. All calculations assumed an absence of extra-cellular calcium and hence can be considered as a closed-cell situation as shown in Fig. 4.19.

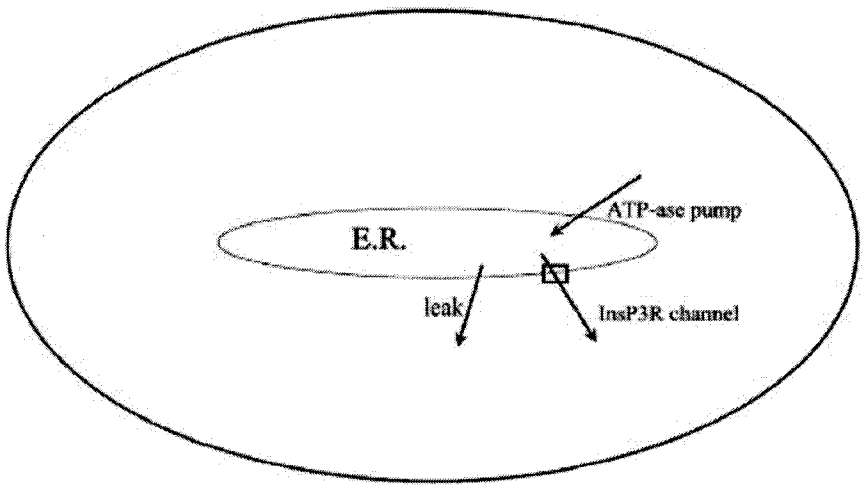


Fig. 4.19. Closed-cell situation model.

A very brief summary of the simulation results is presented here. The results for the averaged $Ca^{2+}$ concentration in the cytosol are given in Fig. 4.20. The plot also

includes experimental data points that have been reported in the literature (116). In Fig. 4.20, the $Ca^{2+}$ concentration starts from an initial 0.1 μM value and increases in time to a maximum of about 0.23 μM. The data is for HL-60 cells. The sharp increase, seen during the initial phase, is due to electric field-induced poration within the ER that leads to a $Ca^{2+}$ outflow. Drift rather than diffusion is the primary transport mechanism during this initial phase when the external voltage remains applied. Beyond this initial sharp $Ca^{2+}$ release, IP3R-activated calcium transfer arising from the CICR mechanism begins to set in. A slow and more gradual recovery down to the initial concentrations is predicted, with final steady state being achieved after about 300 seconds. This ~ 4-5 minute recovery time is in accord with reported measurements (116). The experimental data of White et al. (116) are also shown in Fig. 4.20, and matches the predictions well. The model predictions were within the experimental error deviations for all the points. Due to limitations in the temporal resolution of experimental techniques, values of the $Ca^{2+}$ concentration at the earlier times could not be measured, and hence, such data points could not be shown. The experimental data in Ca-free extra-cellular environments (11,116) is in accord with this prediction.

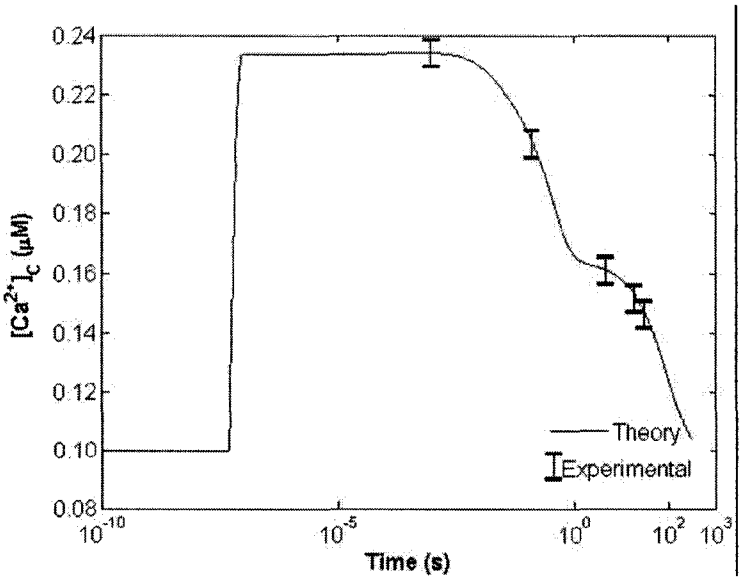


Fig. 4.20. Simulation results for average Ca-concentration in cytosol as a function of time. The experimental data points are from the reports White et al. (116).

# CHAPTER V

# SUMMARY AND SCOPE OF FUTURE WORK

## 5.1 Introduction

Ultra-short, high-field pulses open the way to targeted and deliberate apoptotic cell killing (e.g., of tumor cells). Though experimental data is very useful, it usually yields information on macroscopic variables that is inherently an average over time and/or space. Measurements often do not provide the molecular level information or details, as might be possible through numerical simulations. Here we focus on the MD technique, as it provides the most comprehensive, time-dependent, three-dimensional nanoscale analyses with inclusion of the many-body aspects. This dissertation research presents simulations and analyses of several aspects including membrane poration and its dynamics; predictions of transport parameters under high-field, non-equilibrium conditions; electric fields effects on DNA; micelle disintegration; protein unfolding; and intra-cellular calcium release. Summarizing conclusions on the simulations done in this dissertation research is presented briefly in Section 5.2, while Section 5.3 points to few potential problems that can be solved using MD simulations. This section is basically the scope of future work.

## 5.2 Summary of Research

This section basically summarizes the simulation results already presented in Chapter IV in this dissertation research report. These include DPPC membrane Poration, PS externalization in DPPC-DPPS membrane, calculation of transport parameters and permittivity of water molecules inside the pore as well as near the membrane, high

electric field effects on DNA double helix, simulations showing membrane fragmentation and also continuum approaches used to simulate electric field induced calcium release.

### 5.2.1 Membrane Poration and PS Externalization

The MD simulator was used to probe the pore-formation dynamics, assess the size and temporal duration of the membrane pores, analyze the electrically driven PS-externalization process, and study the physics underlying the observed polarity dependences. The above was carried out using "all-atom" models of pure DPPC and a combination of DPPC–DPPS lipid molecules.

### 5.2.2 Transport Parameters for Electroporation Analyses

Transport analysis and evaluations of the membrane dynamics are often based on simplified approaches that use a set of macroscopic parameters. However, these parameters are field dependent, and in the vicinity of the membrane would have strong spatial variations. Here, microscopic details and inhomogeneities have been considered based on molecular dynamics applied to a DPPC membrane structure. The results given here could primarily be applied to coarse-grained, macroscopic transport modeling work and can play a vital role in understanding transport phenomena of drug delivery.

### 5.2.3 Electric Field Induced Membrane Fragmentation and DNA damage

The physical phenomena of electrically stressing cells to high external voltages has been shown to cause significant increases in conductivity of the cellular medium and that this conductivity rapidly decreases upon voltage termination. Such conductivity increases and the relatively fast conductivity turn-offs cannot be accounted for on the basis of simple electroporation alone. A new hypothesis of localized membrane rupture

and fragmentation on the "nanoscale" at high electric fields has been proposed in this dissertation work and the hypothesis was supported with MD simulations. Finally, such application of high external voltages on cells might damage DNA and could also porate double-membrane of mitochondria possibly leading to cell death. Initial MD simulations on DNA and mitochondrial double membrane system have also been shown in the present dissertation report.

### 5.2.4 Electric-Field Induced Calcium Release

The objective of this study constitutes a first step in quantitatively probing the time- and spatially-dependent modulation of calcium dynamics through the application of external voltages. The simulation results have been shown to be in agreement with the observed calcium dynamics in experiments.

## 5.3 Scope of Future Work

Throughout this dissertation report, a range of discussions were presented spanning from molecular dynamics simulations on membranes, micelles, proteins and water to continuum simulation approaches on calcium dynamics, to show and validate the experimental results of pulsed electric fields on cells. This area of simulations is one of the rapidly growing fields in the world of computational biology. The MD simulation technique, coupled with continuum approaches ("multiscale modeling") can widen the scope for analyses and help in solving a broad array of different problems. Here, a brief discussion will be presented on a few problems of interest that merit subsequent work. These topics include MD simulations on membrane proteins, denaturation of proteins, membrane electro-fusion and multiscale modeling of electrodelivery of bio-active agents.

### 5.3.1 Membrane Proteins

Proteins are the most abundant macromolecules present in the membranes, cytosol, organelles and chromosomes. They constitute more than 50% of the mass of the living cell. The function of a cell membrane generally revolves around its proteins. Different kinds of proteins are found in cell membranes, and are generally globular. They are not held in fixed pattern and they move in the phospholipid bilayer. These proteins normally fall into 3 categories: carrier proteins that regulate transport and diffusion, marker proteins that identify cell to other cells and receptor proteins that allow the cell to receive instructions, communicate and transport proteins, and regulate what enters or leaves the cell. These proteins are either peripheral or integral. As the name implies, peripheral proteins are generally bound to the exterior parts of head-groups and hence can be easily extracted, while the integral proteins are tightly bound to lipid tails and are insoluble in water.

Proteins play crucial roles in dynamic processes within living cells. For example, insulin regulates the metabolism of glucose; rhodopsin converts incoming light in the retina of the eye to ionic signals in the optic nerve. Actin and myosin generate forces in muscle cells. Dynein is an energy-producing component of the cytoskeleton. Kinesin performs intracellular transport. Functional proteins catalyze nearly all cell metabolic proceses. Each functional protein has a specific conformation suited for its function (117). The membrane proteins are a class of proteins that are embedded in the lipid bilayer. Most of the membrane proteins have channels for the exchange of ions and other proteins. It is also proven that around 50 top pharmaceuticals bind to membrane proteins, whose molecular models are available and hence it will be very interesting to understand the molecular details of binding through MD simulations (118). In the next 2 sections, a brief discussion is made on Channel Proteins and Voltage gated ion channels.

### 5.3.1.1 Channel Proteins

One of the proteins which helps in the exchange of ions for ATP and for the metabolism of the cells are the channel proteins. Channel proteins extend through the bilayer and form a pore through the membrane that can move molecules in several ways. One way to understand these channel proteins is to study very simple peptides that form channels. One of the peptaibols is alamethicin, which is a family of fungal peptides.

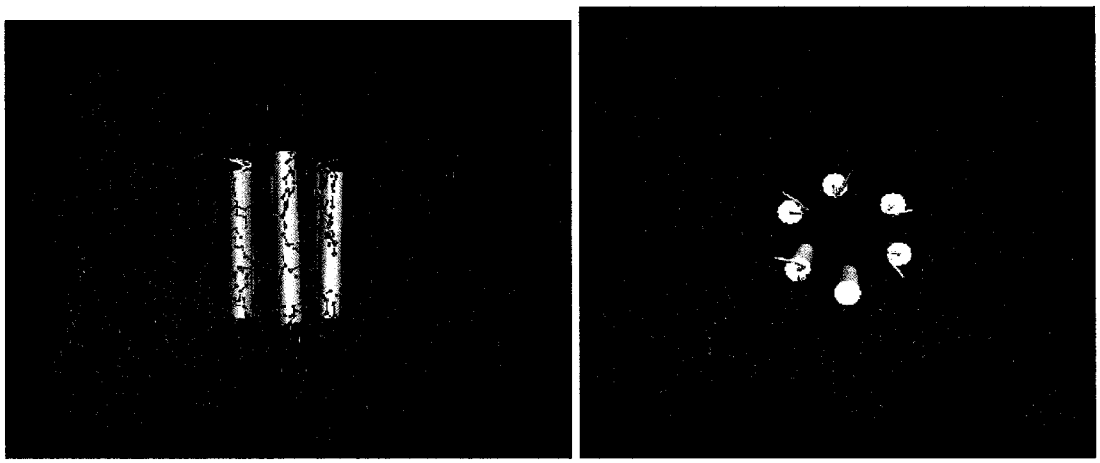

Fig. 5.1. Alamethicin in POPC in side (left) view and top (right) view.

Alamethicin is an alpha helical channel-forming peptide, which inserts into lipid bilayers in a voltage-dependent, asymmetrical fashion. Alamethicin channels have been modeled as parallel helix bundles of transbilayer helices containing between 4 to 8 helices per bundle (119) Previous MD simulations on these varying channel sizes has shown that there is a continous water-filled pore from 6 helices onwards. Alamethicin channel with 6 helices embedded in a bilayer is shown in Fig. 5.1. These kind of channels allow us to use MD simulation to study the conformational changes as well as the conductivity changes upon the application of electric fields.

### 5.3.1.2 Voltage Gated Ion Channels

The remarkable work of Hodgkin and Huxley (120) set the physical basis of the nerve impulse generation and propagation using the giant axon of the squid as a model. In their description, the initiation and conduction of the action potential is the result of a transient influx of Na ions that is followed by an outflux of K ions across the axon membrane. Their voltage-clamp studies revealed that the ion flow through these two specialized pathways occurs with distinctive kinetics and that the conductance of these pathways is voltage dependent.

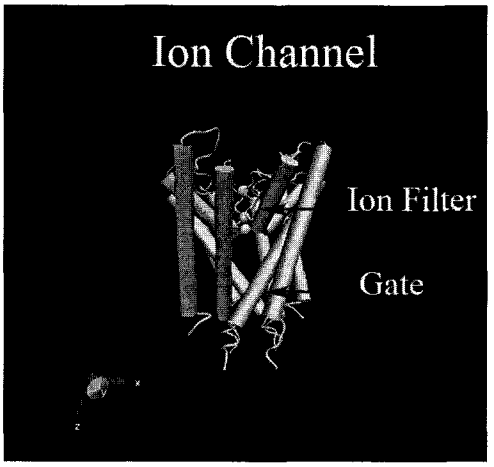


Fig. 5.2. Voltage gated Potassium channel model.

Voltage-dependent ion channels can be thought as made up of three basic units: voltage sensor, pore and the gate. A model of the voltage-gated channel is shown in Fig. 5.2. The exchange of ions through pure lipid bilayer is known to be almost rare, since it takes a large amount of energy to put ions through a low-dielectric constant lipid environment (121). The protein channels help lower this energy barrier and provide ion-exchange capability which, is necessary for cell survival. The gate in the channel allows exchange of selective ions and at selective times. The voltage sensor in the proteins determines these timings. These channels generally have 4 to 6 sub-units. A subunit of the voltage-gated channel is shown in Fig. 5.3. The pore and the gate are formed by S5-

loop-S6 region. The voltage sensor is S1-S4 region, where S4 is composed of charged (positive) amino acid residues and is considered vital in voltage sensing.

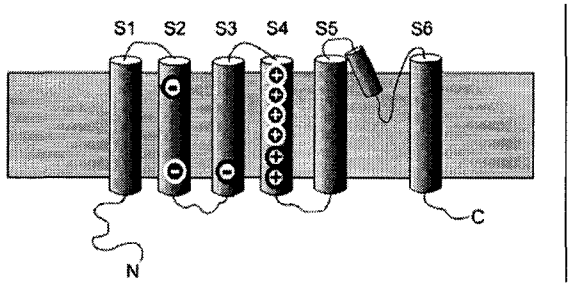


Fig. 5.3. One subunit of Voltage gated ion channels (59).

Some of the recent work on this voltage-sensing mechanism includes different models of this S4 domain. Three current models on this mechanism are shown in Fig. 5.4 and are briefly described below:

1. In the "helical screw" model (shown in (a) of Fig. 5.4), S4 helix moves through the transmembrane region on gating (122). This is shown to be more energetically favourable and many groups are working to prove this hypothesis.
2. In the second model which is known as "transporter model", S4 does not move much upon gating (123). This is similar to helical screw model, but in this model, S4 has to cross 2 barriers, instead of 1 in helical screw model.
3. The third model is known as "paddle model" and is shown in (c) of Fig. 5.4. In this model, S4 lies in the core of the membrane and moves through this unsaturated fatty acids upon gating. The model seems to look energetically unrealistic, but the crystal structures revealed clearly showed that S4 lies in interior and the model can actually work like paddle (124, 125).

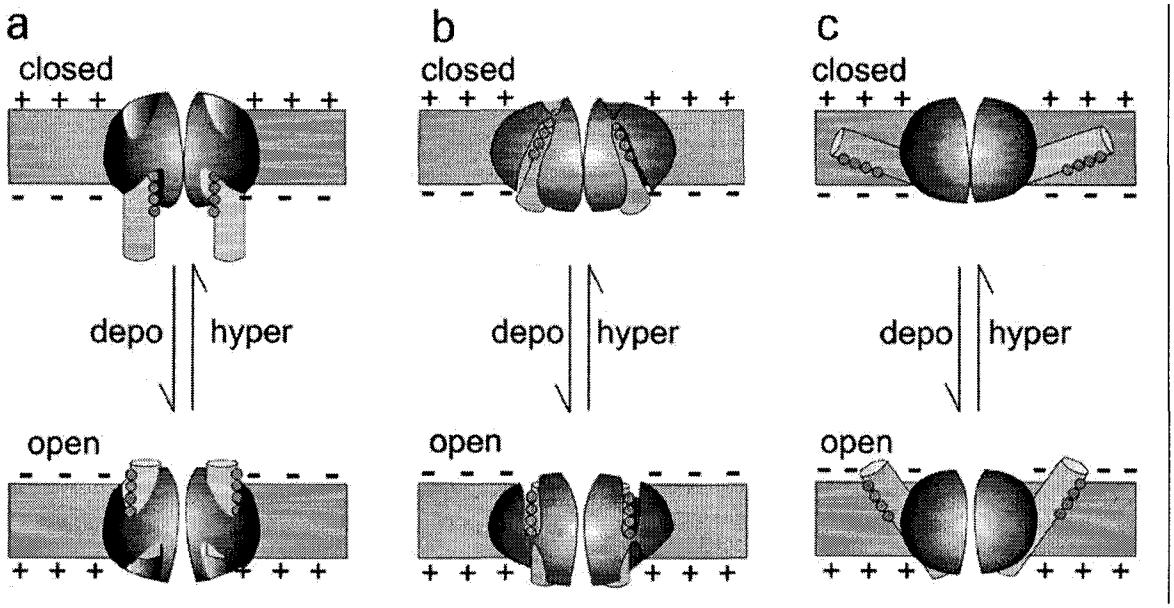


Fig. 5.4. Current models of Voltage-sensing mechanism.

Through MD simulations, there is a possibility to unveil the voltage-sensing mechanism of voltage gated ion channels and hence can contribute lot towards ion channel research.

MD simulation work to study the effects of ultra-short very high amplitude electric pulses on channel proteins as well as voltage gated ion channels are expected to reveal conformational changes, possible voltage-thresholds, and the changes in channel conduction through voltage-gating. Initial efforts have been done with alamethicin channel, but an in-depth study is required to understand the structure and function of ion channels.

### 5.3.2 Membrane Electro-fusion

"Membrane fusion is one of the most basic processes of life," said James McNew, assistant professor of biochemistry and cell biology at Rice University. "It begins at

fertilization and occurs billions of times a second in our bodies, and if it ever stops, we die."

Membrane fusion is mediated by few proteins. The main role of these proteins is to facilitate the fusion, rather than actively drive it. Experimentally, fusion between two membranes is a slow-process, but could become a fast-process if two membranes were very close to each other (126).

Fusion is believed to be caused by topological changes in lipid membrane arising from local fluctuations of the molecules. The initial bilayer destabilization leading to fusion is believed to result from either a high curvature binding defect or a hydrophobic defect -- that both lead to the appearance of lipid "stalks" e.g., the inverted micelle (127) and hemifusion – fusion (128) models. These models are shown in Fig. 5.5. The basic idea is that as two membrane surfaces come in close nano-proximity, the fluctuating lipids will drive away the water from the nano-space between the two adjacent membrane surfaces. Molecular re-arrangements to minimize total energy then result in fusion.

Studying this phenomena at the atomic level through MD simulations, would help answer the following important and critical questions:

(a). Can E-field-induced pores facilitate membrane fusion in cases when two membrane surfaces are in close nano-proximity ?

(b). Could external E-fields be made to alter fusion dynamics ? If so this might be of interest in the context of viruses (flu/HIV) fusing into molecules and proteins.

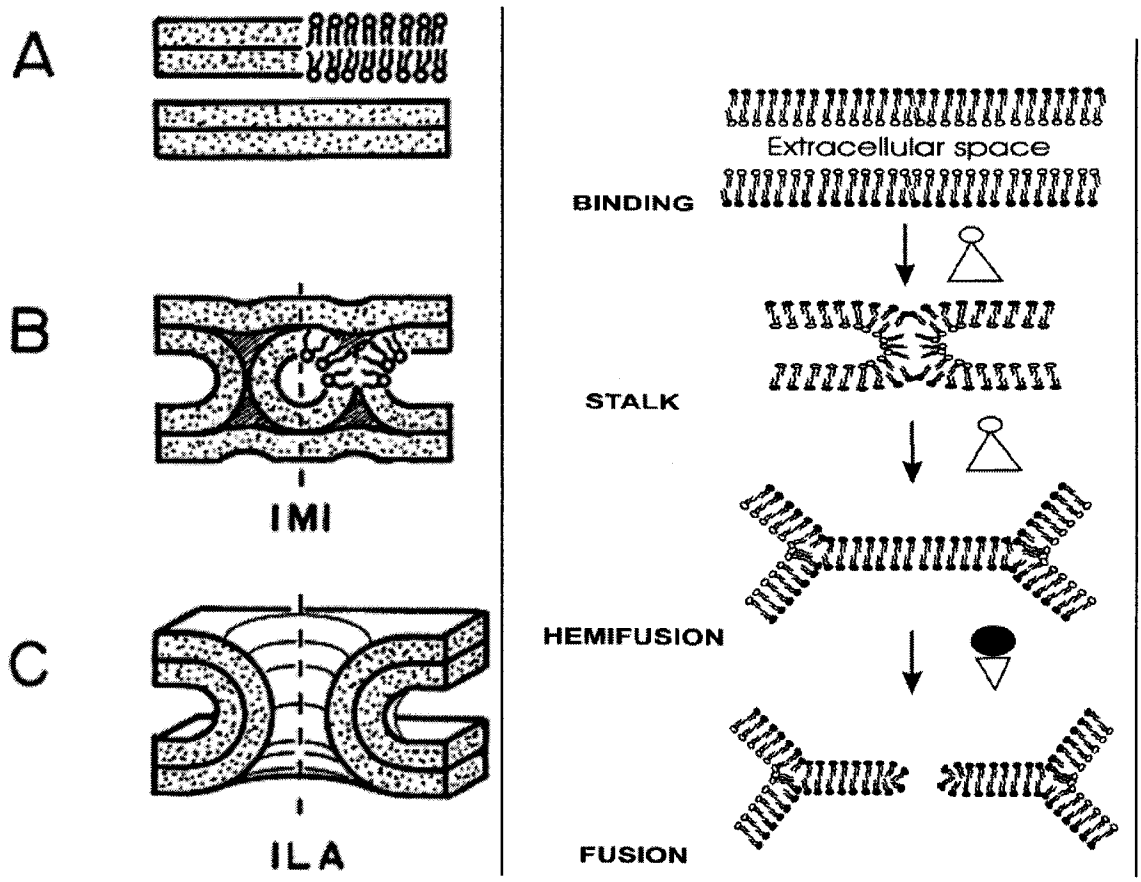


Fig. 5.5. Siegel model (left)- Inverted Micelle Intermediate (IMI) and Fusion Pores (ILA). Melikyan model (right)- Hemifusion intermediate to finally fusion.

### 5.3.3 Artifical "Chaperoning" of Denatured Proteins

Denaturation of proteins by high temperatures is one of the major causes of tissue death. The cause for denaturation is that the supra-physiological temperatures affect the protein leading to unfolding of its inner hydrophobic structure. Naturally chaperones are heat shock proteins that take care of denatured proteins by disaggregating the proteins and hence aid the damaged protein back to its native-folding structure. So, if the concentration of chaperones can be increased near the tissue wound, then there is a possibility of quicker wound healing.

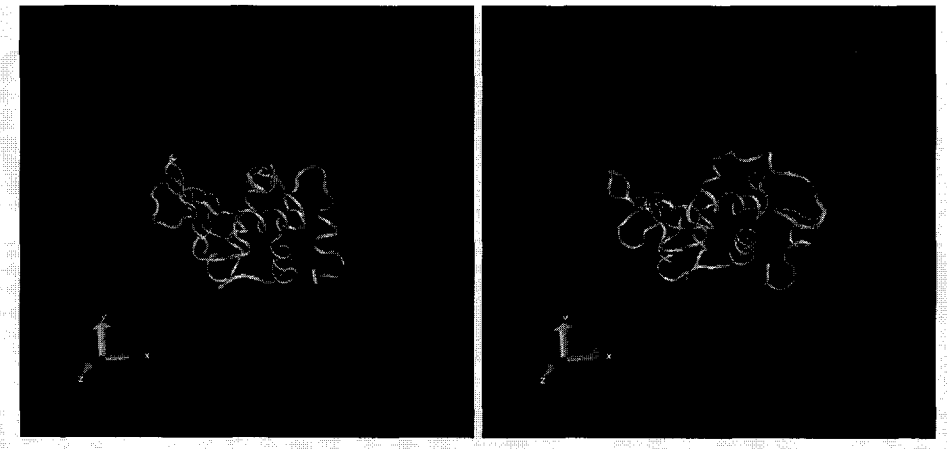

Fig. 5.6. Hen Egg White Lysozyme (HEWL), natural and denatured versions.

Recently, there have been experiments done to probe the injection of artificially induced synthetic polymers of polypropylene oxide-polyethylene oxide (PEO-PPO-PEO) near the damaged tissue. These surfactant polymers do the functioning of natural chaperones. These experimental results showed the ability of these polymers to prevent formation of stable aggregates of heat denatured hen egg lysozyme. This protein's structure along with the denatured version of this protein is shown in Fig. 5.6 above. Fig. 5.7 below shows one of this polymer near the denatured protein.

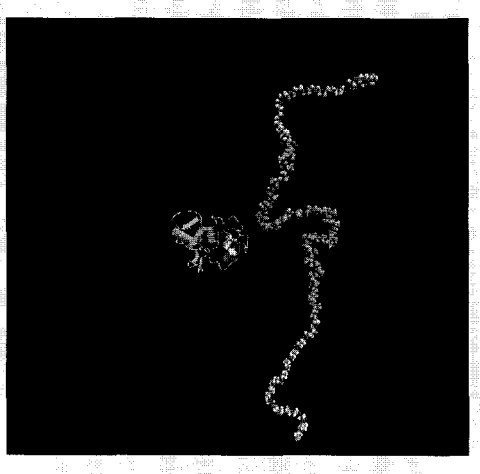

Fig. 5.7. PEO (cyan-red)-PPO (orange)-PEO surfactant placed near HEWL.

The hypothesis was that the synthetic polymers function in chaperoning the heat denatured lysozyme by reducing their aggregation. The actual molecular mechanism is not well understood and hence here we propose MD simulation to understand this mechanism in detail. Initial efforts were done in this area, but a detailed study is required to understand the exact mechanism of these surfactant polymers interactions with the egg lysozyme.

### 5.3.4 Pulsed Electric Field's on Mitochondria

Mitochondria is regarded as the power-house for biological cell. It has 2 membranes as shown in Fig. 5.8. Generally outer membrane can be easily permeated but the inner membrane is highly impermeable. Outer membrane has porins, which act as channels for the exchange of water molecules along with proteins upto 10k Daltons. On the other side, inner membrane is highly impermeable, as cardiolipin binds strongly to it. There are large number of studies to understand the structure and function of aquaporins (129). There have also been numerous studies on cardiolipin (130) to understand the binding properties.

One of the crucial factors for apoptosis is the release of *cytochrome C* from the inner mitochondrial membrane. *Cytochrome C* in general binds to cardiolipin in the inner membrane. Release of *cytochrome C* is shown to initiate by a 2-step process. In the first step, *cytochrome C* will be released from its binding to cardiolipin and in the next step, it will be extruded from outer mitochondrial membrane into cytosol. One other process that accompanies *cytochrome C* release is mitochondrial membrane depolarization (131). This is the general consensus about the release of *cytochrome c* and its role in apoptosis.

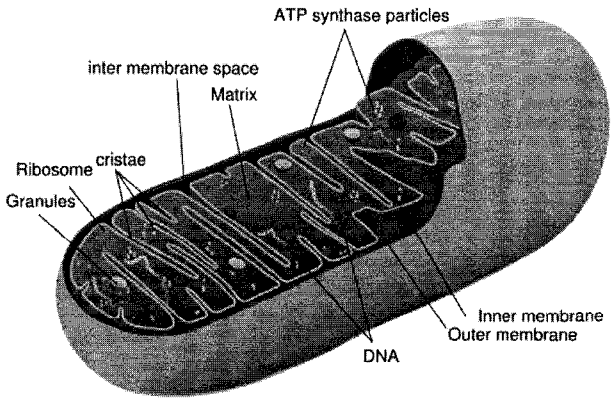


Fig. 5.8. Mitochondrial Structure (132).

The crystal structures of *cytochrome C* have recently been found and there were already simulations done on c*ytochrome C* regarding the structure and its function (132). There were also simulations done to understand *cardiolipin-cytochrome C* binding. Ultra-short PEF's have also shown to induce *cytochrome C* release. With this background motivation and with the computational resources availability, the MD simulation to show release of *cytochrome C* can lead to a major contribution to understand apoptosis caused by pulsed electric fields.

### 5.3.5 Kinetics of Electro-delivery of Bioactive Agents – Multiscale Modeling

Pulsed electric fields were found to increase the uptake of DNA into cells (4). There were molecular simulations done to show the uptake of plasmid DNA's into the cell (53). But, these simulations did not explain the kinetics of the DNA uptake and concentrated more on just showing the trajectory of plasmid DNA through the membrane. To understand the kinetics of electro-delivery of molecules, evaluation of their transport parameters is necessary. Recently, MD simulations were done to calculate the transport parameters of water through the membrane pores . Using the same technique

(MD simulation), there is scope to calculate the transport parameters (diffusion constant) of the bioactive agents of interest. These simulations (parameters of interest) coupled with continuum approaches (drift-diffusion, reaction-diffusion etc.) should explain the kinetics of drugs into the cell. Thus, it would be possible to perform a comprehensive macro-analyses that includes nanoscale physical details and spans a wide temporal range over several orders of magnitude. Fig. 5.9 shows the possible drug delivery into the cell upon the application of traditional electroporation pulses.

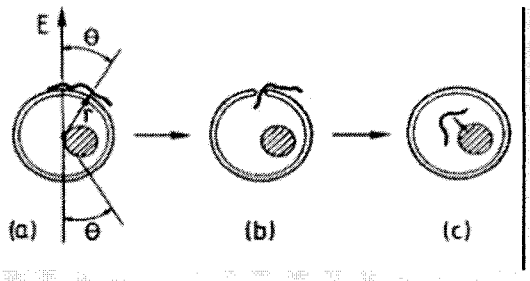


Fig. 5.9. Schematic of Drug delivery into cells (46).

# APPENDIX A

# TIME DOMAIN DIELECTRIC SPECTROSCOPY

## A.1 The Time Domain Spectroscopy Principle

In Time Domain Spectroscopy, a voltage pulse Vo(t) is sent down a coaxial line that is terminated with a dielectric material e.g., a cell suspension. As long as there is no heterogeneity in the transmission line, the pulse passes without any reflection. But if the pulse encounters any heterogeneity (cell suspension), a part of the pulse is reflected back R(t), while the remaining pulse passes through. Information about the heterogeneity can be found from the reflected pulse. This technique is employed to find the dielectric properties of the cell suspensions. A schematic of this principle is shown in Fig. A.1.

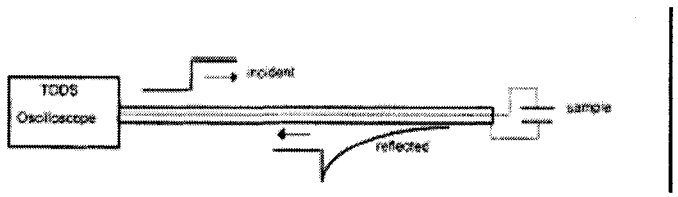


Fig. A.1. Incident and Reflected Pulse in TDDS (133).

The mathematics behind this theory is given below. The voltage pulse V(t) across the sample is :

$$V(t)=V_o(t)+R(t). \qquad \text{(A-1)}$$

The total current I(t) through the sample is then :

$$I(t)= 1/Z_o[V_o(t)-R(t)], \quad \text{(A-2)}$$

where $Z_o$ is the characteristic line impedance.

This total current is composed of the displacement current $I_D(t)$ and the low-frequency current $I_R(t)$ between the capacitor electrodes. The active resistance (r) of sample at low-frequency can be calculated by :

$$r = Lt\ t\rightarrow\infty\ V(t)/I(t) = Z_o\ Lt\ t\rightarrow\infty\ [V_o(t)+R(t)] / [V_o(t)-R(t)]. \quad \text{(A-3)}$$

The low frequency current ($I_R(t)$) is given by :

$$I_R(t) = V(t)/r = V_o(t)+R(t) / Z_o\ Lt\ t\rightarrow\infty\ [V_o(t)-R(t)] / [V_o(t)+R(t)]. \quad \text{(A-4)}$$

Then, the displacement current ($I_D(t)$) is given by:

$$I_D(t) =1/Z_o\ \{\{\ [V_o(t)-R(t)]\}-\{\ [V_o(t)+R(t)]\ Lt\ t\rightarrow\infty\ [V_o(t)-R(t)] / [V_o(t)+R(t)]\}\}. \quad \text{(A-5)}$$

Also, low frequency conductivity ($\sigma$) is :

$$\sigma = (\varepsilon_o/Z_oC_o)Lt\ t\rightarrow\infty\ [V_o(t)-R(t)] / [V_o(t)+R(t)], \quad \text{(A-6)}$$

where $\varepsilon_o$ = 8.85e-12 F/m, and $C_o$ is the electric capacitance of the coaxial sample cell terminated in the transmission line. $C_o$ is found independently from the geometry of the sample cell. Using I(t), V(t) or their complex Laplace transforms i(ω), v(ω), one can get the relations of the dielectric parameters.

The sample admittance (Y(ω)) for the sample cell terminated in the line is then given by:

$$Y(\omega) = i(\omega) / v(\omega). \quad \text{(A-7)}$$

The sample permittivity ($\varepsilon(\omega)$) can be found from the sample admittance as follows:

$$\varepsilon(\omega) = Y(\omega)/(j\omega C_o). \quad \text{(A-8)}$$

where j is the imaginary unit.

As a special case, if one takes into account the definite physical length of the sample and the multiple reflections from the air-dielectric and dielectric-air interfaces, the permittivity ($\varepsilon^*(\omega)$) can be written as:

$$\varepsilon^*(\omega) = c / (j\omega\gamma d)\, Y(\omega)\, X\, \text{Cotangent}(X)\,, \quad \text{(A-9)}$$

where "d" is the effective length of the inner conductor, "c" is the velocity of light, "$\gamma$" is the ratio between the capacitance per unit length of the cell to that of the matched coaxial cable, and

$$X = (\omega d/c)\, \text{sqrt}(\varepsilon^*(\omega))\,. \quad \text{(A-10)}$$

## A.2 Measurements : Drawbacks and Methods for Overcoming Problems

Generally biological systems are conductive. Obtaining low-frequency dielectric parameters for these systems involves correcting for the conductivity. If the dc conductivity is relatively small, then its values can be obtained from eqn. (A-6) at low frequencies. This provides the d.c. value necessary in the evaluation of the loss factor of complex permittivity. On the other hand, if the dc conductivity is significant, it should be corrected before calculating the dielectric parameters. A high dc value can result from the accumulation of charges on the electrodes at low frequency that forms electrical double layers. This effect is also known as parasitic capacitance.

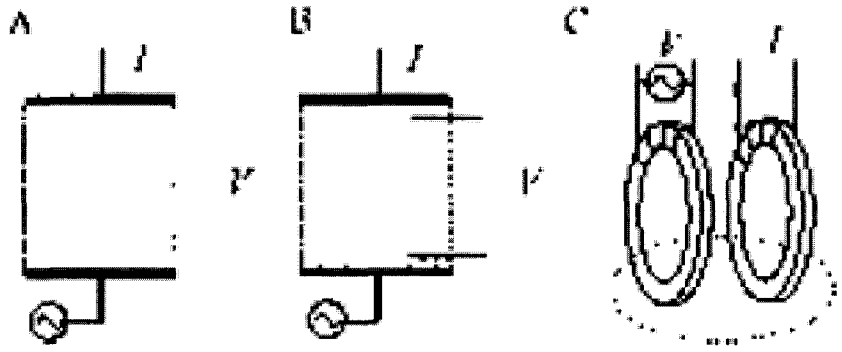

Fig. A.2. Measurement techniques A) Current electrode, B) Four-Electrode, and C) Electromagnetic Induction Method.

Various approaches have been used to correct for electrode polarization. These include four-electrode methods (134) and the electromagnetic induction method (135). In the four-electrode method, electrodes for current supply are different from the voltage electrodes. In the electromagnetic induction method, there are no electrodes and hence there is no electrode polarization. The schematics of the above methods are shown in Fig. A.2. The details of electrode polarization depend microscopically on the topography of the electrode surfaces as well as the area and chemistry of the surface, and the chemical interaction of the sample with the electrode surface. The next step after correcting for electrode polarization is to fit the experimental data to the "reliable" mathematical models and obtaining the dielectric parameters. Various models have been proposed and they are outlined in next section.

## A.3 Mathematical Models

Depending on the concentration of the dispersed particles, the shape of the particles and the conductivity of the media (or dispersed particles), two important mixture

models i.e., Maxwell-Wagner and Hanai have been used extensively in the past. These are briefly discussed below.

### A.3.1 The Maxwell-Wagner (M-W) Mixture Model

Generally for low concentrations of cells in a suspension, the M-W mixture model (136) is used. The M-W model describes the suspension dielectric parameters in terms of the dielectric parameters of the supernatant (or buffer) and the cell. It is assumed that all the cells dispersed in the media are same with respect to size, shape and properties.

$$\varepsilon^*_{mix}(\omega) = \varepsilon^*_{sup}(\omega)*(2\varepsilon^*_{sup}(\omega)+\varepsilon^*_c(\omega)-2p(2\varepsilon^*_{sup}(\omega)-\varepsilon^*_c(\omega))/$$
$$[2\varepsilon^*_{sup}(\omega)+\varepsilon^*_c(\omega)+p(2\varepsilon^*_{sup}(\omega)-\varepsilon^*_c(\omega)] \quad , \qquad \text{(A-11)}$$

where $\varepsilon^*_{mix}$ is the complex permittivity of the mixture, $\varepsilon^*_{sup}$ is the complex permittivity of the supernatant, $\varepsilon^*_c$ is the complex permittivity of the cell and p is the volume fraction.

### A.3.2 The Hanai Mixture Model

Maxwell-Wagner mixture model is employed for cell suspensions having less than few percent (approx. 8 %) of cells. For suspensions with high concentrations of cells, Hanai mixture model is generally employed. The Hanai mixture model (137) describes the suspension dielectric parameters in terms of the dielectric parameters of the supernatant (or buffer) and the cell (similar to the Maxwell-Wagner Model). The effective permittivity is given by:

$$\{(\varepsilon^*_{mix}(\omega)-\varepsilon^*_c(\omega))/(\varepsilon^*_{sup}(\omega)-\varepsilon^*_c(\omega))\}*\{(\varepsilon^*_{sup}/\varepsilon^*_{mix}(\omega))^{0.333}\}= 1\text{-}p. \qquad \text{(A-12)}$$

where $\varepsilon^*_{mix}$ is the complex permittivity of the mixture, $\varepsilon^*_{sup}$ is the complex permittivity of the supernatant, $\varepsilon^*_c$ is the complex permittivity of the cell and p is the volume fraction.

## A.4 Shell Models

The two above mixture models help explain and quantify the average dielectric properties of the cell in the suspension. The shell models require one to ascertain the dielectric parameters of individual phases of cells, i.e., the $\varepsilon^*_c$ values in eqn. (A-12). The individual cell permittivities can be computed on the basis of the shell-models, as described below. In the single shell model, the cell is considered to be a sphere with a thin insulating envelope enclosing conductive cytoplasm. While in the double shell, a smaller sphere representing the nucleus, is incorporated within a big sphere. Every phase is supposed to have no dielectric losses and the complex permittivity is then written as :

$$\varepsilon^*_i(\omega) = \varepsilon_i(\omega) - j\sigma_i(\omega)/\omega\varepsilon_o \,, \qquad \text{(A-13)}$$

where i represents every phase of the heterogeneous system i.e., cell membrane, and cytoplasm for single shell and cell membrane, cytoplasm, nuclear membrane and nucleoplasm for double shell models, $\varepsilon$ represents the relative permittivity, $\sigma$ represents the conductivity, $\omega$ represents the angular frequency and $\varepsilon_o$ represents the vacuum permittivity. These models are shown in Fig. A.3.

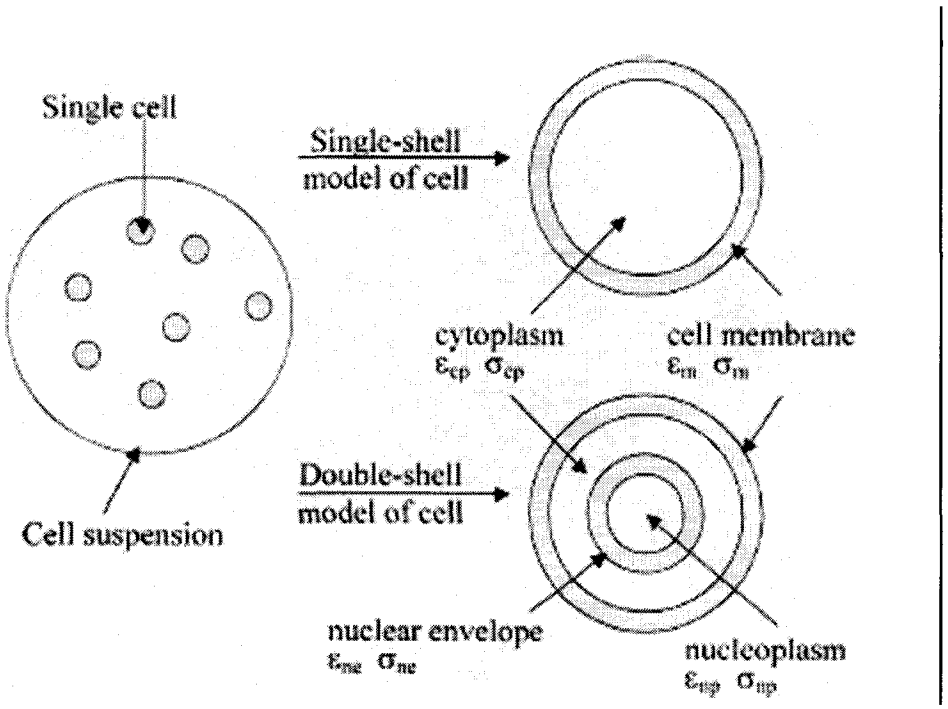


Fig. A.3. Single and Double Shell Models of Cell (133).

Apart from single and double shell models, plant protoplasts can be very well fitted to a double shell model along with vesicles inside it. This model is shown in Fig. A.4. The same theory can be extended to construct multi-shell models for representing vesicle like structures such as mitochondria, endoplasmic reticulum (ER), or other intracellular structures. In such a case, e.g., inclusion of the mitochondria (or the ER), one more phase for mitochondria needs to be added to eqn. (A-12). The calculation of these phase dielectric properties from Maxwell-Wagner mixture model is given below.

$$\varepsilon^*_c = \varepsilon^*_m \{2(1-v_1)+(1+2v_1)E_1\}/\{(2+v_1)+(1-v_1)E_1\} \ , \qquad \text{(A-14)}$$

where the geometrical parameter $v_1$ is given by $(1-(d/R_c))^3$ .

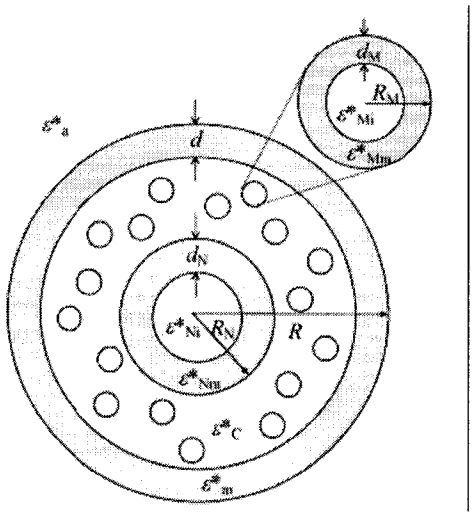

Fig. A.4. Double shell model with vesicles (138).

In single shell model, $E_1$ is given by :

$$E_1 = \varepsilon^*_{cp}/\varepsilon^*_m. \qquad \text{(A-15)}$$

In double shell model with and without vesicles, $E_1$ is given by :

$$E_1 = (\varepsilon^*_{cp}/\varepsilon^*_m)\{\, 2(1-v_2)+(1+2v_2)E_2\}/\{(2+v_2)+(1-v_2)E_2\}\ , \qquad \text{(A-16)}$$

where the geometrical parameter $v_2$ is given by $(R_n/(R_c-d_m))^3$, $E_2$ is given by :

$$E_2 = (\varepsilon^*_{ne}/\varepsilon^*_{cp})\{\, 2(1-v_3)+(1+2v_3)E_3\}/\{(2+v_3)+(1-v_3)E_3\}\ , \qquad \text{(A-17)}$$

where the geometrical parameter $v_3$ is given by $(1-(d_n/R_n))^3$.

In double shell model without vesicles, E3 is given by :

$$E_3 = \varepsilon^*_{np}/\varepsilon^*_{ne} \ . \qquad \text{(A-18)}$$

The same theory is followed for double shell model with vesicles and is not outlined here, but can be found elsewhere (138).

For all these models, the specific capacitance of the cell membrane per unit area can be calculated directly from :

$$C_m = 1.5\varepsilon_o\varepsilon_{mix}(low)/(R_c*(1-(1-p)^{1.5})) \ . \qquad \text{(A-19)}$$

## A.5 Results

Some of the results on the TDDS experiments on Jurkat cells are summarized in Table. A-1. A detailed explanation of the experiment protocols used for this work can be found elsewhere (139).

Table. A.1. TDDS experiments on Jurkat cells and results obtained from double shell model.

| Parameter / description | Name | Value |
|---|---|---|
| Radius of cell (fixed) | $R_c$ | 5.12e-6 m |
| Thickness of outer membrane (fixed) | $d_m$ | 7e-9 m |
| Radius of nucleus (fixed) | $R_n$ | $Rc*(0.8)^{1/3}$ m |
| Thickness of Nuclear envelope (fixed) | $d_n$ | 40e-9 m |
| Permittivity of Cytoplasm (fixed) | $e_{cp}$ | 60 |
| Permittivity of Nucleoplasm (fixed) | $e_{np}$ | 120 |
| Conductivity of cytoplasm | $k_{cp}$ | 0.1 S/m |
| Conductivity of nucleoplasm | $k_{np}$ | 0.2 S/m |
| Conductivity of cell membrane | $k_m$ | 6.4e-6 S/m |
| Conductivity of nuclear membrane | $k_n$ | 4.3e-3 S/m |
| Permittivity of Plasma Membrane | $e_m$ | 7.1 |
| Permittivity of Nuclear Membrane | $e_n$ | 22.6 |
| Permittivity of Supernatant | $e_{susp}$ | 68 |
| Conductivity of Supernatant | $k_{susp}$ | 0.1 S/m |

# APPENDIX B

# TRANSMEMBRANE POTENTIAL

## B.1 Introduction

The charging time constant for the outer membrane (plasma membrane) is a measure of the time during which the cell interior is exposed to the applied pulse. This can be stated equivalently as the outer membrane becomes increasingly transparent for oscillating electric fields with frequencies higher than the inverse time constant of outer membrane. This is known as Schwan's theory of oscillating electric fields. These can be calculated either analytically or using numerical methods. The next sections are devoted to describe transmembrane potentials as a function of electric field, cell diameter and other electrical parameters both analytically and numerically.

## B.2 Analytical Model

A biological cell can be considered spherical cell with another small compartment called nucleus. This is shown in Fig. B.1.

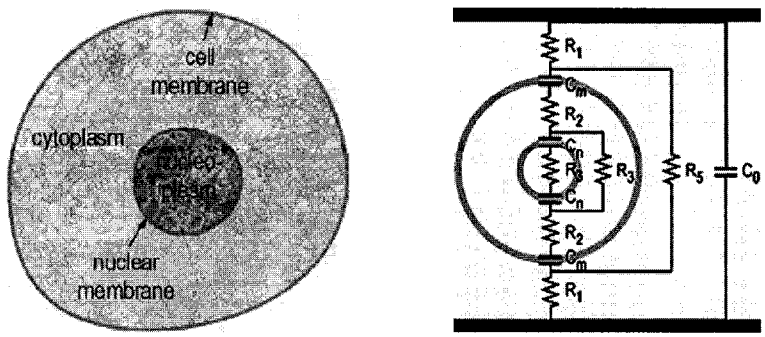


Fig. B.1. Cell structure and its equivalent electrical model.

The diameter of the cell is D, that of the organelle (here nucleus) is d, with d<<D. The organelle and cell are surrounded by cell walls or membranes. They are also called outer membrane (plasma membrane) and the inner membrane (nuclear membrane). The membranes are characterized by their specific capacitance as the conductivity of these membranes is very low (of order 1e-6 S/m), while the interior and exterior of the cell along with the interior of the organelle are characterized by their conductivity. When a step electric field is applied, the plasma membrane is charged with time constant given by Cole (140):

$$\tau_c = [\ (1+2V/1-V)\ \rho_1/2 + \rho_2\ ]\ C_m D/2, \qquad \text{(B-1)}$$

where V is the volume fraction of the cells, $\rho_1$ is the resistivity of the suspending medicum, $\rho_2$ the resistivity of the cytoplasma, $C_m$ the specific capacitance of the membrane.

For an applied electric field, the voltage ($V_{cell}$) across the cell is given by:

$$V_{cell} = f\ E\ D, \qquad \text{(B-2)}$$

where f is a factor equal to 1.5 for spherical cells.

The potential difference ($\Delta V_c$) across the plasma membrane is given by

$$\Delta V_c = f\ E\ (D/2)\ \cos\theta\ (1-\exp(-t/\ \tau_c)), \qquad \text{(B-3)}$$

where $\theta$ is taken as the angle with reference to application of electric fields.

It can be easily seen that the effect of this electric field will be higher at poles for $\theta = 0$ and $\pi$.

From eqn. (B-2) and eqn. (B-3), the voltage across the interior of the cell can be calculated as

$$V_{int}\ (t, \theta) = V_{cell} - 2\Delta V_c = f\ E\ D - f\ E\ D\ \cos\theta\ (1-\exp(-t/\ \tau_c)) = f\ E\ D\ \cos\theta\ \exp(-t/\ \tau_c), \qquad \text{(B-4)}$$

and along polar axis, it will be:

$$V_{int}(t) = V_{cell} - 2\Delta V_c = f\,E\,D - f\,E\,D\cos\theta\,(1-\exp(-t/\tau_c)) = f\,E\,D\exp(-t/\tau_c)\,. \qquad \text{(B-5)}$$

Assuming that the electric field along the polar axis is uniform,

$$E_{int}(t) = f\,E\exp(-t/\tau_c)\,. \qquad \text{(B-6)}$$

Treating the organelle in the similar manner to that of the cell, as the basic structure resembles one another, we get an expression for the voltage across the organelle and it is shown by:

$$V_{organelle}(t) = f^2\,E\,d\exp(-t/\tau_c), \qquad \text{(B-7)}$$

Again using the similarity of organelle to that of the cell, the potential difference across the interior of the inner organelle (here nucleus) can be found to be equal to:

$$\Delta V_o = f^2\,E\,(d/2)\,(\tau_c/(\tau_c - \tau_o))\,(\exp(-t/\tau_c) - \exp(-t/\tau_o))\,, \qquad \text{(B-8)}$$

where $\tau_o$ is the charging time constant for the organelle membrane.

In order to have an idea about the amplitudes of these potentials, a plot has been shown in Fig. B.2. This is calculated with the following cell parameters. D = 10μm, d = 2μm and f=1.5 The specific capacitance is taken to be equal to 1μF/m$^2$ while the resitivities are taken to be equal for cytoplasma, content of inner organelle (here nucleoplasma) and the outside of the cell, which is 100Ω.

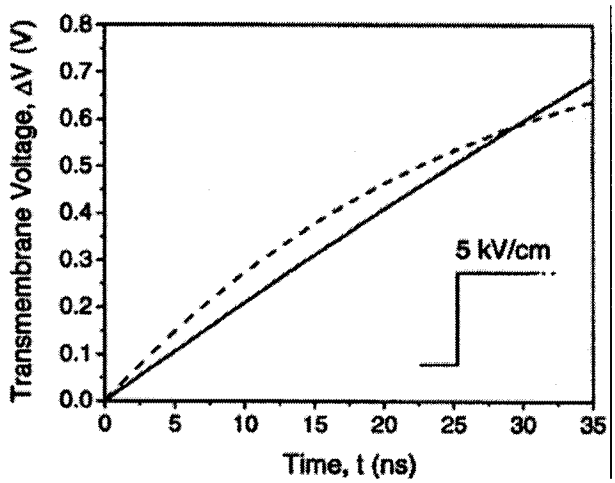


Fig. B.2. Analytical calculations of transmembrane potentials generated across outer and inner membranes (12).

From the Fig. B.2, it is clear that the transmembrane potential generated across inner organelle membrane is greater than that of the cell outer membrane, which supports the hypothesis that the short pulses cannot "see" plasma membrane and can directly interact with the cell interior.

## B.3 Numerical model

The analytical model gives a very good basic understanding of the schwan's theory of oscillating electric fields. The numerical methods of cellular response to ultra-short pulses are required for quantitative predictions of many phenomena seen in experiments. Another advantage of these numerical calculations is the shape of the biological cell is irrelevant. There were 2 such numerical models. One is developed by Weaver's group (141) at MIT while the other is developed by our group at ODU. We used a scheme in which we treated the cell as a distributed circuit. The current continuity equation coupled with the Smoluchowski equation for pore development is considered. Here a brief

description of this numerical model with transmembrane potential calculations is provided.

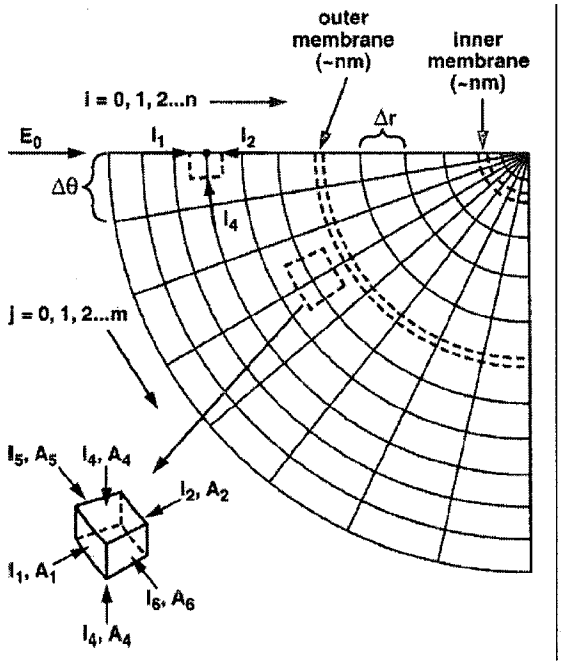


Fig. B.3. Quarter of the cell considered for calculations (142).

In this model, the entire cell volume is broken up into finite segments, and each segment is represented by a parallel RC combination to account for the current flow and charging effects. Using azimuthal symmetry, the three dimensional structure of call can be mapped into the r and " coordinates of a spherical system. Based on the symmetry, only a quarter of the computational region was considered. For simplicity, the membranes were taken as integral unit i.e., this region is not discretized further, which seems reasonable if a proper value of dielectric permittivity and conductivity is given to these units. This is shown in Fig. B.3 above.

The pore growth and size evolution are assumed to depend on continuum Smoluchowski theory, with the following equation for the pore density distribution n(r,t):

$$\partial n(r,t)/dt - \{D/[k_B T]\}[\partial\{n(r,t)dE(r)/\partial r\}/\partial r] - D[\partial^2 n(r,t)/\partial r^2] = S(r) \ , \qquad \text{(B-9)}$$

where S(r) is the source term (here, pore formation), D is the diffusion constant of the pore (lipid molecules enclosing pore), pore radius r, Electric field E, Boltzmann constant $k_B$ and temperature T.

For each element, the current continuity equation is given by:

$$\text{grad.}\ (J+\partial D/\partial t) = 0, \qquad \text{(B-10)}$$

where J is the current density and D is the electric displacement vector. For a detailed description of this model, the reader is directed to Joshi et. al., (142). The transmembrane potentials generated by this scheme are plotted in Fig. B.4 below. The time constant of the plasma membrane calculated from Cole's equation 1 is 75ns for specific cell and media parameters. The results are shown for 2 cases. In the first case, a pulse of 280ns width and 5KV/cm amplitude is taken. Since, the pulse duration is more than charging time constant of outer membrane, the effect on outer membrane is more. Initially the effect on inner membrane is more, as the frequency of the pulse initially (<75ns) is greater than the inverse charging time constant of plasma membrane. But once the pulse duration is more than 75ns, the outer membrane charges more rapidly compared to the inner membrane.

In the second case, a trapezoidal pulse with rise and fall times equal to 1.5ns and total duration of 11ns is applied. Since the duration of the pulse is much smaller than the charging time constant of the plasma membrane, the inner membrane charges more compared to the outer membrane. A detailed explanation of this scheme can be found elsewhere (142).

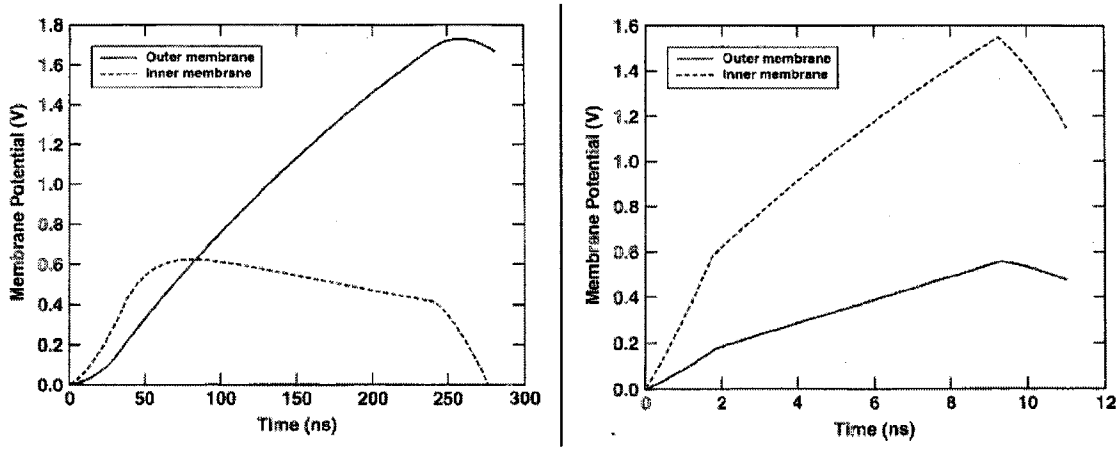


Fig. B.4. Transmembrane potential calculations using Current continuity equations for distributed circuit model coupled to the Smoluchowski equation for pore development (142).

Lately, many groups have started working on the numerical models to calculate transmembrane potentials generated across the cells upon the application of pulsed electric fields (143, 144). There has also been work contributed towards the transmembrane potential generation of irregularly shaped cells i.e., oblate and elliptic spheres (145). Even though the models considered here are simple, they match very well with the experimental results. Thus, numerical simulations provide a great tool for the experimentalists to validate their results.

# REFERENCES LIST


1. Polk, C. & Postow, E. (1995) *Handbook of Biological Effects of Electromagnetic Fields* (CRC Press, Boca Raton).

2. Pakhomov, A. G., Akyel, Y., Pakhomova, O. N., Stuck, B. E., & Murphy, M. R. (1998) *Bioelectromagnetics* **19**, 393-413.

3. Neumann, E., Sowers, A. E., & Jordan, C. A. (1989) *Electroporation and Electrofusion in Cell Biology* (Plenum Press, New York).

4. Neumann, E., Schaefer-Ridder, M., Wang, Y., & Hofschneider, P. H. (1982) *EMBO J.* **1**, 841-845.

5. Schoenbach, K. H., Beebe, S. J., & Buescher, E. S. (2001) *Bioelectromagnetics* **22**, 440-448.

6. Nuccitelli, R., Pliquett, U., Chen, X., Ford, W., James, S. R., Beebe, S. J., Kolb, J. F., & Schoenbach, K. H. (2006) *Biochem. Biophys. Res. Commun.* **343**, 351-360.

7. Rahman, A. & Stillinger, F. H. (1971) *J. Chem. Phys.* **55**, 3336-3359.

8. Beebe, S. J., Fox, P. M., Rec, L. J., Willis, E. L., & Schoenbach, K. H. (2003) *FASEB J.* **17**, 1493-1495.

9. Vernier, P. T., Sun, Y., Marcu, L., Craft, C. M., & Gundersen, M. A. (2004) *Biophys. J.* **86**, 4040-4048.

10. Frey, W., White, J. A., Price, R. O., Blackmore, P. F., Joshi, R. P., Nuccitelli, R., Beebe, S. J., Schoenbach, K. H., & Kolb, J. F. (2006) *Biophys. J.* **90**, 3608-3615.

11. Beebe, S. J., Blackmore, P. F., White, J., Joshi, R. P., & Schoenbach, K. H. (2004) *Physiol Meas.* **25**, 1077-1093.

12. Schoenbach, K. H., Joshi, R. P., Kolb, J. F., Chen, N., Stacey, M., Blackmore, P. F., & Buescher, E. S. (2004) Proceedings of IEEE. **92,** 1122-1137.

13. van Gunsteren, W. F. & Berendsen, H. J. (1982) *Biochem. Soc. Trans.* **10**, 301-305.

14. Egberts, E., Marrink, S. J., & Berendsen, H. J. (1994) *Eur. Biophys. J.* **22**, 423-436.

15. Venable, R. M., Zhang, Y., Hardy, B. J., & Pastor, R. W. (1993) *Science* **262**, 223-226.

16. Patargias, G., Bond, P. J., Deol, S. S., & Sansom, M. S. (2005) *J. Phys. Chem. B Condens. Matter Mater. Surf. Interfaces. Biophys.* **109**, 575-582.

17. Schoenbach, K. H., Peterkin, F. E., Alden, R. W., & Beebe, S. J. (1997) IEEE trans. on Plas. Sci. **25**, 284-292.

18. Durell, S. R. & Guy, H. R. (1992) *Biophys. J.* **62**, 238-247.

19. Zimmermann, U. (1996) in *CRC* Boca Raton.

20. Amr Abou-Ghazala & Karl H.Schoenbach (2000) IEEE trans. on Plas. Sci. **28**, 115-121.

21. Piccotti, L., Marchetti, C., Migliorati, G., Roberti, R., & Corazzi, L. (2002) *J. Biol. Chem.* **277**, 12075-12081.

22. Piccotti, L., Buratta, M., Giannini, S., Gresele, P., Roberti, R., & Corazzi, L. (2004) *J. Membr. Biol.* **198**, 43-53.

23. Guidotti, G. (1972) *Annu. Rev. Biochem.* **41**, 731-752.

24. Pearson, R. H. & Pascher, I. (1979) *Nature* **281**, 499-501.

25. Pascher, I., Sundell, S., Harlos, K., & Eibl, H. (1987) *Biochim. Biophys. Acta* **896**, 77-88.

26. Feller, S. E., Yin, D., Pastor, R. W., & MacKerell, A. D., Jr. (1997) *Biophys. J.* **73**, 2269-2279.

27. van Gunsteren, W. F. & Berendsen, H. J. (1984) *J. Mol. Biol.* **176**, 559-564.

28. Weiner, S. J., Kollman, P. A., Case, D. A., Singh, U. C., Ghio, C., Alagona, G., Profeta, S., & Weiner, P. (1984) J. Amer. Chem. Soc. **106**, 765-784.

29. Brooks, B. R., Bruccoleri, R. E., Olafson, B. D., States, D. J., Swaminathan, S., & Karplus, M. (1983) J. Comp. Chem. **4**, 187-217.

30. Hermans, J., Berendsen, H. J., van Gunsteren, W. F., & Postma, J. P. (1984) Biopolymers. **23**, 1513-1518.

31. Singer, S. J. & Nicolson, G. L. (1972) *Science* **175**, 720-731.

32. Feller, S. E. & Pastor, R. W. (1996) *Biophys. J.* **71**, 1350-1355.

33. Levitt, M. (2001) *Nat. Struct. Biol.* **8**, 392-393.

34. Joshi, R. P., Sridhara, V., & Schoenbach, K. H. (2006) *Biochem. Biophys. Res. Commun.* **348**, 643-648.

35. Pastor, R. W., Venable, R. M., & Feller, S. E. (2002) *Acc. Chem. Res.* **35**, 438-446.

36. Pandit, S. A., Bostick, D., & Berkowitz, M. L. (2003) *Biophys. J.* **84**, 3743-3750.

37. Pandit, S. A., Bostick, D., & Berkowitz, M. L. (2003) *Biophys. J.* **85**, 3120-3131.

38. Tieleman, D. P., Forrest, L. R., Sansom, M. S., & Berendsen, H. J. (1998) *Biochemistry* **37**, 17554-17561.

39. Sansom, M. S., Tieleman, D. P., Forrest, L. R., & Berendsen, H. J. (1998) *Biochem. Soc. Trans.* **26**, 438-443.

40. Shrivastava, I. H., Durell, S. R., & Guy, H. R. (2004) *Biophys. J.* **87**, 2255-2270.

41. Jiang, Y., Lee, A., Chen, J., Ruta, V., Cadene, M., Chait, B. T., & MacKinnon, R. (2003) *Nature* **423**, 33-41.

42. Tieleman, D. P. (2004) *BMC. Biochem.* **5**, 10-21.

43. Hu, Q., Viswanadham, S., Joshi, R. P., Schoenbach, K. H., Beebe, S. J., & Blackmore, P. F. (2005) *Phys. Rev. E. Stat. Nonlin. Soft. Matter Phys.* **71**, 031914.

44. Tekle, E., Astumian, R. D., Friauf, W. A., & Chock, P. B. (2001) *Biophys. J.* **81**, 960-968.

45. Pliquett, U., Schmeer, M., Seipp, T., & Neumann, E. (2002) Intern. Fed. Med. Biol. Engin. Proc. **3**, 98-99.

46. Neumann, E., Toensing, K., Kakorin, S., Budde, P., & Frey, J. (1998) *Biophys. J.* **74**, 98-108.

47. Tsong, T. Y. (1991) *Biophys. J.* **60**, 297-306.

48. Busath, D., Henderson, D., & Sokolowski, S. (2004) J. Phys.: Condens. Matter **16**, S2193-S2201.

49. Tieleman, D. P. (2006) *Clin. Exp. Pharmacol. Physiol* **33**, 893-903.

50. Chung, S. H. & Kuyucak, S. (2001) *Clin. Exp. Pharmacol. Physiol* **28**, 89-94.

51. Vasilkoski, Z., Esser, A. T., Gowrishankar, T. R., & Weaver, J. C. (2006) *Phys. Rev. E. Stat. Nonlin. Soft. Matter Phys.* **74**, 021904.

52. Sukharev, S. I., Klenchin, V. A., Serov, S. M., Chernomordik, L. V., & Chizmadzhev, Y. (1992) *Biophys. J.* **63**, 1320-1327.

53. Tarek, M. (2005) *Biophys. J.* **88**, 4045-4053.

54. Hall, E. H., Schoenbach, K. H., & Beebe, S. J. (2005) *DNA Cell Biol.* **24**, 283-291.

55. Fink, H. W. & Schonenberger, C. (1999) *Nature* **398**, 407-410.

56. Vernier, P. T., Sun, Y., Marcu, L., Salemi, S., Craft, C. M., & Gundersen, M. A. (2003) *Biochem. Biophys. Res. Commun.* **310**, 286-295.

57. Wilczynska, Z., Happle, K., Muller-Taubenberger, A., Schlatterer, C., Malchow, D., & Fisher, P. R. (2005) *Eukaryot. Cell* **4**, 1513-1525.

58. E.Stephen Buescher, Rachel R.Smith, & Karl H.Schoenbach (2004) IEEE trans. on Plas. Sci. **32**, 1563-1572.

59. Bezanilla, F. (2005) *IEEE Trans. Nanobioscience.* **4**, 34-48.

60. Schwan, H. P. (1957) *Adv. Biol. Med. Phys.* **5**, 147-209.

61. Asami, K. & Yonezawa, T. (1995) *Biochim. Biophys. Acta* **1245**, 317-324.

62. Polevaya, Y., Ermolina, I., Schlesinger, M., Ginzburg, B. Z., & Feldman, Y. (1999) *Biochim. Biophys. Acta* **1419**, 257-271.

63. Schwan, H. P. & Onaral, B. (1985) *Med. Biol. Eng Comput.* **23**, 28-32.

64. Fricke, H. (1953) *Nature* **172**, 731-732.

65. Ermolina, I., Morgan, H., Green, N. G., Milner, J. J., & Feldman, Y. (2003) *Biochim. Biophys. Acta* **1622**, 57-63.

66. Asami, K. (2006) *Phys. Rev. E. Stat. Nonlin. Soft. Matter Phys.* **73**, 052903.

67. Jerzy Luczka, Ryszard Rudnicki, & Peter Hanggi (2005) *Physica A* **351**, 68.

68. Chung, S. H., Allen, T. W., & Kuyucak, S. (2002) *Biophys. J.* **83**, 263-277.

69. Elhebil, F. & Premilat, S. (1992) *Biophys. Chem.* **42**, 195-200.

70. Alder, B. J. & Wainwright, T. E. (1957) *J. Chem. Phys.* **27**, 1208-1209.

71. McCammon, J. A. & Karplus, M. (1977) *Nature* **268**, 765-766.

72. Egberts, E. & Berendsen, H. J. (1988) *J. Chem. Phys.* **98**, 1712-1720.

73. Edholm, O., Berger, O., & Jahnig, F. (1995) *J. Mol. Biol.* **250**, 94-111.

74. Duan, Y. & Kollman, P. A. (1998) *Science* **282**, 740-744.

75. van der Spoel, D., Lindahl, E., Hess, B., van Buuren, A. R., Apol, E., Meulenhoff, P. J., Tieleman, D. P., Sijbers, A. L. T. M., Feenstra, K. A., Drunen, R. V. *et al.* (2004) (University of Groningen, The Netherlands).

76. Berendsen, H. J., Postma, J. P., DiNola, A., & Haak, J. R. (1984) *J. Chem. Phys.* **81**, 3684-3690.

77. Ryckaert, J. P., Ciccotti, G., & Berendsen, H. J. (1977) *J. Comp. Phys.* **23**, 327-341.

78. Yoneya, M., Berendsen, H. J., & Hirasawa, K. (1994) *Molecular Simulations* **13**, 395-405.

79. Hess, B., Bekker, H., & Berendsen, H. J. (1997) *J. Comp. Chem.* **18**, 1472.

80. Van Der, S. D., Lindahl, E., Hess, B., Groenhof, G., Mark, A. E., & Berendsen, H. J. (2005) *J. Comput. Chem.* **26**, 1701-1718.

81. van Gunsteren, W. F. & Berendsen, H. J. (1988) *Molecular Simulations* **1**, 173-185.

82. Zwanzig, R. W. (1961) Lectures in Theoretical Physics, New York.

83. Humphrey, W. F., Dalke, A., & Schulten, K. (1996) *J. Mol. Graphics.* **14**, 33-38.

84. Bootman, M. D., Berridge, M. J., & Lipp, P. (1997) *Cell* **91**, 367-373.

85. Berridge, M. J., Bootman, M. D., & Lipp, P. (1998) *Nature* **395**, 645-648.

86. Marchant, J. S. & Parker, I. (2001) *EMBO J.* **20**, 65-76.

87. Callamaras, N. & Parker, I. (1994) *Cell Calcium* **15**, 66-78.

88. Sneyd, J. & Falcke, M. (2005) *Prog. Biophys. Mol. Biol.* **89**, 207-245.

89. Fontanilla, R. A. & Nuccitelli, R. (1998) *Biophys. J.* **75**, 2079-2087.

90. Sneyd, J. & Kalachev, L. V. (1994) *Cell Calcium* **15**, 289-296.

91. Bugrim, A. E., Zhabotinsky, A. M., & Epstein, I. R. (1997) *Biophys. J.* **73**, 2897-2906.

92. Shuai, J. W. & Jung, P. (2003) *Proc. Natl. Acad. Sci. U. S. A* **100**, 506-510.

93. Shuai, J. W. & Jung, P. (2002) *Biophys. J.* **83**, 87-97.

94. Sun, X. P., Callamaras, N., Marchant, J. S., & Parker, I. (1998) *J. Physiol* **509 ( Pt 1)**, 67-80.

95. Shuai, J. W. & Jung, P. (2002) *Phys. Rev. Lett.* **88**, 068102.

96. Li, Y. X. & Rinzel, J. (1994) *J. Theor. Biol.* **166**, 461-473.

97. De Young, G. W. & Keizer, J. (1992) *Proc. Natl. Acad. Sci. U. S. A* **89**, 9895-9899.

98. Nuccitelli, R., Yim, D. L., & Smart, T. (1993) *Dev. Biol.* **158**, 200-212.

99. Venable, R. M., Zhang, Y., Hardy, B. J., & Pastor, R. W. (1993) *Science* **262**, 223-226.

100. Tieleman, D. P. & Berendsen, H. J. (1998) *Biophys. J.* **74**, 2786-2801.

101. Tieleman, D. P., Marrink, S. J., & Berendsen, H. J. (1997) *Biochim. Biophys. Acta* **1331**, 235-270.

102. Allen, M. P. & Tildesley, D. J. (1987) *Computer Simulation of Liquids* (Clarendon Press, Oxford).

103. Tieleman, D. P., Leontiadou, H., Mark, A. E., & Marrink, S. J. (2003) *J. Am. Chem. Soc.* **125**, 6382-6383.

104. Balucani, U., Brodholt, J. P., & Vallauri, R. (1996) *J. Phys. Condens. Matter* **8**, 6139-6144.

105. Yeh, I. C. & Berkowitz, M. L. (1999) *J. Chem. Phys.* **110**, 7935-7942.

106. Mahoney, M. W. & Jorgensen, W. L. (2000) *J. Chem. Phys.* **112**, 8910-8922.

107. Joshi, R. P., Sridhara, V., & Schoenbach, K. H. (2006) *Biochem. Biophys. Res. Commun.* **348**, 643-648.

108. Marrink, S. J., Berger, O., Tieleman, P., & Jahnig, F. (1998) *Biophys. J.* **74**, 931-943.

109. Ott, M., Robertson, J. D., Gogvadze, V., Zhivotovsky, B., & Orrenius, S. (2002) *Proc. Natl. Acad. Sci. U. S. A* **99**, 1259-1263.

110. Nicholls, P. (1974) *Biochim. Biophys. Acta* **346**, 261-310.

111. Chuprina, V. P., Heinemann, U., Nurislamov, A. A., Zielenkiewicz, P., Dickerson, R. E., & Saenger, W. (1991) *Proc. Natl. Acad. Sci. U. S. A* **88**, 593-597.

112. Kopka, M. L., Fratini, A. V., Drew, H. R., & Dickerson, R. E. (1983) *J. Mol. Biol.* **163**, 129-146.

113. Dickerson, R. E., Drew, H. R., Conner, B. N., Wing, R. M., Fratini, A. V., & Kopka, M. L. (1982) *Science* **216**, 475-485.

114. Sorin, E. J. & Pande, V. S. (2005) *Biophys. J.* **88**, 2472-2493.

115. Deng, J., Schoenbach, K. H., Buescher, E. S., Hair, P. S., Fox, P. M., & Beebe, S. J. (2003) *Biophys. J.* **84**, 2709-2714.

116. White, J. A., Blackmore, P. F., Schoenbach, K. H., & Beebe, S. J. (2004) *J. Biol. Chem.* **279**, 22964-22972.

117. Tuszynski, J. A. & Kurzynski, M. (2003) *Introduction to Molecular Biophysics* (CRC Press, Boca Raton;London;New York; Washington DC).

118. Guy, H. R. (2006) National Cancer Institute, National Institute of Health, personal communication.

119. Breed, J., Biggin, P. C., Kerr, I. D., Smart, O. S., & Sansom, M. S. (1997) *Biochim. Biophys. Acta* **1325**, 235-249.

120. Hodgkin, A. L. & Huxley, A. F. (1952) *J. Physiol* **117**, 500-544.

121. Parsegian, A. (1969) *Nature* **221**, 844-846.

122. Durell, S. R., Shrivastava, I. H., & Guy, H. R. (2004) *Biophys. J.* **87**, 2116-2130.

123. Starace, D. M., Stefani, E., & Bezanilla, F. (1997) *Neuron* **19**, 1319-1327.

124. Jiang, Y., Lee, A., Chen, J., Ruta, V., Cadene, M., Chait, B. T., & MacKinnon, R. (2003) *Nature* **423**, 33-41.

125. Jiang, Y., Ruta, V., Chen, J., Lee, A., & MacKinnon, R. (2003) *Nature* **423**, 42-48.

126. Prestegard, J. H. & Fellmeth, B. (1974) *Biochemistry* **13**, 1122-1126.

127. Siegel, D. P. (1986) *Biophys. J.* **49**, 1171-1183.

128. Melikyan, G. B., Brener, S. A., Ok, D. C., & Cohen, F. S. (1997) *J. Cell Biol.* **136**, 995-1005.

129. Agre, P., King, L. S., Yasui, M., Guggino, W. B., Ottersen, O. P., Fujiyoshi, Y., Engel, A., & Nielsen, S. (2002) *J. Physiol* **542**, 3-16.

130. Schwarz, D., Richter, W., Kruger, V., Chernogolov, A., Usanov, S., & Stier, A. (1994) *J. Struct. Biol.* **113**, 207-215.

131. Heiskanen, K. M., Bhat, M. B., Wang, H. W., Ma, J., & Nieminen, A. L. (1999) *J. Biol. Chem.* **274**, 5654-5658.

132. Furlan, S., Penna, G. L., Banci, L., & Mealli, C. (2007) *J. Phys. Chem. B Condens. Matter Mater. Surf. Interfaces. Biophys.* **111**, 1157-1164.

133. Feldman, Y., Ermolina, I., & Hayashi, Y. (2003) *IEEE Trans. Dielec. Elec. Insulation* **10**, 728-753.

134. Schwan, H. P. (1968) *Ann. N. Y. Acad. Sci.* **148**, 191-209.

135. Wakamatsu, H. (1997) *Hewlett-Packard J.* **48**, 37.

136. Maxwell, J. C. (1891), ed. Dover (Clarendon, Oxford).

137. Hanai, T., Koizumi, N., & Irimajiri, A. (1975) *Biophys. Struct. Mech.* **1**, 285-294.

138. Raicu, V., Saibara, T., Enzan, H., & Irimajiri, A. (1998) *Bioelectrochem. Bioenerg.* **47**, 333-342.

139. Garner, A. L., Chen, N., Yang, J., Kolb, J. F., Swanson, R. J., Loftin, K. C., Beebe, S. J., Joshi, R. P., & Schoenbach, K. H. (2004) *IEEE Trans. Plasma. Sci* **32**, 2073-2084.

140. Cole, K. S. (1937) *Trans. Faraday Soc.* **33**, 966-972.

141. Gowrishankar, T. R. & Weaver, J. C. (2003) *Proc. Natl. Acad. Sci. U. S. A* **100**, 3203-3208.

142. Joshi, R. P., Hu, Q., Schoenbach, K. H., & Beebe, S. J. (2004) *Phys. Rev. E. Stat. Nonlin. Soft. Matter Phys.* **69**, 051901.

143. Valic, B., Golzio, M., Pavlin, M., Schatz, A., Faurie, C., Gabriel, B., Teissie, J., Rols, M. P., & Miklavcic, D. (2003) *Eur. Biophys. J.* **32**, 519-528.

144. Valic, B., Pavlin, M., & Miklavcic, D. (2004) *Bioelectrochemistry.* **63**, 311-315.

145. Pucihar, G., Kotnik, T., Valic, B., & Miklavcic, D. (2006) *Ann. Biomed. Eng* **34**, 642-652.

# VITA
## VISWANADHAM SRIDHARA

### EDUCATION

2001-2003 *Old Dominion University* Norfolk, VA.
*M.S in Electrical and Computer Engineering*
1996-2000 *College of Engineering, Osmania University* Hyderabad, India.
B.E in Electrical and Electronics Engineering

### HONORS AND AWARDS

February 2007: *Pending offer of* NIH postdoctoral fellowship.
June 2006: Old Dominion University BCET Scholarship ($2000).
April 2006: Nomination for Outstanding Graduate Research Award.

### JOURNAL PUBLICATIONS

Joshi, R.P., Nguyen, A., Sridhara, V., Nuccitelli, R., and Schoenbach, K.H, "Simulations of Calcium Release Dynamics in Response to a High-Intensity, Ultra-Short Electric Pulse,"(*accepted* in Physical Review E, April 2007.)

Pliquett, U., Joshi, R. P., Sridhara, V., Schoenbach, K.H. "Studies of High Electrical Field effects on Cell Membranes." Bioelectrochemistry Vol. 70, Oct. 2006, pp. 275-282.

Joshi, R. P., Sridhara, V., Schoenbach, K.H "Microscopic Calculations of Local Lipid Membrane Permittivities and Diffusion Coefficients for Application to Electroporation Analyses." Biochemical Biophysical Research Communications Vol. 348, Issue. 2, Sept. 2006, pp. 643-648.

Hu, Q., Sridhara, V., Joshi, R. P., J. Kolb and K.H, Schoenbach, "Molecular Dynamics Analysis of High Electric Pulse effects on Bilayer Membranes Containing DPPC and DPPS." (*invited paper*) IEEE Transactions on Plasma Science, Vol. 34, no. 4, Aug. 2006, pp. 1405-1411.

Hu, Q., Sridhara, V., Joshi, R. P., Schoenbach, K.H., Beebe, S.J., Blackmore, P.F. "Simulations of transient membrane behavior in cells subjected to a high-intensity ultrashort electric pulse." Physical Review E - Statistical, Nonlinear, and Soft Matter Physics, Vol. 71, no. 3, March 2005, pp. 031914(1-7).

Joshi, R. P., Sridhara, V., Jogai, B., Shah, P., Del Rosario, R.D. "Analysis of dislocation scattering on electron mobility in GaN high electron mobility transistors." Journal of Applied Physics, Vol. 93, no. 12, Jun 15, 2003, pp. 10046-10052.

Joshi, R. P., Sridhara, V., Shah, P., Del Rosario, R.D. " Monte Carlo analysis of GaN-based Gunn oscillators for microwave power generation." Journal of Applied Physics, Vol. 93, no. 8, Apr 15, 2003, pp. 4836-4842.